

FREE CONVECTION HEAT TRANSFER
IN A STRATIFIED MEDIUM – CAVITY PROBLEM

A THESIS SUBMITTED TO
THE GRADUATE SCHOOL OF NATURAL AND APPLIED SCIENCES
OF
MIDDLE EAST TECHNICAL UNIVERSITY

BY

YAVUZ SELİM KAYSERİLIOĞLU

IN PARTIAL FULFILLMENT OF THE REQUIREMENTS
FOR
THE DEGREE OF DOCTOR OF PHILOSOPHY

IN

MECHANICAL ENGINEERING

SEPTEMBER 2013

Approval of the thesis:

**FREE CONVECTION HEAT TRANSFER
IN A STRATIFIED MEDIUM – CAVITY PROBLEM**

submitted by **YAVUZ SELİM KAYSERİLİOĞLU** in partial fulfillment of the requirements for the degree of **Doctor of Philosophy in Mechanical Engineering Department, Middle East Technical University** by,

Prof. Dr. Canan Özgen _____
Dean, Graduate School of **Natural and Applied Sciences**

Prof. Dr. Suha Oral _____
Head of Department, **Mechanical Engineering**

Prof. Dr. Rüknettin Oskay _____
Supervisor, **Mechanical Engineering Dept., METU**

Assoc. Prof. Dr. Tuba Okutucu Özyurt _____
Co-Supervisor, **Mechanical Engineering Dept., METU**

Examining Committee Members:

Prof. Dr. Faruk Arınç _____
Mechanical Engineering Dept., METU

Prof. Dr. Rüknettin Oskay _____
Mechanical Engineering Dept., METU

Prof. Dr. Nafiz Alemdaroğlu _____
Aerospace Engineering Dept., METU

Assoc. Prof. Dr. İlker Tarı _____
Mechanical Engineering Dept., METU

Asst. Prof. Dr. Barbaros Çetin _____
Mechanical Engineering Dept., Bilkent University

Date:

27/09/2013

I hereby declare that all information in this document has been obtained and presented in accordance with academic rules and ethical conduct. I also declare that, as required by these rules and conduct, I have fully cited and referenced all material and results that are not original to this work.

Name, Last name : Yavuz Selim Kayseriliođlu

Signature :

ABSTRACT

FREE CONVECTION HEAT TRANSFER IN A STRATIFIED MEDIUM – CAVITY PROBLEM

Kayseriilioğlu, Yavuz Selim

Ph.D., Department of Mechanical Engineering

Supervisor: Prof. Dr. Rüknettin Oskay

Co-Supervisor: Assoc. Prof. Dr. Tuba Okutucu Özyurt

September 2013, 133 Pages

A numerical study is performed in order to simulate a 2D cavity filled with water having one inlet and one outlet. Relatively warm water is fed to the cavity to charge it while relatively cooler water is drained from the outlet. The top surface of the cavity is exposed to ambient air. Bottom surface is insulated while vertical side surfaces are cooled.

Mathematical model comprised of laminar 2D transient flow of an incompressible fluid. Momentum and energy equations are solved simultaneously with Boussinesq approximation since both forced and natural convection occur within cavity.

The charging period of the cavity with relatively hot charging water is examined. Velocity and temperature fields for cavity are presented. Effects of initial temperature, ambient air temperature, inlet charging temperature, and solar radiation on free surface are examined. It is found that lower initial storage temperature, higher ambient air temperature, higher charging water temperature, and existence of solar radiation have positive effects on the performance of cavity.

Heat removal period from cavity is examined. Basic heat removal tubes with rectangular cross-sections are modeled as negative heat generation sources. Heat removal process affects regions below the tubes more than regions above the tubes. The effect of heat removal is seen all the way down to bottom of the cavity whereas only a couple of centimeters above the heat removal tubes are affected. As a result, when heat is removed from a lower layer, stored energy content of cavity at the end of heat removal is higher.

Keywords: Sensible Heat Storage, Thermal Stratification, Warm Water Storage, Finite Volume Method, SIMPLE Algorithm

ÖZ

ISIL TABAKALANMIŞ ORTAMDA DOĞAL ISI TRANSFERİ – BOŞLUK PROBLEMİ

Kayseriliođlu, Yavuz Selim
Doktora, Makine Mühendisliđi Bölümü
Tez Yöneticisi: Prof. Dr. Rüknettin Oskay
Ortak Tez Yöneticisi: Doç. Dr. Tuba Okutucu Özyurt
Eylül 2013, 133 Sayfa

İki boyutlu, bir girişı bir de çıkışı olan, içi su dolu bir boşluđu simüle etmek için sayısal çalışma yapılmıştır. Görece sıcak su boşluđu yüklemek için girişten verilirken görece sođuk su çıkıştan çekilir. Boşluđun üst yüzü ortam havası ile temas halindedir. Alt yüzey ısı yalıtılmışken dikey yan yüzeyler sođutulmaktadır.

Matematik model sıkıştırılmaz bir akışkanın laminar, geçici, iki boyutlu akışından oluşmaktadır. Boşlukta hem zorlama hem doğal taşınım olduđu için momentum ve enerji denklemleri Boussinesq yaklaşımını yardımıyla eşzamanlı çözölmektedir.

Boşluđun sıcak suyla yüklendiđi yükleme süreci incelenmektedir. Boşluđun hız ve sıcaklık alanı sunulmaktadır. İlk sıcaklığın, ortam hava sıcaklığının, yükleme suyu sıcaklığının ve su yüzeyine güneş ışınımının etkileri incelenmektedir. Daha sođuk ilk sıcaklığın, daha sıcak ortam hava sıcaklığının, daha sıcak yükleme sıcaklığının ve güneş ışınımının bulunmasının boşluk performansına olumlu etkisi olduđu görölmektedir.

Boşlukta ısı çekme süreci incelenmektedir. Basit dikdörtgen kesitli ısı çekme tüpleri negatif ısı jenerasyonu kaynađı olarak modellenmektedir. Isı çekmenin tüplerin altında kalan kısımları tüplerin üzerinde kalan kısımlardan daha çok etkilediđi gözlemlenmiştir. Isı çekmenin etkisinin tabana kadar etkili olduđu, ancak tüplerin üzerinde sadece birkaç santimetrelik bir bölgeyi etkilediđi görölmektedir. Sonuç olarak boşluđun daha aşağılarından ısı çekildiđinde, ısı çekme sonuçlandıđında boşlukta kalan ısı enerjisi daha fazladır.

Anahtar Kelimeler: Duyulur Isı Depolama, Isıl Tabakalanma, Sıcak Su Deposu, Sonlu Hacimler Yöntemi, SIMPLE Algoritması

To my dearest nephew Emir and to my pretty niece Ece

ACKNOWLEDGMENTS

I am deeply grateful to my supervisor, Prof. Dr. Rüknettin Oskay, for his guidance, inspiration, and invaluable help all throughout the study.

I would like to present my thanks to the members of the thesis supervising committee, Prof. Dr. Nafiz Alemdaroğlu and Prof. Dr. Faruk Arınç, for their insightful advice.

I wish to express my sincere appreciation to Asst. Prof. Dr. Barbaros Çetin, our lack of success in the modeling of the problem with a commercial software package increased my confidence on the coding of my own program.

Finally, I express my deepest gratitude to my family, for their continuous encouragement, understanding, and support.

TABLE OF CONTENTS

ABSTRACT.....	v
ÖZ.....	vi
ACKNOWLEDGMENTS.....	viii
TABLE OF CONTENTS.....	ix
LIST OF TABLES.....	xi
LIST OF FIGURES.....	xii
NOMENCLATURE.....	xvi
CHAPTERS	
1. INTRODUCTION.....	1
2. LITERATURE REVIEW.....	5
3. MATHEMATICAL FORMULATION.....	13
4. FINITE VOLUME METHOD.....	21
4.1 Discretization of the Governing Equations.....	21
4.2 Staggered Grid.....	29
4.3 The Discretized Forms of the Governing Equations in Staggered Grid.....	31
4.4 The SIMPLE Algorithm.....	31
4.5 Boundary Conditions.....	36
4.6 Solution of Discretized Equations.....	42
4.7 Monitoring Convergence.....	43
4.8 Under-relaxation.....	44
4.8 Linearization of the Source Term and Always Positive Coefficients Rule.....	45
5. THE COMPUTER CODE.....	49
6. VALIDATION OF THE CODE.....	53
6.1 2D Laminar Steady Flow within a Lid-Driven Cavity.....	53
6.2 2D Laminar Steady Flow with Energy Equation within a Cavity with 1 Inlet and 1 Outlet.....	54
7. RESULTS AND DISCUSSIONS.....	61
7.1 The Geometry, Initial Condition, and Boundary Conditions.....	61
7.2 Examination of the Thermal Boundary Condition on the Vertical Side Walls.....	63
7.3 Conservation of Energy Equation for the Cavity in Time-Rate Form.....	80
7.4 The Flow Field.....	83
7.5 Dimensionless Bulk Temperature, θ	91
7.6 Effect of Initial Temperature.....	92
7.7 Effect of Ambient Temperature.....	96
7.8 Effect of Inlet Temperature.....	98

7.9 Effect of Solar Radiation.....	100
7.10 Lower Aspect Ratio.....	103
7.11 Heat Removal Period.....	105
8. CONCLUSIONS.....	111
REFERENCES.....	115
APPENDICES	
A. DISCRETIZATION OF THE GENERAL TRANSPORT EQUATION WITH THE HYBRID DIFFERENCING SCHEME.....	119
B. ILLUSTRATIVE MATERIAL.....	121
CURRICULUM VITAE.....	133

LIST OF TABLES

TABLES

Table 4.1	Transport Variables, Diffusion Coefficients, and Source Functions for Governing Equations.....	21
Table 4.2	Staggered Grid Point Locations for the Velocity Cells and the Scalar Cell.....	31
Table B.1	Geometry and Flow Parameters of the Simulations.....	131
Table B.2	Wall Heat Flux Variation with Time in a Typical Experiment	132

LIST OF FIGURES

FIGURES

Fig. 2.1	Development of Vertical Temperature Profile within the Storage Unit During Charging, from [17].....	9
Fig. 2.2	Development of Vertical Temperature Profile within the Storage Unit During Heat Removal with Charging Continued, from [17].....	10
Fig. 2.3	Development of Vertical Temperature Profile within the Storage Unit During Heat Removal without Charging Continued, from [17].....	11
Fig. 3.1	Schematic of the Cavity.....	13
Fig. 3.2	Cross Section of the Cavity at a Constant z -plane.....	14
Fig. 4.1	An Arbitrary Portion of the 3D Grid.....	22
Fig. 4.2	An Arbitrary Portion of the 2D Grid.....	23
Fig. 4.3	2D Backward Staggered Grid.....	30
Fig. 4.4	The SIMPLE Algorithm (Adapted from [21]).....	35
Fig. 4.5	Inlet Boundary Discretization.....	36
Fig. 4.6	Exit Boundary Discretization.....	37
Fig. 4.7	Wall Boundary Discretization.....	39
Fig. 4.8	Free-Surface Boundary Discretization.....	41
Fig. 4.9	A Typical Near Boundary Temperature Cell.....	46
Fig. 5.1	Flow Chart of the Program.....	52
Fig. 6.1	Comparison of Streamlines for Lid-Driven Cavity, $Re = 100$, On the Left, Output of the Code, On the Right, from [29].....	54
Fig. 6.2	Schematic Configuration of the Cavity, from [30].....	54
Fig. 6.3	Variation of Streamlines and Isotherm Contours for Different Ri values, from [30].....	57
Fig. 6.4	Streamlines and Isotherms for $Ri = 0$ ($Re = 100, Pr = 0.71$).....	58
Fig. 6.5	Streamlines and Isotherms for $Ri = 1$ ($Re = 100, Pr = 0.71$).....	58
Fig. 6.6	Streamlines and Isotherms for $Ri = 5$ ($Re = 100, Pr = 0.71$).....	58

Fig. 6.7	Streamlines and Isotherms for $Ri = 10$ ($Re = 100$, $Pr = 0.71$).....	59
Fig. 7.1	2D Cavity Geometry.....	61
Fig. 7.2	Schematic Drawing of Experimental Set-up Showing the Water Jackets, Front and Side Views.....	63
Fig. 7.3	Development of Vertical Temperature Profile within Cavity at $x = 1$ m for Simulation 1.....	65
Fig. 7.4	Development of Vertical Temperature Profile within Cavity, from [17]	66
Fig. 7.5	Development of Vertical Temperature Profile within Cavity at $x = 1$ m for Simulation 2.....	68
Fig. 7.6	Development of Vertical Temperature Profile within Cavity at $x = 1$ m for Simulation 4.....	70
Fig. 7.7	Development of Vertical Temperature Profile within Cavity at $x = 1$ m for Simulation 6.....	71
Fig. 7.8	Development of Vertical Temperature Profile within Cavity at $x = 1$ m for Simulation 8.....	73
Fig. 7.9	Different Spatial & Temporal Heat Flux Patterns for Vertical Side Walls.....	74
Fig. 7.10	Development of Vertical Temperature Profile within Cavity at $x = 1$ m for Simulation 10.....	76
Fig. 7.11	Development of Vertical Temperature Profile within Cavity at $x = 1$ m for Simulation 12.....	77
Fig. 7.12	Development of Vertical Temperature Profile within Cavity at $x = 1$ m for Simulation 13.....	78
Fig. 7.13	Development of Vertical Temperature Profile within Cavity at $x = 1$ m for Simulation 14.....	79
Fig. 7.14	Variation of Components of Energy Equation in Time-Rate Form for Simulation 14.....	82
Fig. 7.15	Velocity Vectors within the Cavity during Charging, for Simulation 14.....	84
Fig. 7.16	Streamlines within the Cavity during Charging for Simulation 14....	87
Fig. 7.17	Temperature Distribution within the Cavity and the Inlet and the Outlet during Charging for Simulation 14.....	89
Fig. 7.18	Variation of Dimensionless Bulk Temperature Distribution within the Cavity during Charging for Simulation 14.....	92

Fig. 7.19	Development of Vertical Temperature Profile within Cavity at $x = 1$ m for Simulation 15, $T_{ic} = 16^{\circ}\text{C}$, $T_{amb} = 16^{\circ}\text{C}$	93
Fig. 7.20	Development of Vertical Temperature Profile within Cavity at $x = 1$ m for Simulation 16, $T_{ic} = 20^{\circ}\text{C}$, $T_{amb} = 16^{\circ}\text{C}$	94
Fig. 7.21	Development of Vertical Temperature Profile within Cavity at $x = 1$ m for Simulation 17, $T_{ic} = 24^{\circ}\text{C}$, $T_{amb} = 16^{\circ}\text{C}$	95
Fig. 7.22	Variation of Dimensionless Bulk Temperature Distribution within the Cavity during Charging for Simulations 15, 16, and 17.....	96
Fig. 7.23	Development of Vertical Temperature Profile within Cavity at $x = 1$ m for Simulation 19, $T_{ic} = 20^{\circ}\text{C}$, $T_{amb} = 10^{\circ}\text{C}$	97
Fig. 7.24	Variation of Dimensionless Bulk Temperature Distribution within the Cavity during Charging for Simulations 14, 16, and 19.....	98
Fig. 7.25	Development of Vertical Temperature Profile within Cavity at $x = 1$ m for Simulation 20, $T_{in} = 40^{\circ}\text{C}$	99
Fig. 7.26	Variation of Dimensionless Bulk Temperature within the Cavity during Charging for Simulations 14 and 20.....	100
Fig. 7.27	Development of Vertical Temperature Profile within Cavity at $x = 1$ m for Simulation 21, $q''_{solar} = 200\text{ W/m}^2$	101
Fig. 7.28	Development of Vertical Temperature Profile within Cavity at $x = 1$ m for Simulation 22, $q''_{solar} = 400\text{ W/m}^2$	102
Fig. 7.29	Variation of Dimensionless Bulk Temperature within the Cavity during Charging for Simulations 14, 21 and 22.....	103
Fig. 7.30	Development of Vertical Temperature Profile within Cavity at $x = 1$ m for Simulation 23, $A = 0.15$	104
Fig. 7.31	Schematic Drawing of 2D Cavity Showing the Heat Removal Tubes.....	105
Fig. 7.32	Development of Vertical Temperature Profile within Cavity at $x = 1$ m for Simulation 14.1, $h_{rem} = 0.18\text{ m}$	106
Fig. 7.33	Development of Vertical Temperature Profile within Cavity at $x = 1$ m for Simulation 14.3, $h_{rem} = 0.06\text{ m}$	107
Fig. 7.34	Development of Vertical Temperature Profile within Cavity at $x = 1$ m for Simulation 14.5, $h_{rem1} = 0.18\text{ m}$, $h_{rem2} = 0.06\text{ m}$	108

Fig. 7.35	Variation of Components of Energy Equation in Time-Rate Form for Simulation 14.1.....	109
Fig. 7.36	Variation of Dimensionless Bulk Temperature within the Cavity during Charging for Simulations 14.1 thru 14.7.....	110
Fig. B.1	Development of Vertical Temperature Profile within Cavity at $x = 1\text{m}$ for Simulation 3.....	122
Fig. B.2	Variation of Components of Energy Equation in Time-Rate Form up to 1200 minutes for Simulation 14.....	123
Fig. B.3	Development of Vertical Temperature Profile within Cavity at $x = 0\text{m}$ for Simulation 14.....	124
Fig. B.4	Development of Vertical Temperature Profile within Cavity at $x = 0.25\text{m}$ for Simulation 14.....	125
Fig. B.5	Development of Vertical Temperature Profile within Cavity at $x = 1.75\text{m}$ for Simulation 14.....	126
Fig. B.6	Development of Vertical Temperature Profile within Cavity at $x = 2\text{m}$ for Simulation 14.....	127
Fig. B.7	Comparison of Experimental Data (Experiment 1 from [17]) with Simulation Data, $A = H/L = 0.26$, $\dot{m}_{in} = 206\text{kg/hr}$, $T_{in} = 47.5^\circ\text{C}$, $T_{ic} = 25.2^\circ\text{C}$, $T_{amb} = 24^\circ\text{C}$, $q''_{wt} = 5000\text{W/m}^2$ as of Fig. 7.9.b.....	128
Fig. B.8	Comparison of Experimental Data (Experiment 1 from [17]) with Simulation Data, $A = H/L = 0.26$, $\dot{m}_{in} = 206\text{kg/hr}$, $T_{in} = 47.5^\circ\text{C}$, $T_{ic} = 25.2^\circ\text{C}$, $T_{amb} = 24^\circ\text{C}$, $q''_{wt} = 5000\text{W/m}^2$ as of Fig. 7.9.c.....	129
Fig. B.9	Comparison of Experimental Data (Experiment 1 from [17]) with Simulation Data, $A = H/L = 0.26$, $\dot{m}_{in} = 206\text{kg/hr}$, $T_{in} = 47.5^\circ\text{C}$, $T_{ic} = 25.2^\circ\text{C}$, $T_{amb} = 24^\circ\text{C}$, $q''_{wt} = 5000\text{W/m}^2$ as of Fig. 7.9.d.....	130

NOMENCLATURE

A	area, m^2
A	aspect ratio, H/L
B	width of storage medium, m
c_p	constant pressure specific heat, J/kgK
c_v	constant volume specific heat, J/kgK
D	diffusion conductance, kg/s
D_{av}	binary diffusion coefficient, m^2/s
d	relative location of heat removal tubes from free surface, m
E	energy, J
e	specific energy, J/kg
F	strength of convection, kg/s
H	height of storage medium, m
H	enthalpy, J
\dot{H}	enthalpy flow rate, W
h	specific enthalpy, J/kg
h	convective heat transfer coefficient, W/m^2K
h_{fg}	latent heat of vaporization, J/kg
k	thermal conductivity, W/mK
L	length of storage medium, m
Le	Lewis number, α/D_{ab}
m	mass, kg
\dot{m}	mass flow rate, kg/s
Nu	Nusselt number, hL/k
P	pressure, Pa
Pe	Peclet number, uL/α

Pr	Prandtl number, ν/α
Q	heat transfer, J
\dot{Q}	rate of heat transfer, W
R	residual
Ra	Rayleigh number, $g\beta(T_s - T_\infty)L_{ch}^3/\nu\alpha$
Re	Reynolds number, uL/ν
Ri	Richardson number, $g\beta(T - T_{ic})L/u^2$
S	source function
T	temperature, °C
t	time, s
U	internal energy, J
u	specific internal energy, J/kg
V	velocity, m/s
V	volume, m ³
\mathbf{v}	velocity vector, m/s
W	work, J
w	specific humidity ratio, kg _w /kg _a
x	Cartesian coordinate along length
y	Cartesian coordinate along width
z	Cartesian coordinate along depth

Greek Symbols

α	under-relaxation factor
α	thermal diffusivity, m ² /s
β	thermal expansion coefficient, 1/K
ϕ	generic transport variable
ϕ	relative humidity, %
Γ	generic diffusion coefficient
ν	kinematic viscosity, m ² /s

ρ	density, kg/m ³
θ	dimensionless bulk temperature, $(T_b - T_{ic}) / (T_{in} - T_{ic})$

Subscripts

<i>a</i>	air
<i>amb</i>	ambient
<i>b</i>	bulk
<i>b, B</i>	bottom
<i>ch</i>	characteristic
<i>conv</i>	convective
<i>e</i>	exit
<i>e, E</i>	east
<i>evap</i>	evaporative
<i>f</i>	film
<i>ic</i>	initial condition
<i>in</i>	inlet
<i>L</i>	limiting value
<i>m</i>	mass transfer
<i>n, N</i>	north
<i>out</i>	outlet
<i>rem</i>	removed
<i>s</i>	surface
<i>s, S</i>	south
<i>t, T</i>	top
<i>w</i>	water
<i>w, W</i>	west
<i>wl</i>	wall
<i>ws</i>	water at saturation
∞	free stream

Abbreviations

B.C.	boundary condition
C.S.	control surface
C.V.	control volume
CFD	Computational Fluid Dynamics
CHT	Computational Heat Transfer
FVM	Finite Volume Method
I.C.	initial condition
TDMA	Tri-Diagonal Matrix Algorithm
SIMPLE	Semi-Implicit Method for Pressure-Linked Equations

CHAPTER 1

INTRODUCTION

Energy storage systems involve the collection and retention of readily available energy for later use. There are four main modes of energy storage; electrical, mechanical, chemical, and thermal. Among these, thermal energy storage is attractive for the applications related to waste heat recovery, solar energy utilization, and peak electricity.

Thermal energy can be stored as sensible heat, as latent heat of phase change, or in a reversible chemical reaction. Latent heat can be stored within a medium undergoing a phase change. For example, during boiling of a liquid, heat of vaporization is stored in its vapor and this stored energy can be released during the condensation of the vapor. Thermal energy can be stored in a reversible chemical reaction. During an endothermic reaction, energy is stored and when the reaction is reversed, the exothermic reaction releases the stored energy.

Sensible heat storage systems utilize materials that store energy as sensible heat, thus the temperature of storage medium changes as it stores or discharges thermal energy. The sensible heat gained or lost by a material during a change in temperature from T_1 to T_2 can be written as;

$$Q = V \int_{T_1}^{T_2} \rho c dT \quad (1.1)$$

Where Q : Sensible heat gained or lost

T : Temperature of the material

ρ : Density of the material

V : Volume of the material

c : Specific heat capacity of the material

Liquids and solids are used as the storage media. Most commonly used solids as the solid storage media are rocks and pebble beds. Water is the most common liquid used as liquid storage media.

Some of the advantages of using water as the sensible heat storage medium are:

- it is cheap and abundant,
- has relatively high heat capacity (five times more than that of granite),
- has lower density compared to rocks,
- non-toxic, non-combustible.

General operational problems of sensible heat storage systems can be summarized as [1]:

- Temperature of the storage medium continually rises during charging which results in greater heat loss.
- Temperature of the storage medium continually drops during heat removal which results in smaller heat flux deliveries.
- Heat storage occurs at temperatures higher than ambient temperature. Therefore insulation is required which increases system cost.

The temperature distribution within the sensible liquid storage medium can be isothermal as it is in a well-mixed liquid storage or can be non-uniform as it is in thermally stratified storage.

Thermal stratification is a kind of non-uniform temperature distribution in a body. It occurs especially in the vertical direction within a water storage tank. The relatively warmer water entering the storage unit is lighter than the relatively colder water inside the storage tank and remains on top of the relatively cold water of the storage, resulting in non-uniform temperature distribution in the vertical direction. The benefit of thermal stratification in a water storage is that liquid at a higher temperature than the overall mixed temperature can be stored at the top of the storage medium.

The main objective of the present study is to simulate numerically a rectangular parallelepiped cavity. The cavity is a flow through reservoir containing water in it as the working fluid, and charged from a single inlet by relatively warm water and discharged by a single outlet from the opposite side of the inlet. The two side walls along the inlet and the outlet are cooled to attain thermal stratification whereas the remaining two side walls are kept at a constant wall temperature, while the bottom surface is assumed to be insulated. The top surface is a free surface permitting interaction of the fluid filling the cavity with the ambient air.

The three dimensional Navier-Stokes equations and the energy equation will be solved for unsteady conditions for an incompressible fluid with constant viscosity and thermal conductivity. The method used in the discretization of the governing equations is the Finite Volume Method. SIMPLE algorithm will be the solution algorithm.

There will be two stages of the simulations. In the first stage, the cavity (the relative dimensions of the cavity will be changed) will be charged (with different charging

temperatures, starting from different initial temperatures, with/without solar radiation on the free-surface) until a steady-state flow field and temperature field is established within the cavity. This state corresponds to the equilibrium state at which thermal energy input to the cavity equals heat losses from the cavity. At this time, the highest amount of thermal energy is stored within the cavity.

Next, the heat extraction stage begins; thermal energy in the cavity will be used with the help of heat-exchangers. Equal amount of heat will be extracted from different depths of the cavity in order to observe the resulting effect of heat removal on the flow and temperature fields. The flow field and the temperature field within the cavity will converge to yet another steady-state.

CHAPTER 2

LITERATURE REVIEW

Some of the aspects that are important in the evaluation of storage performance of a sensible storage may be classified as follows; the velocity and temperature of the inlet flow charging the storage medium, relative locations of the inlet and outlet channels or ports with respect to the storage geometry, boundary conditions of the storage medium, especially at the surface if there is a free surface with the ambient, aspect ratio dictated by the storage medium (L/D for cylindrical geometries, L/H for rectangular geometries) and the thermal stratification inside the storage medium. Following is a review of some of the papers available in the literature dealing with these aspects.

Oberkampf and Crow [2] simulated the velocity and temperature fields in a reservoir by using a finite difference procedure. They assumed the flow inside the reservoir to be two-dimensional in a vertical plane and solved the vorticity transport, stream function and energy equations. The inflow was set at a temperature and velocity to simulate thermal discharge from a power plant and occurred at the surface at one end of the reservoir and outflow occurred on the opposite end at different depths. Wind shear, thermal radiation, evaporation, and convection at the surface of the reservoir were considered. They discussed the effects of inflow-outflow, wind shear and heat transfer on the reservoir.

Lavan and Thompson [3] studied thermal stratification in hot water storage systems. Cylindrical plastic vessels with various length-to-diameter ratios were charged with varying inlet-outlet temperature differences and mass flow rates. They also studied inlet and exit port configuration on thermal stratification. They concluded that, even at very large flow rates, thermal stratification could be maintained in cylindrical water tanks. Increasing L/D and inlet and outlet port diameter, decreasing mass flow rate improved thermal stratification. They obtained best results when the inlet and outlet ports were near the end walls of the storage tank.

Çömez [4] designed and constructed a sensible heat storage unit as part of his M.S. study. Author observed the development of temperature and velocity profiles experimentally within the storage unit. The main parameters investigated for the evaluation of performance of the storage unit were the charging flow rate, charging temperature and aspect ratio ($A = H/L$) of the water body. Two dimensionless parameters were defined,

the effectiveness, ε , was related to the percentage of input energy which could be stored inside the storage unit and a dimensionless temperature θ , represented a mean bulk temperature for the storage medium. The main conclusions that the author derived were as follows. The storage medium could be thermally stratified for all of the charging mass flow rates. Better stratification was observed at lower charging rates. Aspect ratio was an important parameter affecting the performance of the storage unit. Lower aspect ratios gave better storage performance. Slow moving convective currents were observed during the flow visualization tests.

Jaluria and Gupta [5] carried out an experimental study of the temperature decay in a thermally stratified water body. Water body was initially stratified by the recirculating flow of hot water discharge and by the addition of hot water at the top of the colder fluid. After the fluid was stratified, it was allowed to cool without any external charging of the storage. They also investigated the cooling of an isothermal water region. Greater buoyancy-induced mixing was observed in isothermal case, since stratified region inhibited mixing currents and energy transfer in this region was mainly by thermal diffusion. They concluded that stratified medium was a better energy storage system compared to the isothermal one. Experimental results indicated that the temperature field was largely one-dimensional and they formulated a simple analytical model. Analytical results were in good agreement with the experimental results.

Jaluria and O'Mara [6] studied experimentally the recirculating flow in an enclosed water region due to the discharge of heated, buoyant, surface jets, coupled with withdrawal of cold fluid at the other end of the region. They determined both the transient and steady-state temperature fields. Effects of inflow conditions, flow configuration, enclosure dimensions and the outlet location on the temperature field were examined. They investigated the downward penetration of the flow and thermal stratification in the region. They found that the temperature field in the water body undergoes a rapid transient behavior at the beginning of the flow, followed by a gradual variation to steady-state conditions. Inlet conditions and outlet location determined the transient behavior. An interesting finding was that the temperature field they obtained was mainly two-dimensional, only a small variation was observed in the transverse direction. Buoyancy affected mainly the temperature distribution inside the water body. It was the cause of fairly good horizontal temperature homogeneity except the proximity of inlet and outlet channels.

Yoo and Pak [7] studied a theoretical model of the charging process to provide an upper limit of the performance for stratified thermal storage tanks. They reached a closed-form solution for the transient temperature as a function of Peclet number Pe , assuming perfect piston flow together with appropriate boundary conditions and applying Laplace transform. They compared the model with those from heat conduction between two semi-infinite regions in contact with the moving interface. They concluded that the model could be used for a wider range of Pe , and predicted the thermal behavior of storage tank better compared to the semi-infinite case.

Safi and Loc [8] performed a numerical study for the determination of thermal stratification in an open cavity with one heated discharge. Hot laminar jet entered horizontally into the square cavity at the top of one end, the outlet was at the bottom of the opposite end. They used a finite difference scheme to solve two-dimensional flow described by the Navier-Stokes and energy equations. The influences of non-dimensional parameters of Reynolds, Peclet and Richardson numbers on the flow and thermal stratification were observed. Authors concluded that the flow was strongly dependent on Richardson and Peclet numbers.

Eames and Norton [9] performed a theoretical and experimental study to investigate the thermal performance of stratified hot water stores. They compared their transient three-dimensional finite volume model with the experiments they performed. Variations in inlet velocities, temperatures and initial store stratification were the main concerns. Authors reported that store charging was more efficient when H/D of the store increased and inlet port located near to the top of the store.

Hahne and Chen [10] investigated numerically the flow and heat transfer characteristics of a cylindrical store during charging under adiabatic conditions. The study is concentrated on the effects of charging temperature differences, charging velocities, charging flow rates and length to diameter ratios on the charging efficiency. The conclusions were; charging efficiency depended mainly on Richardson number, Peclet number and aspect ratio of the storage. An increase in Richardson number or aspect ratio revealed an increase in charging efficiency. An increase in Peclet number while keeping Richardson number constant increased charging efficiency.

According to Bouhdjar and Harhad [11], thermal stratification generated in the sensible heat storage should be promoted in order to improve thermodynamic system efficiency of the storage. They presented a numerical study of transient mixed convection. The use of different fluids (Torada oil, ethylene glycol, and water) as a heat storage medium in cylindrical cavities with different aspect ratios (3 to 1/3) was examined. The effect of different fluids was observed by changing the physical properties represented by the Prandtl number. Fluid was injected from the top and discharged from the bottom. They solved conservation equations for laminar natural convection flow with Boussinesq approximation and superimposed forced convection using finite volume method. They presented the performances of the thermal energy storage through the transient thermal storage efficiency.

Ersoy [12] performed a numerical study of mixed convection in cavities. The flow was two-dimensional, incompressible, steady flow of a Newtonian fluid. Gauss-Seidel iteration was used to solve the non-dimensional vorticity transport, stream function, and energy equations for cavities without any inlets or outlets and with single inlet and outlet configurations. Author emphasizes that "Rayleigh number has considerable influence on every variable of the flow." Also for the numerical computations, the author reports that convergence is affected by Rayleigh and Prandtl numbers.

Saha et. al. [13] performed a numerical study on a 2D cavity with one inlet and two exits. Ambient air is fed to the cavity from the inlet located at the bottom of one vertical side wall and the exits are located at the top of the two side walls. The bottom wall of the cavity is heated with constant heat flux while the other three walls of the cavity are adiabatic. Laminar flow of air within the cavity is solved by a control volume based finite element technique. At low Reynolds and Richardson numbers, they observed a large eddy within the cavity. The governing parameter affecting heat transfer is found to be Richardson number.

Das et. al. [14] investigated a rectangular cavity heated symmetrically from the vertical side walls both numerically and experimentally. The numerical model is 2D FVM, while the experimental set-up has two heated opposite side-walls and the remaining side walls are glass. The bottom of cavity is insulated while the top surface is left open. They find a well-mixed zone near the top of the cavity whereas the lower region of the cavity is thermally stratified.

Rahman et. al. [15] studied combined forced and free convection within a rectangular cavity which has an inlet in the middle of the left wall and an outlet at the top of the right wall. The remaining right side wall is heated with constant heat flux and a horizontal conducting cylinder is placed at different locations within the cavity. The numerical method used is Galerkin Finite Element Method. They report that as the diameter of the conductive cylinder increases, the average Nusselt number of the heated wall increases and the average fluid temperature within the cavity decreases.

Papanicolaou and Belessiotis [16] studied numerically a real-scale underground hot-water storage tank. The simulated storage tank has a volume of 8m^3 , concrete bottom and side walls, a free-surface at the top which is covered by an other concrete lid 8 cm above the free-surface. The storage has an inlet at the top of one of the side walls and an exit at the bottom of the same vertical side wall. The storage is charged with constant mass flow rate of water with either at constant temperature, or at transient temperature due to solar-collector heating, or at transient temperature due to electrical heating. The numerical model used is either 2D low Re $k-\varepsilon$ or two-layer turbulence model. When constant temperature charging is used, the inlet velocity is 0.022m/s , the inlet temperature is 50°C , and the initial temperature of the storage is 20°C . Zero-shear velocity B.C. is used at the free-surface. The fluid region and the thick concrete walls are solved together. The streamlines and isotherms at different times are presented. The isotherms reveal thermal stratification in the vertical direction.

In his M. Sc. study, Kayserilioğlu [17] performed an experimental study on the same set-up of [4] with some major alterations. The charging of the storage unit until reaching a steady-state flow field and temperature field was followed by thermal energy extraction from the storage unit by passing cooler water inside coils suspended into the storage unit. During this energy extraction, charging is either continued or ceased. Fig. 2.1 shows the vertical thermal stratification during the charging period of the storage unit, Fig. 2.2,

during the heat removal period of the storage unit whilst the charging is continued, and Fig. 2.3, during the heat removal period of the storage unit whilst the charging is ceased. A steady thermal stratification is achieved (Fig. 2.1) when the total energy input is equaled by heat losses from the storage unit. When the heat removal is started with the continuation of energy charging, temperature field converges another steady profile, not far from the first steady profile (mainly due to lack of complex heat removal equipment and/or not utilizing higher mass flow rates within the heat removal coils).

On the contrary, when the heat removal was in the absence of further charging of the storage unit, decay of thermal stratification was abrupt.

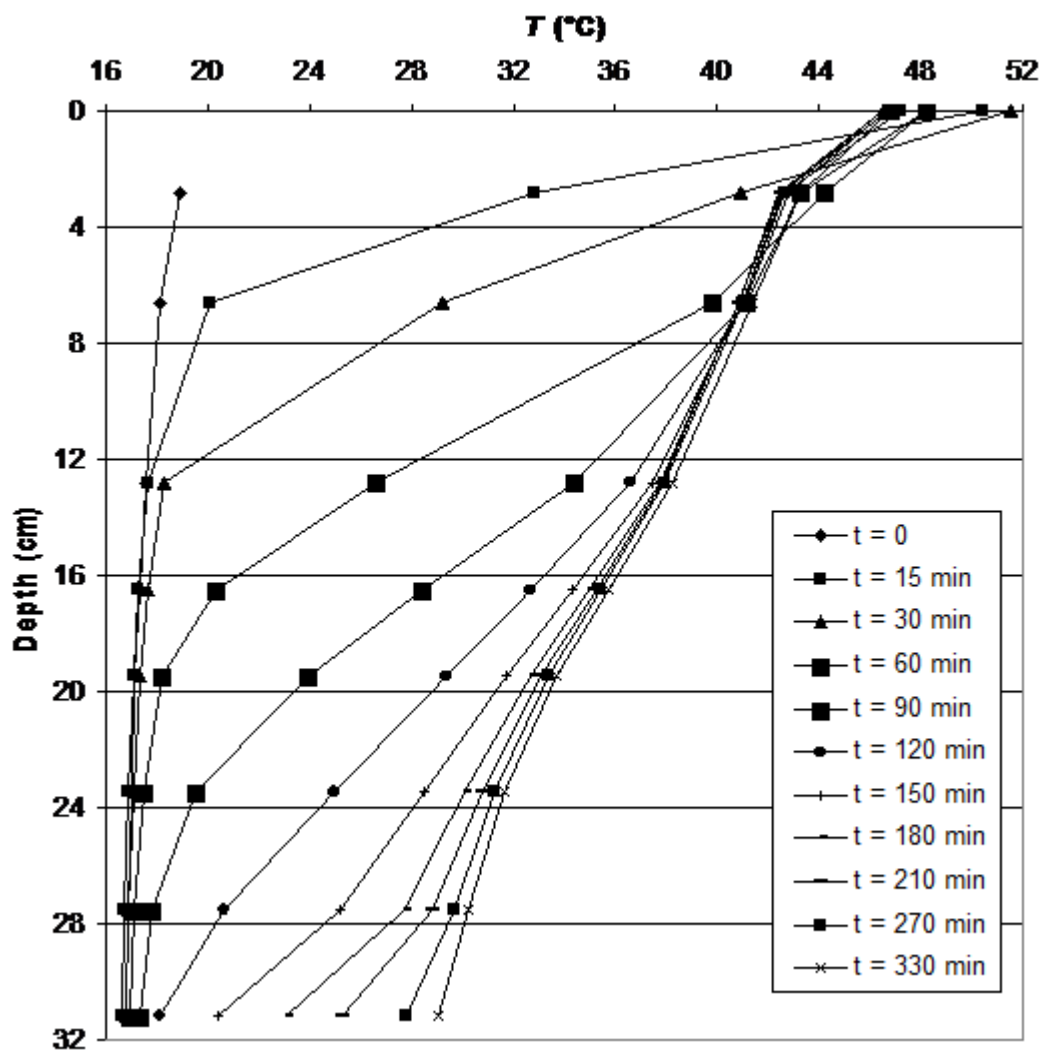


Fig. 2.1 Development of Vertical Temperature Profile within the Storage Unit During Charging, from [17]

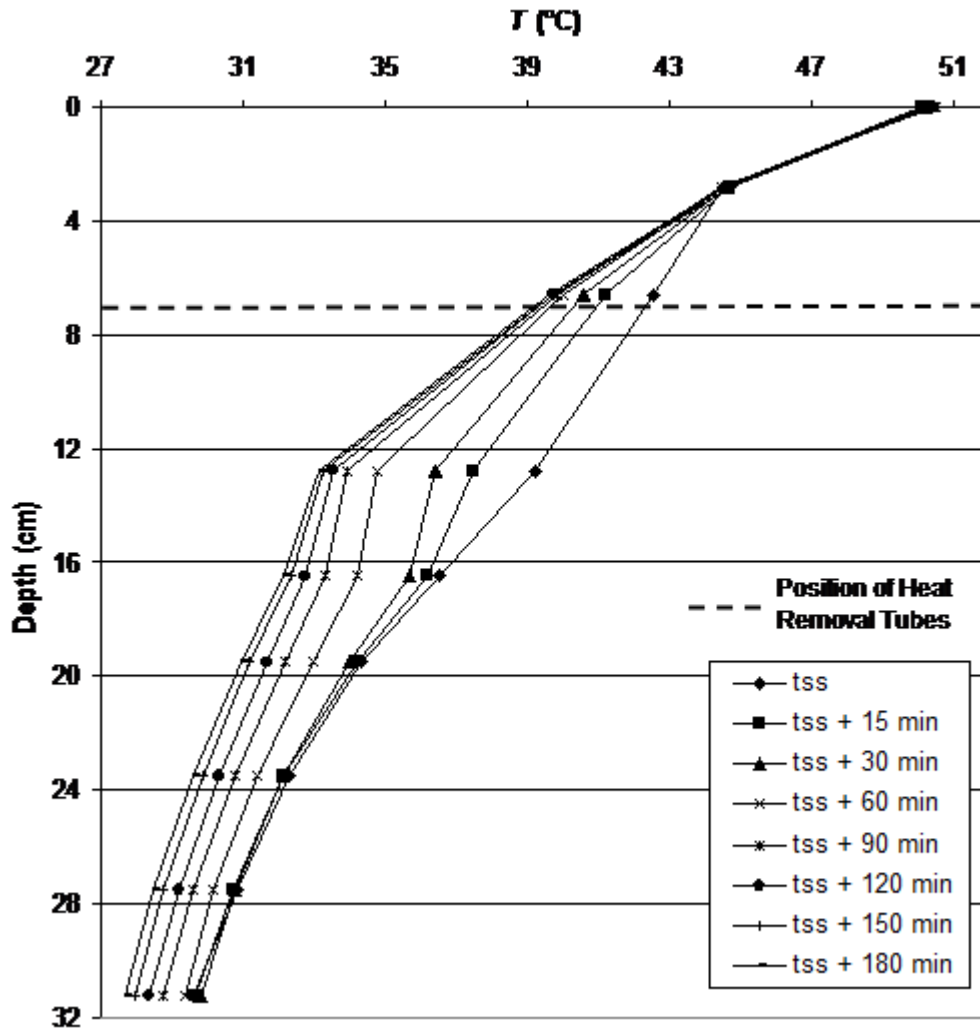


Fig. 2.2 Development of Vertical Temperature Profile within the Storage Unit During Heat Removal with Charging Continued, from [17]

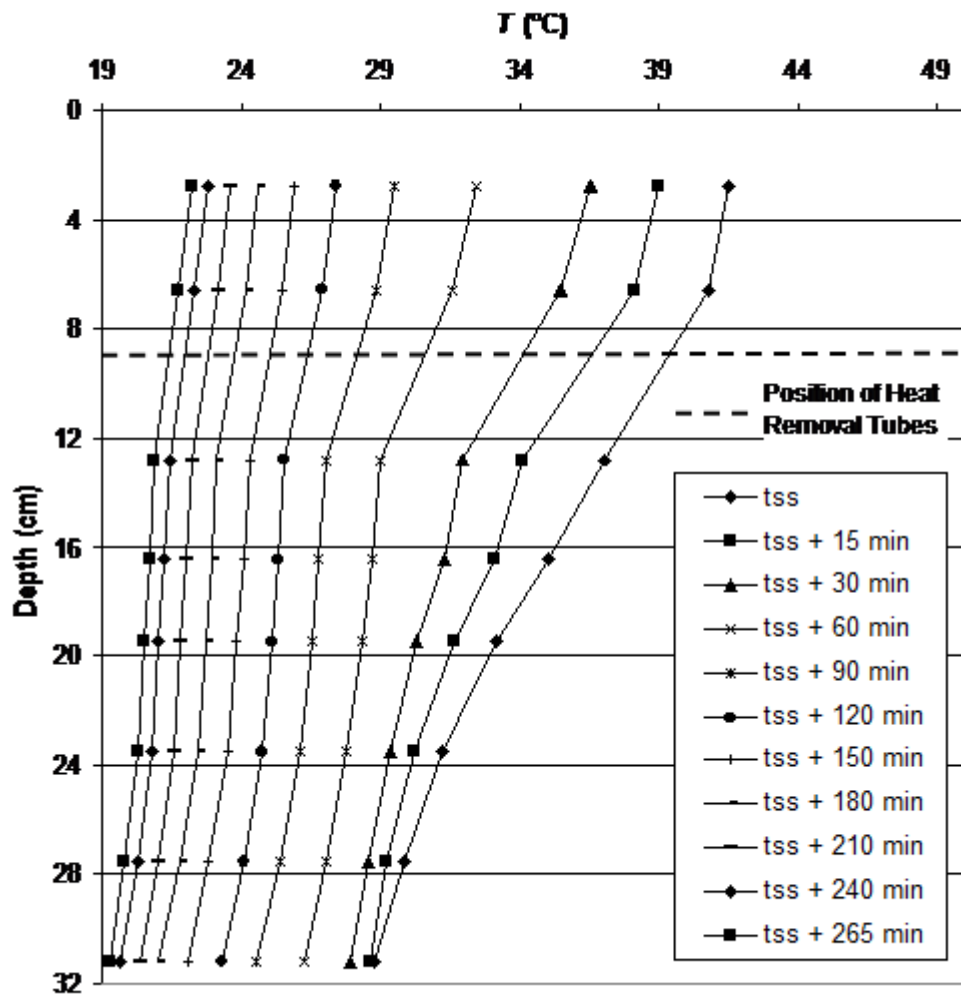


Fig. 2.3 Development of Vertical Temperature Profile within the Storage Unit During Heat Removal without Charging Continued, from [17]

CHAPTER 3

MATHEMATICAL FORMULATION

The schematic of the cavity is presented in Fig. 3.1. A cross section of the cavity at $z=0$ plane is presented in Fig. 3.2. The cavity dimensions are $L \times H \times 2B$. Side walls are cooled while the bottom surface is assumed to be insulated. The top surface is a free surface interacting with the ambient air. Warm water enters the cavity from the inlet which is at the $x=0$ plane, h far from the free surface. Relatively cooler water is drained from the bottom of the opposite side of the cavity.

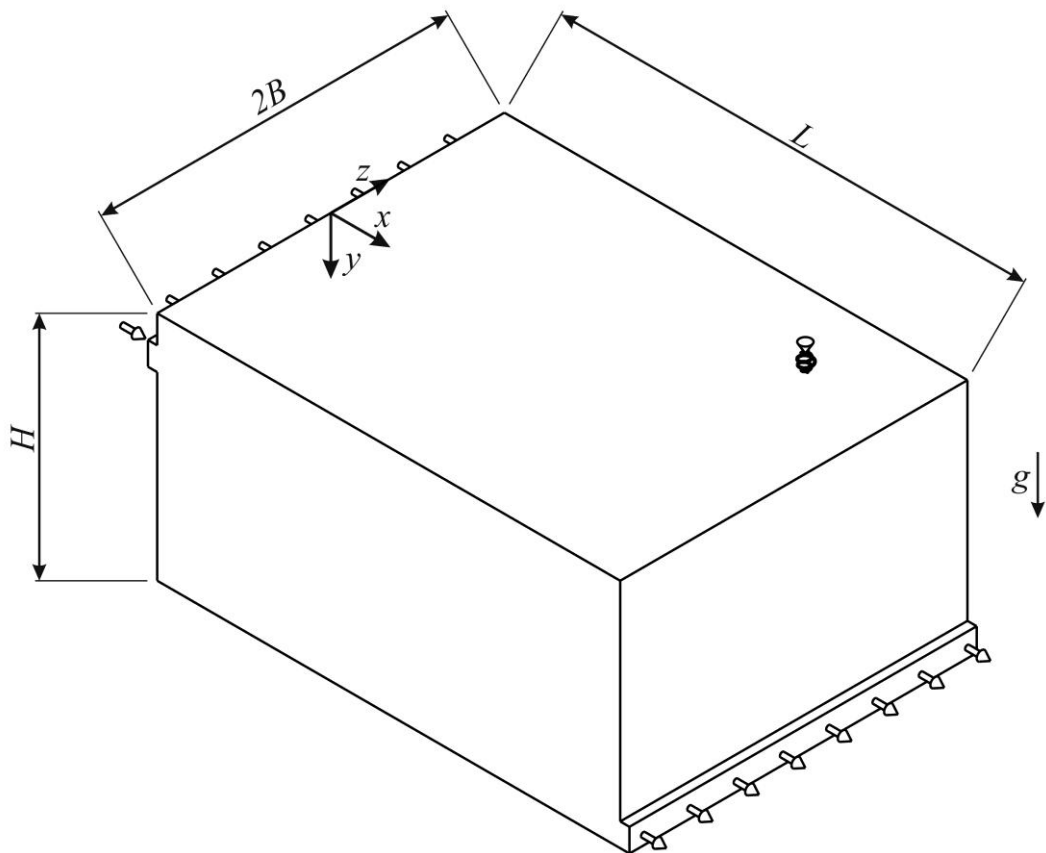


Fig. 3.1 Schematic of the Cavity

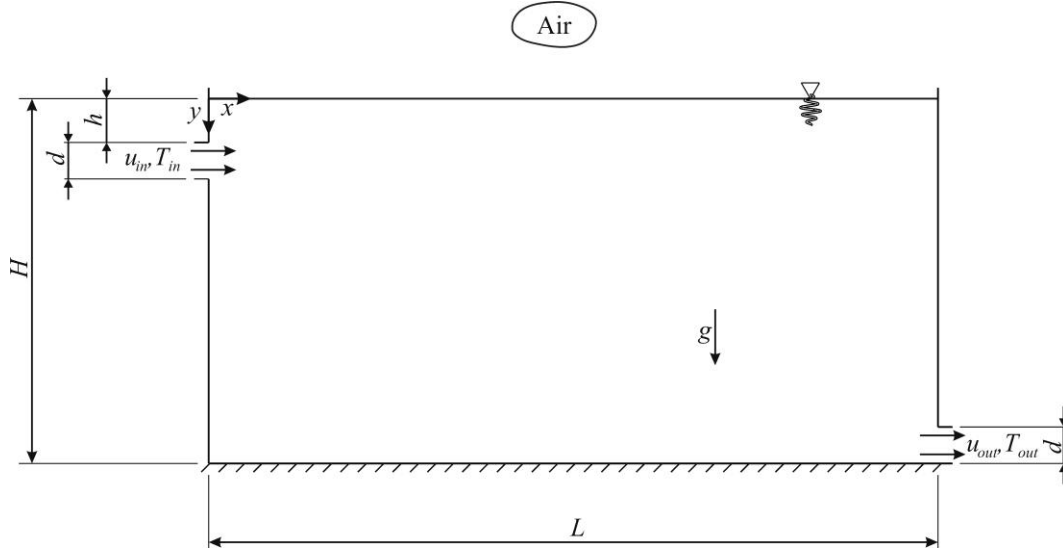


Fig. 3.2 Cross Section of the Cavity at a Constant z -plane

The flow is assumed to be laminar, 3 dimensional, unsteady; the fluid is incompressible (liquid water) and has constant properties. The governing equations with the employment of the Boussinesq approximation are (from Jaluria [18] and Yang [19])

$$\frac{\partial u}{\partial x} + \frac{\partial v}{\partial y} + \frac{\partial w}{\partial z} = 0 \quad (3.1)$$

$$\rho \frac{\partial u}{\partial t} + \rho u \frac{\partial u}{\partial x} + \rho v \frac{\partial u}{\partial y} + \rho w \frac{\partial u}{\partial z} = -\frac{\partial p}{\partial x} + \mu \left(\frac{\partial^2 u}{\partial x^2} + \frac{\partial^2 u}{\partial y^2} + \frac{\partial^2 u}{\partial z^2} \right) \quad (3.2)$$

$$\rho \frac{\partial v}{\partial t} + \rho u \frac{\partial v}{\partial x} + \rho v \frac{\partial v}{\partial y} + \rho w \frac{\partial v}{\partial z} = -\frac{\partial p}{\partial y} + \mu \left(\frac{\partial^2 v}{\partial x^2} + \frac{\partial^2 v}{\partial y^2} + \frac{\partial^2 v}{\partial z^2} \right) - \rho g \beta (T - T_{ic}) \quad (3.3)$$

$$\rho \frac{\partial w}{\partial t} + \rho u \frac{\partial w}{\partial x} + \rho v \frac{\partial w}{\partial y} + \rho w \frac{\partial w}{\partial z} = -\frac{\partial p}{\partial z} + \mu \left(\frac{\partial^2 w}{\partial x^2} + \frac{\partial^2 w}{\partial y^2} + \frac{\partial^2 w}{\partial z^2} \right) \quad (3.4)$$

$$\rho c \frac{\partial T}{\partial t} + \rho c u \frac{\partial T}{\partial x} + \rho c v \frac{\partial T}{\partial y} + \rho c w \frac{\partial T}{\partial z} = k \left(\frac{\partial^2 T}{\partial x^2} + \frac{\partial^2 T}{\partial y^2} + \frac{\partial^2 T}{\partial z^2} \right) \quad (3.5)$$

Where, T_{ic} is the initial uniform temperature of the cavity, β is the coefficient of thermal expansion of the fluid, and g is the gravitational acceleration.

The initial condition for the cavity is quiescent water in thermal equilibrium.

$$\begin{aligned} u(x, y, z, 0) = v(x, y, z, 0) = w(x, y, z, 0) = 0 \\ T(x, y, z, 0) = T_{ic} \end{aligned} \quad (3.6)$$

And the boundary conditions are; no slip and transient cooling boundaries at the vertical walls along the inlet and outlet and no-slip and constant wall temperature boundaries for the remaining two vertical side walls.

$$\begin{aligned} u(0, y, z, t) = v(0, y, z, t) = w(0, y, z, t) \\ = u(L, y, z, t) = v(L, y, z, t) = w(L, y, z, t) = 0 \\ \frac{\partial T}{\partial x}(0, y, z, t) = \frac{\partial T}{\partial x}(L, y, z, t) = \frac{q_{wl}(t)}{k} \end{aligned} \quad (3.7)$$

$$\begin{aligned} u(x, y, -B, t) = v(x, y, -B, t) = w(x, y, -B, t) \\ = u(x, y, B, t) = v(x, y, B, t) = w(x, y, B, t) = 0 \\ T(x, y, -B, t) = T(x, y, B, t) = T_{wl} \end{aligned} \quad (3.8)$$

Or instead of using one of the $z = \pm B$, $0 \leq x \leq L$, $0 \leq y \leq H$ boundaries, the symmetry at $z = 0$ plane can be used

$$\frac{\partial u}{\partial z}(x, y, 0, t) = \frac{\partial v}{\partial z}(x, y, 0, t) = \frac{\partial w}{\partial z}(x, y, 0, t) = \frac{\partial T}{\partial z}(x, y, 0, t) = 0 \quad (3.9)$$

The bottom surface will be treated as thermally insulated with the usual no-slip condition;

$$u(x, H, z, t) = v(x, H, z, t) = w(x, H, z, t) = \frac{\partial T}{\partial z}(x, H, z, t) = 0 \quad (3.10)$$

The velocity and the temperature of the fluid entering the cavity are specified

$$u = u_{in} \text{ and } T = T_{in} \quad (3.11)$$

at the inlet.

And the velocity at the outlet is equal to the velocity at the inlet and zero temperature gradient in the x – direction.

$$u = u_{in} \text{ and } \frac{\partial T}{\partial x} = 0 \quad (3.12)$$

though in the computations, velocity outlet is an unknown extrapolated from the exterior solution and balanced by overall mass balance for the cavity.

For the top surface, Jaluria [18] recommended no-shear velocity condition for the tangential directions of this surface;

$$\frac{\partial u}{\partial y}(x, 0, z, t) = v(x, 0, z, t) = \frac{\partial w}{\partial y}(x, 0, z, t) = 0 \quad (3.13)$$

The thermal boundary condition at the free surface is due to the total heat loss from this surface which changes with respect to time as the flow develops.

$$\frac{\partial T}{\partial y}(x, 0, z, t) = \frac{q_s(t)}{k} \quad (3.14)$$

Heat flux through the free surface includes evaporative and convective losses and solar gain.

$$q_s(t) = q_{conv}(t) + q_{evap}(t) - q_{solar}(t) \quad (3.15)$$

The convective heat transfer from the free-surface can be calculated by approximating the free surface to the upper surface of a heated plate at constant temperature although temperature of the free-surface varies. The Rayleigh number for the free surface is

$$Ra_L(t) = \frac{g \beta_{air} (T_s(t) - T_\infty) L}{\nu_{air} \alpha_{air}} \quad (3.16)$$

The thermophysical properties of air are evaluated at $T_f = (T_s + T_\infty)/2$ and L is the characteristic length of the free-surface defined by $L = A_s/P$. A_s is the surface area and P is the perimeter of the free-surface. The following average Nusselt number correlations recommended by Incropera [20] are used.

$$Nu_L(t) = 0.54 (Ra_L(t))^{1/4} \quad (10^4 \leq Ra_L \leq 10^7) \quad (3.17)$$

$$Nu_L(t) = 0.15 (Ra_L(t))^{1/3} \quad (10^7 \leq Ra_L \leq 10^{11}) \quad (3.18)$$

Hence the overall convective heat transfer coefficient and the convective heat transfer through the free surface are

$$h_{conv}(t) = Nu_L(t) \frac{k_{air}}{L} \quad (3.19)$$

$$q_{conv}(t) = h_{conv}(t) A_s (T_s(t) - T_\infty) \quad (3.20)$$

The computation of mass transfer coefficient involves utilization of heat and mass transfer analogy

$$\frac{h_{conv}(t)}{h_{evap}(t)} = \rho_{air} c_{p,air} \left(\frac{\alpha_{air}}{D_{AB}} \right)^{1-n} \quad (3.21)$$

Where D_{AB} is the binary diffusion coefficient of water vapor in atmospheric air. The recommended ([20]) value of n is 1/3. Once the mass convection coefficient is computed, then the rate of vaporization is calculated

$$\dot{m}_{evap}(t) = h_{evap}(t) A_s (\rho_w(@T_s(t)) - \phi \rho_w(@T_\infty)) \quad (3.22)$$

In the above equation, ϕ is relative humidity. The heat transfer accompanying the mass transfer is

$$q_{evap}(t) = \dot{m}_{evap}(t) h_{fg}(@T_s(t)) \quad (3.23)$$

The last term in equation (3.15) is heat transfer due to solar radiation. Solar radiation could be time dependent or assumed to be constant during the simulations.

$$q_{solar}(t) = q_{solar}''(t) A_s \quad (3.24)$$

To non-dimensionalize the governing equations, the height of the inlet d , the velocity of the charging fluid u_{in} , the temperature difference of the charging fluid, and the uniform initial temperature of the water body ($T_{in} - T_{ic}$) will be used;

$$\begin{aligned} X &= \frac{x}{d}, \quad Y = \frac{y}{d}, \quad Z = \frac{z}{d}, \quad U = \frac{u}{u_{in}}, \quad V = \frac{v}{u_{in}}, \quad W = \frac{w}{u_{in}} \\ \tau &= \frac{t}{\frac{d}{u_{in}}}, \quad P = \frac{p}{\rho u_{in}^2}, \quad \theta = \frac{T - T_{ic}}{T_{in} - T_{ic}} \end{aligned} \quad (3.25)$$

The governing equations become;

$$\frac{\partial U}{\partial X} + \frac{\partial V}{\partial Y} + \frac{\partial W}{\partial Z} = 0 \quad (3.26)$$

$$\frac{\partial U}{\partial \tau} + U \frac{\partial U}{\partial X} + V \frac{\partial U}{\partial Y} + W \frac{\partial U}{\partial Z} = -\frac{\partial P}{\partial X} + \frac{\nu}{U_i d} \left(\frac{\partial^2 U}{\partial X^2} + \frac{\partial^2 U}{\partial Y^2} + \frac{\partial^2 U}{\partial Z^2} \right) \quad (3.27)$$

$$\begin{aligned} \frac{\partial V}{\partial \tau} + U \frac{\partial V}{\partial X} + V \frac{\partial V}{\partial Y} + W \frac{\partial V}{\partial Z} \\ = -\frac{\partial P}{\partial Y} + \frac{\nu}{U_i d} \left(\frac{\partial^2 V}{\partial X^2} + \frac{\partial^2 V}{\partial Y^2} + \frac{\partial^2 V}{\partial Z^2} \right) - \frac{g \beta d (T_{in} - T_{ic})}{u_{in}^2} \theta \end{aligned} \quad (3.28)$$

$$\frac{\partial W}{\partial \tau} + U \frac{\partial W}{\partial X} + V \frac{\partial W}{\partial Y} + W \frac{\partial W}{\partial Z} = -\frac{\partial P}{\partial Z} + \frac{\nu}{U_i d} \left(\frac{\partial^2 W}{\partial X^2} + \frac{\partial^2 W}{\partial Y^2} + \frac{\partial^2 W}{\partial Z^2} \right) \quad (3.29)$$

$$\frac{\partial \theta}{\partial \tau} + U \frac{\partial \theta}{\partial X} + V \frac{\partial \theta}{\partial Y} + W \frac{\partial \theta}{\partial Z} = \frac{\alpha}{U_i d} \left(\frac{\partial^2 \theta}{\partial X^2} + \frac{\partial^2 \theta}{\partial Y^2} + \frac{\partial^2 \theta}{\partial Z^2} \right) \quad (3.30)$$

Where

$$\frac{\nu}{u_{in} d} = \frac{1}{Re} \quad (3.31)$$

$$\frac{g \beta d (T_{in} - T_{ic})}{u_{in}^2} = \frac{g \beta d^3 (T_{in} - T_{ic})}{\nu^2} \frac{\nu^2}{u_{in}^2 d^2} = \frac{Gr}{Re^2} \quad (3.32)$$

$$\frac{\alpha}{u_{in} d} = \frac{\alpha}{\nu} \frac{\nu}{u_{in} d} = \frac{1}{Pr} \frac{1}{Re} \quad (3.33)$$

The initial condition becomes

$$\begin{aligned} U(X, Y, Z, 0) = V(X, Y, Z, 0) = W(X, Y, Z, 0) = 0 \\ \theta(X, Y, Z, 0) = 0 \end{aligned} \quad (3.34)$$

The boundary conditions become;

Side surfaces containing the inlet and outlet:

$$\begin{aligned} U(0, Y, Z, \tau) = V(0, Y, Z, \tau) = W(0, Y, Z, \tau) \\ = U(L/d, Y, Z, \tau) = V(L/d, Y, Z, \tau) = W(L/d, Y, Z, \tau) = 0 \\ \frac{\partial \theta}{\partial X}(0, Y, Z, \tau) = \frac{\partial \theta}{\partial X}(L/d, Y, Z, \tau) = \frac{q_{wl}(t)}{k(T_{in} - T_{ic})} \end{aligned} \quad (3.35)$$

The other two side surfaces:

$$\begin{aligned}
 U(X, Y, -B/d, \tau) &= V(X, Y, -B/d, \tau) = W(X, Y, -B/d, \tau) \\
 &= U(X, Y, B/d, \tau) = V(X, Y, B/d, \tau) = W(X, Y, B/d, \tau) = 0 \\
 \theta(X, Y, -B/d, \tau) &= \theta(X, Y, B/d, \tau) = \frac{T_w - T_{ic}}{T_{in} - T_{ic}}
 \end{aligned} \tag{3.36}$$

Or the symmetry condition at $Z = 0$ plane

$$\frac{\partial U}{\partial Z}(X, Y, 0, \tau) = \frac{\partial V}{\partial Z}(X, Y, 0, \tau) = \frac{\partial W}{\partial Z}(X, Y, 0, \tau) = \frac{\partial \theta}{\partial Z}(X, Y, 0, \tau) = 0 \tag{3.37}$$

The bottom surface:

$$\begin{aligned}
 U(X, H/d, Z, \tau) &= V(X, H/d, Z, \tau) = W(X, H/d, Z, \tau) \\
 &= \frac{\partial \theta}{\partial Z}(X, H/d, Z, \tau) = 0
 \end{aligned} \tag{3.38}$$

The top surface:

$$\begin{aligned}
 \frac{\partial U}{\partial Y}(X, 0, Z, \tau) &= V(X, 0, Z, \tau) = \frac{\partial W}{\partial Y}(X, 0, Z, \tau) = 0 \\
 \frac{\partial \theta}{\partial Y}(X, 0, Z, \tau) &= \frac{q_s d}{k(T_{in} - T_{ic})}
 \end{aligned} \tag{3.39}$$

At the inlet

$$U = 1 \text{ and } \theta = 1 \tag{3.40}$$

And at the exit

$$U = 1 \text{ and } \frac{\partial \theta}{\partial X} = 0 \tag{3.41}$$

CHAPTER 4

FINITE VOLUME METHOD

4.1 Discretization of the Governing Equations

The momentum equations (3.2) to (3.4) are non-linear. Furthermore the y-momentum equation, equation (3.3) is coupled with the energy equation, equation (3.5). They are to be solved simultaneously in a continuous iterative manner. The transport equations (3.2) to (3.5) can be represented by the following general transport equation

$$\rho \frac{\partial \phi}{\partial t} + \rho u \frac{\partial \phi}{\partial x} + \rho v \frac{\partial \phi}{\partial y} + \rho w \frac{\partial \phi}{\partial z} = \Gamma \left(\frac{\partial^2 \phi}{\partial x^2} + \frac{\partial^2 \phi}{\partial y^2} + \frac{\partial^2 \phi}{\partial z^2} \right) + S \quad (4.1)$$

where ϕ is the transport variable, Γ is the diffusion coefficient, and S is called the source function. The corresponding counterparts within the governing equations are tabulated in Table 4.1.

Table 4.1 Transport Variables, Diffusion Coefficients, and Source Functions for Governing Equations

	ϕ	Γ	S
x-momentum Equation	u	μ	$-\frac{\partial p}{\partial x}$
y-momentum Equation	v	μ	$-\frac{\partial p}{\partial y} - \rho g \beta (T - T_{ic})$
z-momentum Equation	w	μ	$-\frac{\partial p}{\partial z}$
Energy Equation	T	$\frac{k}{c}$	0

If in equation (4.1) velocities u , v , and w are known, or in the solution of continuously iterative FVM they assumed to be equal to the velocity values of the previous iteration, the non-linearities of equation (4.1) can be avoided.

In the discretization process of the general transport equation, the following (Fig. 4.1) arbitrary three-dimensional rectangular control volume is to be used. A two-dimensional grid is also shown in Fig. 4.2 for clarity.

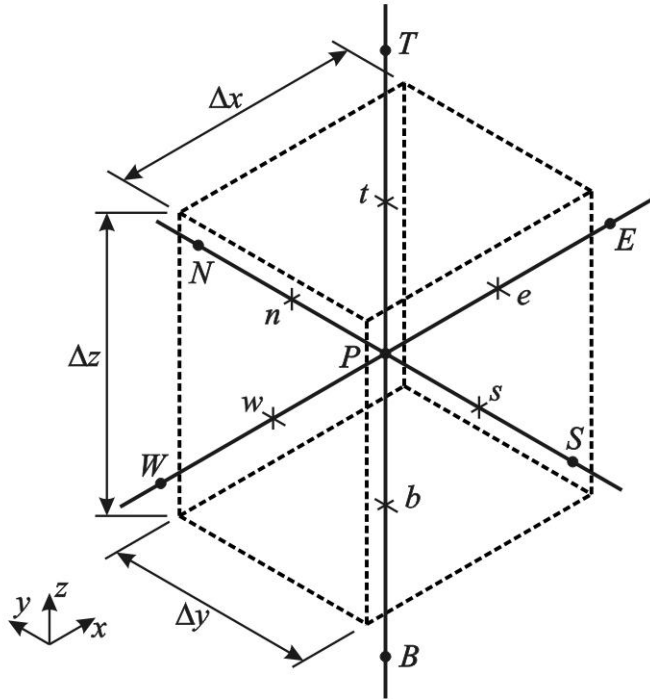


Fig. 4.1 An Arbitrary Portion of the 3D Grid

A general grid point (or node) P has east (E) and west (W) neighbors in x -direction, north (N) and south (S) neighbors in y -direction, and top (T) and bottom (B) neighbors in z -direction. The grid point P is located beforehand and the cell faces e , w , n , s , t , and b are placed such that they are positioned midway between grid points (hence Δx_{wP} need not equal to Δx_{Pe} , yet $\Delta x_{wP} = \Delta x_{Ww}$ and $\Delta x_{Pe} = \Delta x_{eE}$). This is called cell-vertex scheme.

The grid point P could also be put on the geometric center of a control volume and that approach is called cell-centered scheme. Since in Finite Volume Method, values at the grid points are assumed to be the representative values of the whole control volume, cell-centered scheme has the advantage of better representing grid point values over the

control volume whereas cell-vertex scheme has the advantage of approximating the flux values at the control surfaces better.

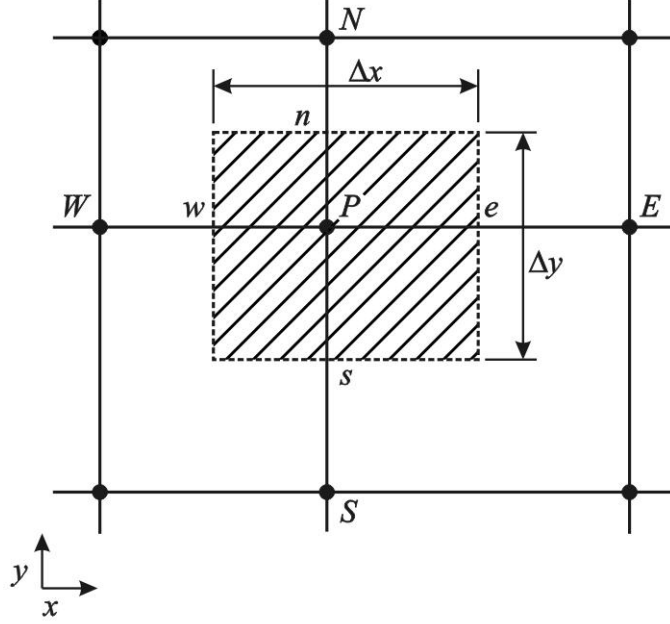


Fig. 4.2 An Arbitrary Portion of the 2D Grid

The control volume integration (the key step of the finite volume method that distinguishes it from all other CFD techniques, Versteeg and Malalasekera [21]) of the general transport equation, equation (4.1) is performed spatially over this control volume defined by cell-vertex scheme and also temporally over a time increment Δt . The integrated form of equation (4.1) is

$$\begin{aligned}
 & \int_t^{t+\Delta t} \left(\int_{CV} \rho \frac{\partial \phi}{\partial t} dV \right) dt + \int_t^{t+\Delta t} \left(\int_{CV} \rho u \frac{\partial \phi}{\partial x} dV \right) dt + \int_t^{t+\Delta t} \left(\int_{CV} \rho v \frac{\partial \phi}{\partial y} dV \right) dt \\
 & + \int_t^{t+\Delta t} \left(\int_{CV} \rho w \frac{\partial \phi}{\partial z} dV \right) dt = \int_t^{t+\Delta t} \left(\int_{CV} \Gamma \frac{\partial^2 \phi}{\partial x^2} dV \right) dt + \int_t^{t+\Delta t} \left(\int_{CV} \Gamma \frac{\partial^2 \phi}{\partial y^2} dV \right) dt \quad (4.2) \\
 & + \int_t^{t+\Delta t} \left(\int_{CV} \Gamma \frac{\partial^2 \phi}{\partial z^2} dV \right) dt + \int_t^{t+\Delta t} \left(\int_{CV} S dV \right) dt
 \end{aligned}$$

Assuming the value of ϕ at the grid point P prevails over the whole control volume and changing the order of integration for the unsteady term, the unsteady term becomes

$$\int_t^{t+\Delta t} \left(\int_{CV} \rho \frac{\partial \phi}{\partial t} dV \right) dt = \int_{CV} \left(\int_t^{t+\Delta t} \rho \frac{\partial \phi}{\partial t} dt \right) dV = \rho (\phi_P - \phi_P^0) \Delta V \quad (4.3)$$

Where ϕ_P and ϕ_P^0 are the values of ϕ at the grid point P at time $t + \Delta t$ and t respectively.

In the treatment of the diffusion terms, the volume integrals are converted to surface integrals by the divergence theorem, for example the diffusion term in the x -direction becomes

$$\int_t^{t+\Delta t} \left(\int_{CV} \Gamma \frac{\partial^2 \phi}{\partial x^2} dV \right) dt = \int_t^{t+\Delta t} \left[\left(\Gamma A \frac{\partial \phi}{\partial x} \right)_e - \left(\Gamma A \frac{\partial \phi}{\partial x} \right)_w \right] dt \quad (4.4)$$

The diffusion coefficient is constant according to our previous assumptions, also the eastern and western control surface areas are the same ($A_e = A_w = A_{yz}$). The gradient of ϕ at the control surfaces is approximated by central differencing

$$\left(\frac{\partial \phi}{\partial x} \right)_e = \frac{\phi_E - \phi_P}{\Delta x_{PE}} \quad (4.5)$$

$$\left(\frac{\partial \phi}{\partial x} \right)_w = \frac{\phi_P - \phi_W}{\Delta x_{WP}} \quad (4.6)$$

Equation (4.4) now becomes

$$\int_t^{t+\Delta t} \left(\int_{CV} \Gamma \frac{\partial^2 \phi}{\partial x^2} dV \right) dt = \Gamma A_{yz} \int_t^{t+\Delta t} \left[\left(\frac{\phi_E - \phi_P}{\Delta x_{PE}} \right) - \left(\frac{\phi_P - \phi_W}{\Delta x_{WP}} \right) \right] dt \quad (4.7)$$

In the evaluation of the time integral, if the temporal variation of ϕ is assumed such that the new value (value at time is equal to $t + \Delta t$) prevails during the time increment, the temporal discretization is called the fully implicit discretization scheme. The fully implicit scheme is unconditionally stable and it is the preferred scheme in numerical analysis. The diffusion term is now transformed to its final discretized form as

$$\int_t^{t+\Delta t} \left(\int_{CV} \Gamma \frac{\partial^2 \phi}{\partial x^2} dV \right) dt = \Gamma A_{yz} \Delta t \left[\left(\frac{\phi_E - \phi_P}{\Delta x_{PE}} \right) - \left(\frac{\phi_P - \phi_W}{\Delta x_{WP}} \right) \right] \quad (4.8)$$

Similarly the diffusion terms in the y - and z -directions are;

$$\int_t^{t+\Delta t} \left(\int_{CV} \Gamma \frac{\partial^2 \phi}{\partial y^2} dV \right) dt = \Gamma A_{xz} \Delta t \left[\left(\frac{\phi_N - \phi_P}{\Delta y_{PN}} \right) - \left(\frac{\phi_P - \phi_S}{\Delta y_{SP}} \right) \right] \quad (4.9)$$

$$\int_t^{t+\Delta t} \left(\int_{CV} \Gamma \frac{\partial^2 \phi}{\partial z^2} dV \right) dt = \Gamma A_{xy} \Delta t \left[\left(\frac{\phi_T - \phi_P}{\Delta z_{PT}} \right) - \left(\frac{\phi_P - \phi_B}{\Delta z_{BP}} \right) \right] \quad (4.10)$$

When the divergence theorem is applied to the first convective term of equation (4.2) and fully implicit scheme is utilized for the temporal variation of ϕ .

$$\begin{aligned} \int_t^{t+\Delta t} \left(\int_{CV} \rho u \frac{\partial \phi}{\partial x} dV \right) dt &= \int_t^{t+\Delta t} [(\rho u A \phi)_e - (\rho u A \phi)_w] dt \\ &= \rho u_e A_{yz} \phi_e \Delta t - \rho u_w A_{yz} \phi_w \Delta t \end{aligned} \quad (4.11)$$

The values ϕ_e and ϕ_w are the values of ϕ at the east and west control surfaces of the control volume. They must be interpolated from the grid point values by a suitable scheme. Several schemes of interpolation exist such as central differencing scheme, upwind scheme (upstream difference scheme, donor-cell method), the hybrid differencing scheme of Spalding [22], the power law scheme of Patankar [23], the quadratic upstream interpolation for convective kinetics (QUICK) scheme of Leonard [24].

In upwind differencing scheme, the face values (or control surface values) are simply replaced by the grid point values from where the flow approaches to the control faces of the control volume, hence,

$$\phi_e = \phi_P \quad \text{if } u_e > 0 \quad (4.12)$$

$$\phi_e = \phi_E \quad \text{if } u_e < 0 \quad (4.13)$$

$$\phi_w = \phi_W \quad \text{if } u_w > 0 \quad (4.14)$$

$$\phi_w = \phi_P \quad \text{if } u_w < 0 \quad (4.15)$$

In other words

$$\phi_e = \phi_P \frac{\max(u_e, 0)}{u_e} - \phi_E \frac{\max(-u_e, 0)}{u_e} \quad (4.16)$$

$$\phi_w = \phi_W \frac{\max(u_w, 0)}{u_w} - \phi_P \frac{\max(-u_w, 0)}{u_w} \quad (4.17)$$

where the function \max is simply

$$\max(x, y) \begin{cases} = x & \text{if } x > y \\ = y & \text{if } x < y \end{cases} \quad (4.18)$$

The convective term of equation (4.11) becomes

$$\int_t^{t+\Delta t} \left(\int_{CV} \rho u \frac{\partial \phi}{\partial x} dV \right) dt = \rho A_{yz} \Delta t \begin{bmatrix} \phi_P \max(u_e, 0) - \phi_E \max(-u_e, 0) \\ -\phi_W \max(u_w, 0) + \phi_P \max(-u_w, 0) \end{bmatrix} \quad (4.19)$$

Similar treatment for the other two convective terms reveals,

$$\int_t^{t+\Delta t} \left(\int_{CV} \rho v \frac{\partial \phi}{\partial y} dV \right) dt = \rho A_{xz} \Delta t \begin{bmatrix} \phi_P \max(u_n, 0) - \phi_N \max(-u_n, 0) \\ -\phi_S \max(u_s, 0) + \phi_P \max(-u_s, 0) \end{bmatrix} \quad (4.20)$$

$$\int_t^{t+\Delta t} \left(\int_{CV} \rho w \frac{\partial \phi}{\partial z} dV \right) dt = \rho A_{xy} \Delta t \begin{bmatrix} \phi_P \max(u_t, 0) - \phi_T \max(-u_t, 0) \\ -\phi_B \max(u_b, 0) + \phi_P \max(-u_b, 0) \end{bmatrix} \quad (4.21)$$

The last term in equation (4.2) is the source term and it could be discretized as

$$\int_t^{t+\Delta t} \left(\int_{CV} S dV \right) dt = \bar{S} \Delta t \Delta V \quad (4.22)$$

where \bar{S} is the C.V. average value of S at time $t + \Delta t$. Actually embedding the pressure gradient within the source function is only sufficient for the time being. During the primitive variables formulation, the pressure gradient will be dealt separately.

Plugging in the discretized unsteady, convective, diffusive, and source terms into the finite volume integrated general transport equation (4.2)

$$\begin{aligned}
& \rho(\phi_P - \phi_P^0)\Delta V + \rho A_{yz}\Delta t \left[\begin{aligned} & \phi_P \max(u_e, 0) - \phi_E \max(-u_e, 0) \\ & -\phi_W \max(u_w, 0) + \phi_P \max(-u_w, 0) \end{aligned} \right] \\
& + \rho A_{xz}\Delta t \left[\begin{aligned} & \phi_P \max(v_n, 0) - \phi_N \max(-v_n, 0) \\ & -\phi_S \max(v_s, 0) + \phi_P \max(-v_s, 0) \end{aligned} \right] \\
& + \rho A_{xy}\Delta t \left[\begin{aligned} & \phi_P \max(w_t, 0) - \phi_T \max(-w_t, 0) \\ & -\phi_B \max(w_b, 0) + \phi_P \max(-w_b, 0) \end{aligned} \right] \\
& = \Gamma A_{yz}\Delta t \left[\left(\frac{\phi_E - \phi_P}{\Delta x_{PE}} \right) - \left(\frac{\phi_P - \phi_W}{\Delta x_{WP}} \right) \right] \\
& + \Gamma A_{xz}\Delta t \left[\left(\frac{\phi_N - \phi_P}{\Delta y_{PN}} \right) - \left(\frac{\phi_P - \phi_S}{\Delta y_{SP}} \right) \right] \\
& + \Gamma A_{xy}\Delta t \left[\left(\frac{\phi_T - \phi_P}{\Delta z_{PT}} \right) - \left(\frac{\phi_P - \phi_B}{\Delta z_{BP}} \right) \right] + \bar{S}\Delta t\Delta V
\end{aligned} \tag{4.23}$$

To simplify the formulation, F indicating the strength of convection and D , the diffusion conductance are defined (Patankar [23])

$$F = \rho u A_{CS} \tag{4.24}$$

$$D = \frac{\Gamma A_{CS}}{\Delta x} \tag{4.25}$$

With the help of equations (4.24) and (4.25) and some rearrangements, equation (4.23) becomes

$$a_P \phi_P = a_E \phi_E + a_W \phi_W + a_N \phi_N + a_S \phi_S + a_T \phi_T + a_B \phi_B + b \tag{4.26}$$

where

$$a_E = \max(-F_e, 0) + D_e \tag{4.27}$$

$$a_W = \max(F_w, 0) + D_w \tag{4.28}$$

$$a_N = \max(-F_n, 0) + D_n \tag{4.29}$$

$$a_S = \max(F_s, 0) + D_s \tag{4.30}$$

$$a_T = \max(-F_t, 0) + D_t \tag{4.31}$$

$$a_B = \max(F_b, 0) + D_b \tag{4.32}$$

$$a_p^0 = \rho \frac{\Delta V}{\Delta t} \quad (4.33)$$

$$b = \rho \phi_p^0 \frac{\Delta V}{\Delta t} + \bar{S} \Delta V \quad (4.34)$$

and

$$a_p = a_E + a_W + a_N + a_S + a_T + a_B + a_p^0 + (F_e - F_w) + (F_n - F_s) + (F_t - F_b) \quad (4.35)$$

The form of the final discretized equation (equation (4.26)) of the control volume integrated general transport equation (equation 4.2) does not change together with equations (4.33) through (4.35) when a different interpolation scheme is used for the discretization of convective terms, only the coefficients in equations (4.27) through (4.32) change. Patankar's [23] hybrid differencing scheme (which is favored over the upwind differencing scheme [21], [23]) for example will yield the following neighboring nodal coefficients.

$$a_E = \max \left[-F_e, \left(D_e - \frac{F_e}{2} \right), 0 \right] \quad (4.36)$$

$$a_W = \max \left[F_w, \left(D_w + \frac{F_w}{2} \right), 0 \right] \quad (4.37)$$

$$a_N = \max \left[-F_n, \left(D_n - \frac{F_n}{2} \right), 0 \right] \quad (4.38)$$

$$a_S = \max \left[F_s, \left(D_s + \frac{F_s}{2} \right), 0 \right] \quad (4.39)$$

$$a_T = \max \left[-F_t, \left(D_t - \frac{F_t}{2} \right), 0 \right] \quad (4.40)$$

$$a_B = \max \left[F_b, \left(D_b + \frac{F_b}{2} \right), 0 \right] \quad (4.41)$$

The definition of the hybrid differencing scheme and the derivation of the corresponding coefficients, equations (4.36) through (4.41), are supplied in APPENDIX A.

4.2 Staggered Grid

In the solution of the coupled governing equations using primitive variables, staggered grid utilization is recommended [23, 21]. The velocities and scalar variables (pressure and temperature) are stored at different locations of the grid. Simply u velocity nodes are defined at the western and eastern faces of a scalar control volume (correspondingly the scalar nodes are defined at the western and eastern faces of a u velocity control volume), similarly v velocity nodes are defined at the northern and southern faces of a scalar control volume and w velocity nodes are defined at the top and bottom faces of a scalar control volume. Fig. 4.3 demonstrates a 2D backward staggered grid.

In the 2D staggered grid, scalar grid point is at (I, J) , scalar control volume (or scalar cell) is in the region $i < x < i+1$ and $j < y < j+1$. The u velocity grid point is at (i, J) , and the u -cell is in the region $I-1 < x < I$ and $j < y < j+1$. The v velocity grid point is at (I, j) , and the v -cell is in the region $i < x < i+1$ and $J-1 < y < J$. The neighbor nodes and face nodes for the four cells are presented in Table 4.2.

The strength of convection, for example, at the west face of a u -cell is

$$F_{w_u} = F_{I-1, J, K} = \frac{F_{i-1, J, K} + F_{i, J, K}}{2}$$

by linear interpolation since the west face node of a u -cell is a scalar node and does not contain u velocity data. Strength of convection at the west face of a scalar cell is simply

$$F_{w_T} = F_{i, J, K}$$

since the west face of a scalar cell is a u velocity node which contains the u velocity data.

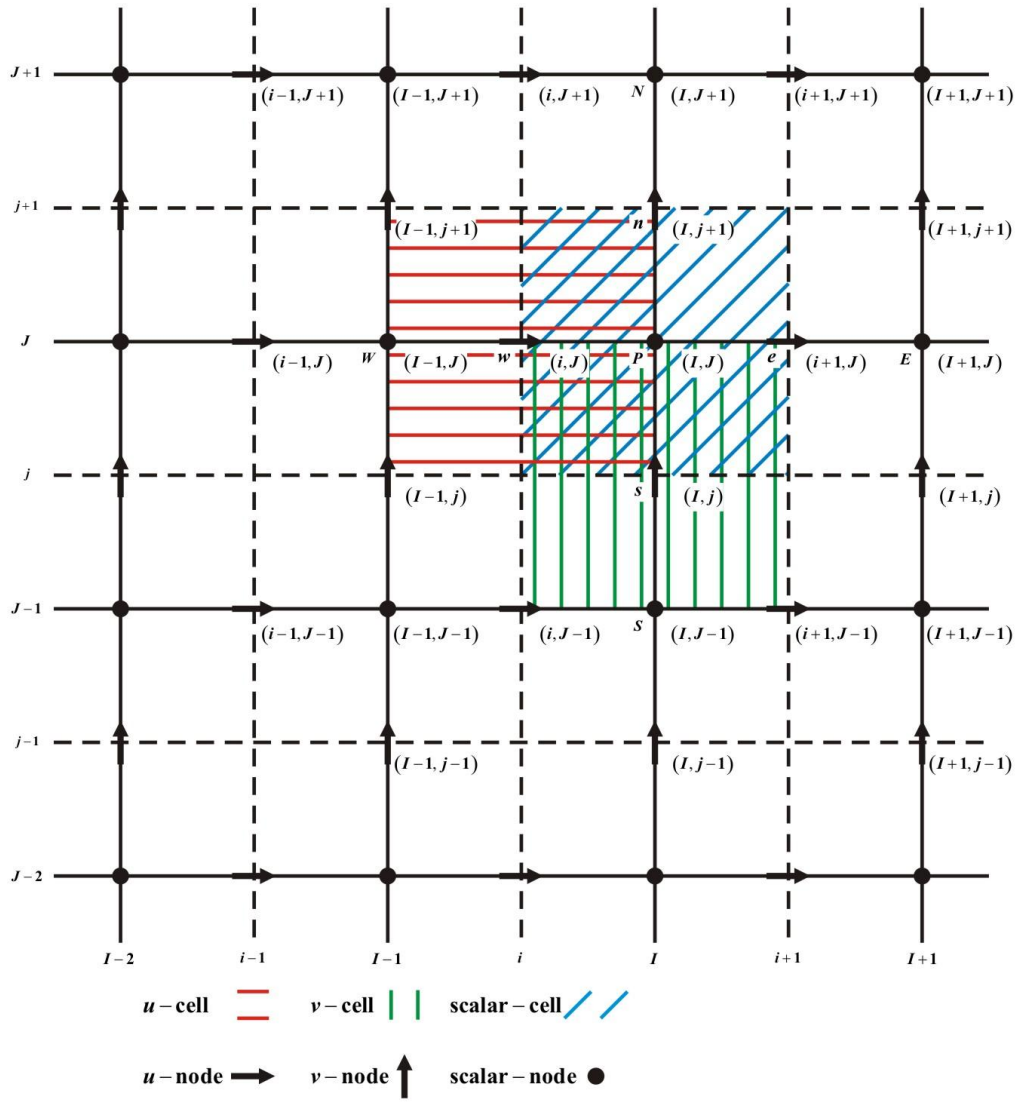


Fig. 4.3 2D Backward Staggered Grid

Table 4.2 Staggered Grid Point Locations for the Velocity Cells and the Scalar Cell

	u -cell	v -cell	w -cell	T -cell
P	(i, J, K)	(I, j, K)	(I, J, k)	(I, J, K)
E	$(i+1, J, K)$	$(I+1, j, K)$	$(I+1, J, k)$	$(I+1, J, K)$
W	$(i-1, J, K)$	$(I-1, j, K)$	$(I-1, J, k)$	$(I-1, J, K)$
N	$(i, J+1, K)$	$(I, j+1, K)$	$(I, J+1, k)$	$(I, J+1, K)$
S	$(i, J-1, K)$	$(I, j-1, K)$	$(I, J-1, k)$	$(I, J-1, K)$
T	$(i, J, K+1)$	$(I, j, K+1)$	$(I, J, k+1)$	$(I, J, K+1)$
B	$(i, J, K-1)$	$(I, j, K-1)$	$(I, J, k-1)$	$(I, J, K-1)$
e	(I, J, K)	$(i+1, j, K)$	$(I+1, J, k)$	$(i+1, J, K)$
w	$(I-1, J, K)$	$(i-1, j, K)$	$(I-1, J, k)$	(i, J, K)
n	$(i, j+1, K)$	(I, J, K)	$(I, j+1, k)$	$(I, j+1, K)$
s	$(i, j-1, K)$	$(I, J-1, K)$	$(I, j-1, k)$	$(I, j-1, K)$
t	$(i, J, k+1)$	$(I, j, k+1)$	(I, J, K)	$(I, J, k+1)$
b	$(i, J, k-1)$	$(I, j, k-1)$	$(I, J, K-1)$	$(I, J, k-1)$

4.3 The Discretized Forms of the Governing Equations in Staggered Grid

Equation (4.26) can be modified in order to conform to the backward staggered grid. The three momentum equations and the energy equation when the pressure gradient terms are extracted from the source terms can be written as

$$a_{i,J,K}u_{i,J,K} = \sum a_{nb}u_{nb} + (p_{I-1,J,K} - p_{I,J,K})A_{i,J,K} + b_{i,J,K} \quad (4.42)$$

$$a_{I,j,K}v_{I,j,K} = \sum a_{nb}v_{nb} + (p_{I,J-1,K} - p_{I,J,K})A_{I,j,K} + b_{I,j,K} \quad (4.43)$$

$$a_{I,J,k}w_{I,J,k} = \sum a_{nb}w_{nb} + (p_{I,J,K-1} - p_{I,J,K})A_{I,J,k} + b_{I,J,k} \quad (4.44)$$

$$a_{I,J,K}T_{I,J,K} = \sum a_{nb}T_{nb} + b_{I,J,K} \quad (4.45)$$

4.4 The SIMPLE Algorithm

In the above equations, pressure should be known in order to calculate the other transport variables. The Semi-Implicit Method for Pressure-Linked Equations was first described

by Patankar and Spalding [25] which is a guess-and-correct algorithm to calculate the pressure. At first, a pressure field p^* is guessed and the momentum equations (4.42) to (4.44) are solved to obtain velocity components corresponding to the guessed pressure field.

$$a_{i,j,k}u_{i,j,k}^* = \sum a_{nb}u_{nb}^* + (p_{i-1,j,k}^* - p_{i,j,k}^*)A_{i,j,k} + b_{i,j,k} \quad (4.46)$$

$$a_{l,j,k}v_{l,j,k}^* = \sum a_{nb}v_{nb}^* + (p_{l,j-1,k}^* - p_{l,j,k}^*)A_{l,j,k} + b_{l,j,k} \quad (4.47)$$

$$a_{l,j,k}w_{l,j,k}^* = \sum a_{nb}w_{nb}^* + (p_{l,j,k-1}^* - p_{l,j,k}^*)A_{l,j,k} + b_{l,j,k} \quad (4.48)$$

Hence, there are differences between the correct velocity components and the ones computed from the guessed pressure field. Also, there is a difference between the correct pressure and the guessed pressure.

$$p = p^* + p' \quad (4.49)$$

$$u = u^* + u' \quad (4.50)$$

$$v = v^* + v' \quad (4.51)$$

$$w = w^* + w' \quad (4.52)$$

The primed velocities and the pressure are the velocity corrections and pressure correction. If equations (4.46) to (4.48) are subtracted from equations (4.42) to (4.44), the following equations are gained

$$a_{i,j,k}u'_{i,j,k} = \sum a_{nb}u'_{nb} + (p'_{i-1,j,k} - p'_{i,j,k})A_{i,j,k} \quad (4.53)$$

$$a_{l,j,k}v'_{l,j,k} = \sum a_{nb}v'_{nb} + (p'_{l,j-1,k} - p'_{l,j,k})A_{l,j,k} \quad (4.54)$$

$$a_{l,j,k}w'_{l,j,k} = \sum a_{nb}w'_{nb} + (p'_{l,j,k-1} - p'_{l,j,k})A_{l,j,k} \quad (4.55)$$

The main approximation of the SIMPLE method is the omission of the first terms on the right hand side of equations (4.53) to (4.55). The reasons of this omission are discussed by the developer of the procedure [23]. The velocity correction equations now become:

$$u'_{i,j,k} = d_{i,j,k} (p'_{i-1,j,k} - p'_{i,j,k}) \quad (4.56)$$

$$v'_{l,j,k} = d_{l,j,k} (p'_{l,j-1,k} - p'_{l,j,k}) \quad (4.57)$$

$$w'_{I,J,k} = d_{I,J,k} (p'_{I,J,K-1} - p'_{I,J,K}) \quad (4.58)$$

Equations (4.50) to (4.52) now become

$$u_{i,J,K} = u_{i,J,K}^* + d_{i,J,K} (p'_{I-1,J,K} - p'_{I,J,K}) \quad (4.59)$$

$$v_{I,j,K} = v_{I,j,K}^* + d_{I,j,K} (p'_{I,J-1,K} - p'_{I,J,K}) \quad (4.60)$$

$$w_{I,J,k} = w_{I,J,k}^* + d_{I,J,k} (p'_{I,J,K-1} - p'_{I,J,K}) \quad (4.61)$$

Thus, if the pressure correction can be calculated e.g. from the continuity equation, equations (4.59) to (4.61) could be used in order to compute the correct velocity field. For this purpose, mass conservation equation (equation (3.1)) is discretized for the scalar cell (T -cell).

$$\begin{aligned} & \left[(\rho u A)_{i+1,J,K} - (\rho u A)_{i,J,K} \right] + \left[(\rho v A)_{I,j+1,K} - (\rho v A)_{I,j,K} \right] \\ & + \left[(\rho w A)_{I,J,k+1} - (\rho w A)_{I,J,k} \right] = 0 \end{aligned} \quad (4.62)$$

Putting the correct velocities (with necessary indicial operations) of equations (4.59) to (4.61) into the discretized continuity equation (4.62) gives

$$\begin{aligned} & \left[(\rho A)_{i+1,J,K} (u_{i+1,J,K}^* + d_{i+1,J,K} (p'_{I,J,K} - p'_{I+1,J,K})) \right] \\ & - \left[(\rho A)_{i,J,K} (u_{i,J,K}^* + d_{i,J,K} (p'_{I-1,J,K} - p'_{I,J,K})) \right] \\ & + \left[(\rho A)_{I,j+1,K} (v_{I,j+1,K}^* + d_{I,j+1,K} (p'_{I,J,K} - p'_{I,J+1,K})) \right] \\ & - \left[(\rho A)_{I,j,K} (v_{I,j,K}^* + d_{I,j,K} (p'_{I,J-1,K} - p'_{I,J,K})) \right] \\ & + \left[(\rho A)_{I,J,k+1} (w_{I,J,k+1}^* + d_{I,J,k+1} (p'_{I,J,K} - p'_{I,J,K+1})) \right] \\ & - \left[(\rho A)_{I,J,k} (w_{I,J,k}^* + d_{I,J,k} (p'_{I,J,K-1} - p'_{I,J,K})) \right] = 0 \end{aligned} \quad (4.63)$$

After some rearrangements, the pressure correction equation is obtained

$$\begin{aligned} a_{I,J,K} p'_{I,J,K} &= a_{I+1,J,K} p'_{I+1,J,K} + a_{I-1,J,K} p'_{I-1,J,K} + a_{I,J+1,K} p'_{I,J+1,K} \\ &+ a_{I,J-1,K} p'_{I,J-1,K} + a_{I,J,K+1} p'_{I,J,K+1} + a_{I,J,K-1} p'_{I,J,K-1} + b'_{I,J,K} \end{aligned} \quad (4.64)$$

where

$$a_{I,J,K} = a_{I+1,J,K} + a_{I-1,J,K} + a_{I,J+1,K} + a_{I,J-1,K} + a_{I,J,K+1} + a_{I,J,K-1} \quad (4.65)$$

$$a_{I+1,J,K} = (\rho dA)_{i+1,J,K} \quad (4.66)$$

$$a_{I-1,J,K} = (\rho dA)_{i-1,J,K} \quad (4.67)$$

$$a_{I,J+1,K} = (\rho dA)_{I,j+1,K} \quad (4.68)$$

$$a_{I,J-1,K} = (\rho dA)_{I,j-1,K} \quad (4.69)$$

$$a_{I,J,K+1} = (\rho dA)_{I,J,k+1} \quad (4.70)$$

$$a_{I,J,K-1} = (\rho dA)_{I,J,k-1} \quad (4.71)$$

$$b'_{I,J,K} = \left[(\rho u^* A)_{i,J,K} - (\rho u^* A)_{i+1,J,K} \right] + \left[(\rho v^* A)_{I,j,K} - (\rho v^* A)_{I,j+1,K} \right] \\ + \left[(\rho w^* A)_{I,J,k} - (\rho w^* A)_{I,J,k+1} \right] \quad (4.72)$$

The SIMPLE algorithm flow chart is presented in Fig. 4.4.

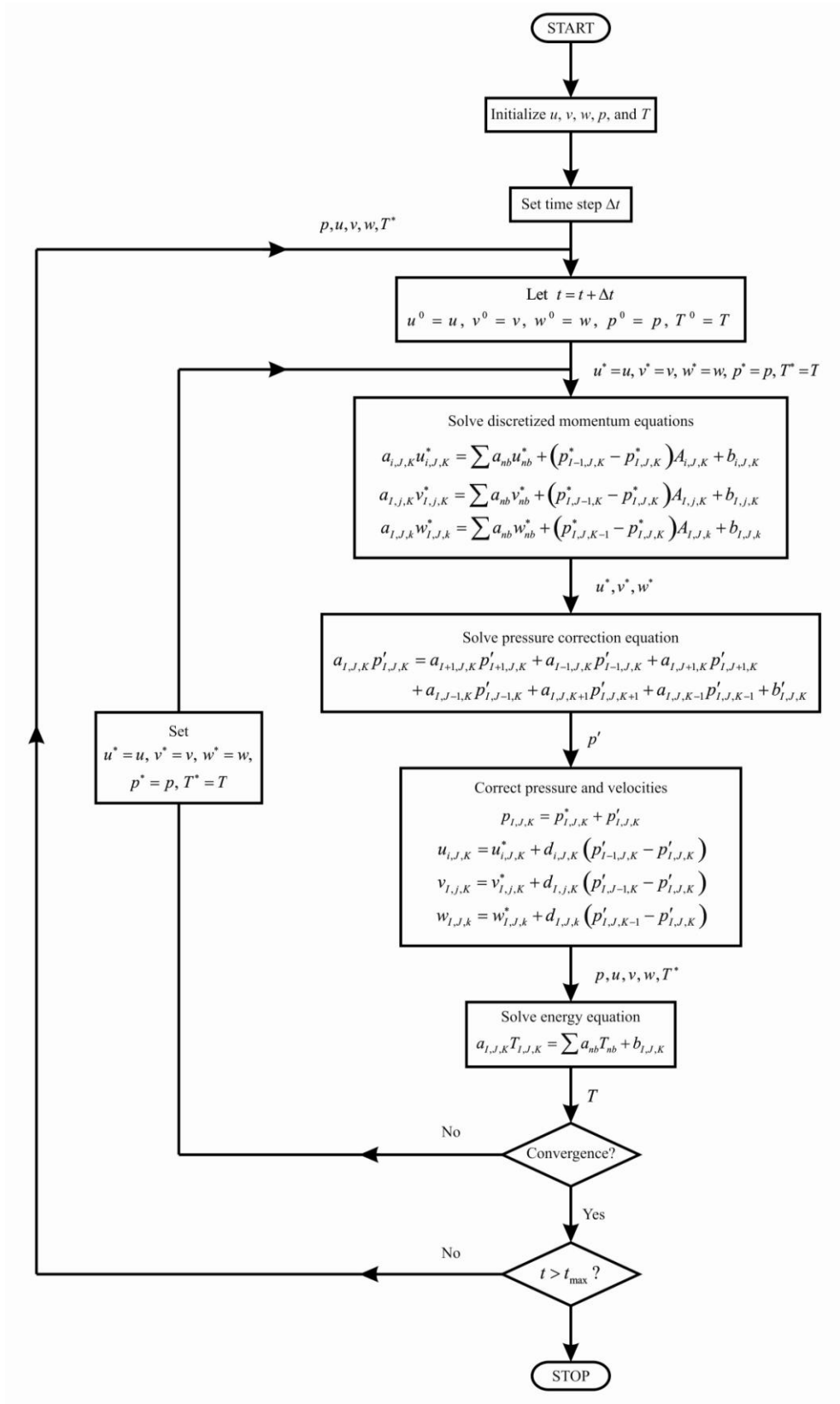


Fig. 4.4 The SIMPLE Algorithm (Adapted from [21])

4.5 Boundary Conditions

A portion of the inlet to the cavity is shown in Fig. 4.5 in 2D viewpoint for ease of demonstration. The inlet is at $i=1$. The inlet boundary value u_{in} is stored at the grids with $i=1$, and the solution of x -momentum equation (4.42) is started from $i=2$ onwards in the x -direction. Hence in the figure a typical u -cell feeling the effect of the inlet boundary condition at first hand is at $(i=2, nw+1, K)$, and its western neighbor grid is simply the inlet boundary condition. The rest of the boundary conditions are stored at $I=0$ ($v_{in} = w_{in} = p'_{in} = 0$ and the specified inlet temperature T_{in}) and the governing equations are solved from $I=1$ onwards. Furthermore, for the pressure correction equation at the scalar grid point $a_w = 0$ and $u_w^* = u_w$ in equation (4.72).

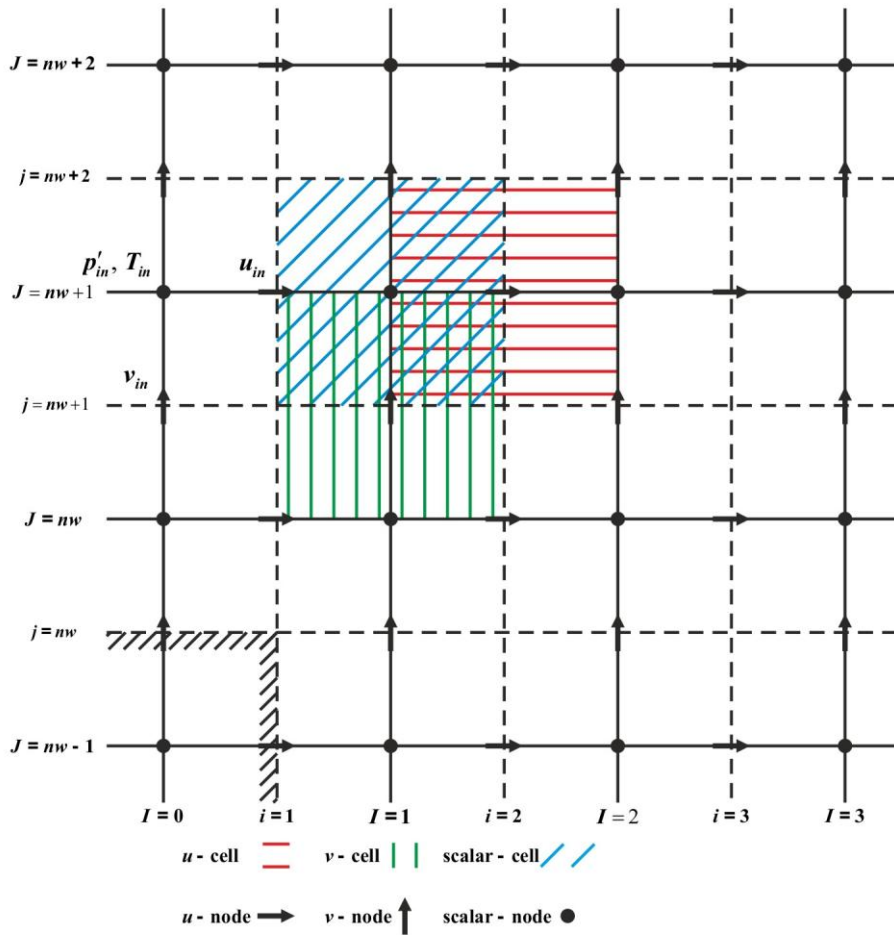


Fig. 4.5 Inlet Boundary Discretization

Exit boundary is shown in Fig. 4.6. The u velocity B.C. is kept at $i = NX + 1$. Thus the x – momentum equation is solved up to the grids having $i = NX$.

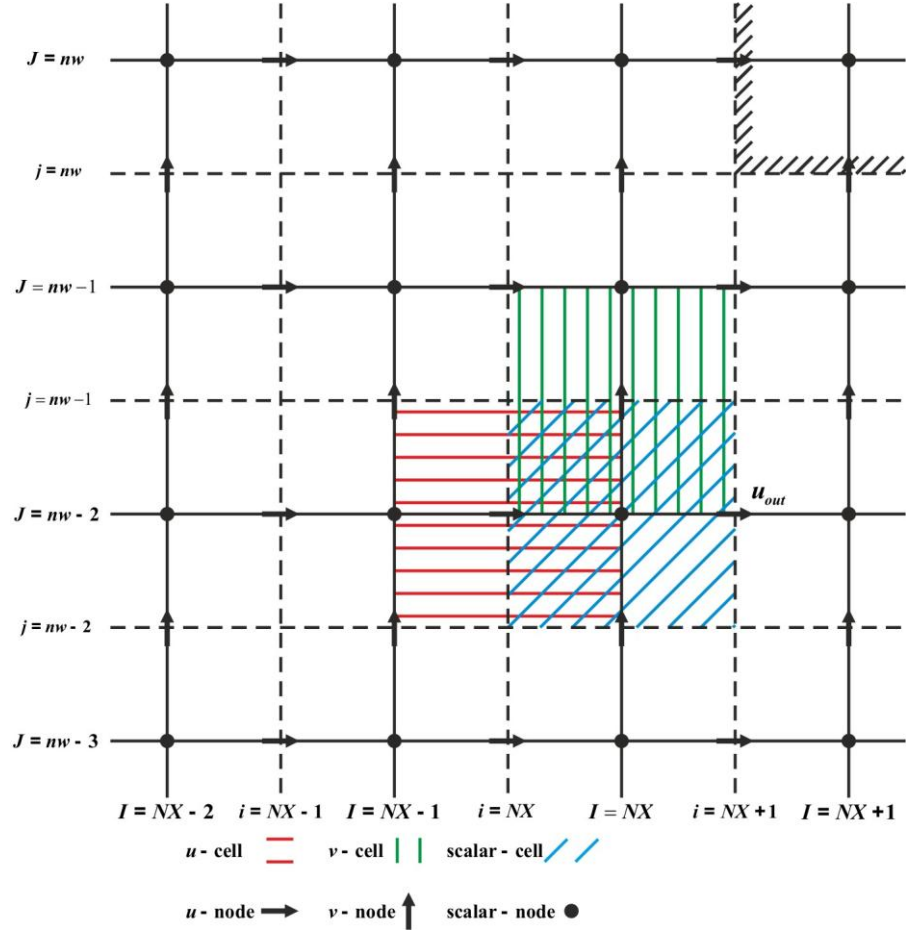


Fig. 4.6 Exit Boundary Discretization

Since the velocity B.C. at the inlet is set as a velocity-inlet, velocity B.C. at the exit can either be a velocity-outlet or a pressure-outlet. In both of these exit B.C. conditions, the exit flow is assumed to reach a fully developed state and hence the gradients of flow variables (except pressure and normal velocity) are zero normal to the exit plane meaning $v_{NX+1,j,k} = v_{NX,j,k}$, $w_{NX+1,j,k} = w_{NX,j,k}$, and $T_{NX+1,j,k} = T_{NX,j,k}$. The right hand sides of these equations are set from the previous time step values. Defining zero gradient to the normal velocity at the exit plane does not necessarily ensure mass conservation, so overall mass balance correction is applied if velocity-outlet (outflow) B.C. is used.

$$u_{NX+1,j,k} = u_{NX,j,k} \cdot \frac{\dot{m}_{in}}{\dot{m}_{out}} \quad (4.73)$$

In the above equation, \dot{m}_{in} and \dot{m}_{out} are the corresponding mass flow rates at the inlet and exit of the C.V. computed at every outer iteration, though calculation of the inlet mass flow rate at the inlet at every outer iteration is trivial for the problem at hand.

Also when velocity-outlet B.C. is used, for the p' -equation, a_E is set to zero and $u_E^* = u_E$ in equation (4.72).

If pressure-outlet B.C. is applied at the exit, the pressure correction at the scalar-cell in Fig. 4.6 is set to zero and the outlet normal velocity u_{out} is computed from interior values by writing mass conservation for the same scalar-cell.

$$u_{out} = u_{NX+1,j,k} = (u_{NX,j,k}\Delta y + v_{NX,j,k}\Delta x - v_{NX,j+1,k}\Delta x) / \Delta y \quad (4.74)$$

The bottom wall and the four side walls of the cavity except the inlet and exit are wall boundaries. Fig. 4.7 presents a wall boundary portion where x -direction is along the main flow direction, and y -direction is normal to the main flow. At the wall $v=0$, the y -momentum equations are solved from $j=2$ onwards. For the pressure correction equations at $J=1$, $a_s=0$ and $v_s^* = v_s$ in equation (4.72).

The bottom side of the u -cell is the wall and there is the shear interaction between the fluid and the wall since the fluid is viscous. The shear force in the x -direction, acting on the south face of the u -cell is, by assuming laminar flow and a fine enough mesh,

$$F_{xy} = -\tau_w A_{cell} = -\mu \frac{u_{i,2,K}}{\Delta y_p} A_{cell} \quad (4.75)$$

Hence $S_p = -\frac{\mu}{\Delta y_p} A_{cell}$ is a source term which should be included in the computation of $a_{i,J,K} \equiv a_p$ coefficient of equation (4.42) for the necessary nodes (Node $(i, J=1, K)$ in Fig. 4.7). Since $S_p \leq 0$ and $S_U = 0$ always positive coefficients rule (see Section 4.9) is ensured automatically for wall B.C. treatment of momentum equations.

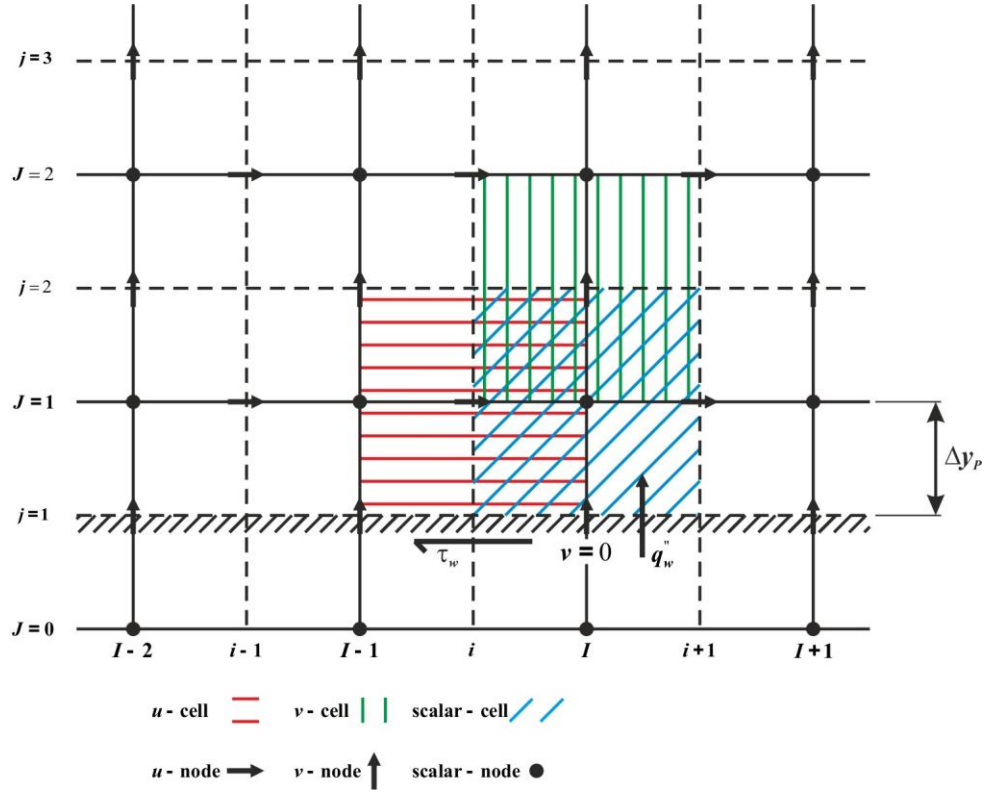


Fig. 4.7 Wall Boundary Discretization

Similar treatment could be applied for the z -direction velocity component (equation (4.44)) for the same wall boundary. The southern coefficients (a_s) are also set to zero for these x - and z -momentum equations.

For the energy equation, first of all, the southern coefficient a_s is set to zero. If the boundary condition is specified as constant temperature, the heat flow through the southern face of the scalar node ($I, J = 1, K$) is

$$q_s = k \frac{(T_{wall} - T_{I,1,K})}{\Delta y_p} A_{cell} \quad (4.76)$$

This heat transfer contributes to the discretized energy equation as a source term (equation (4.26) and (4.34)). The form of the source is

$$S = S_U + S_P T_{I,1,K} = \frac{k (T_{wall} - T_{I,1,K}) A_{cell}}{c_p \Delta y_p \Delta V} \quad (4.77)$$

Hence if wall temperature is higher than the grid point temperature of the fluid, fluid gains energy (positive source), and if wall temperature is lower than the grid point temperature of the fluid, fluid loses energy (negative source).

In either case $S_p = -\frac{k}{\Delta y_p} A_{cell}$ and it should be included in the computation of $a_{I,J,K}$

coefficient of equation (4.45) of the nodes $(I, J=1, K)$. Also $S_u = \frac{k}{\Delta y_p} T_{wall} A_{cell}$ and this

should be included in the computation of $b_{I,J,K}$ coefficient of the same equation of the same nodes. Just like the source terms of the momentum equation of a u -cell, the source terms of the energy equation of a scalar cell in the vicinity of a wall satisfies $S_p \leq 0$ and $S_u > 0$ regardless of the direction of the heat flow.

If the thermal boundary condition on the wall is isoflux, energy balance on the bottom surface of the C.V. yields

$$q_s = q''_{wall} A_{cell} \quad (4.78)$$

when the fluid gains energy from the wall. The source terms are $S_p = 0$ and $S_u = q''_{wall} A_{cell}$ and both of them satisfy the always positive coefficients rule. On the contrary, if the fluid would lose energy to the wall, energy balance on the interface surface would be

$$q_s = -q''_{wall} A_{cell} \quad (4.79)$$

yielding $S_p = 0$ and $S_u = -q''_{wall} A_{cell}$ contradicting the always positive coefficients rule. Once again special treatment required for the source terms of the discretized energy equation of the C.V. in the vicinity of a wall.

If the surface were to be insulated, both $S_p = S_u = 0$. Hence the always positive coefficients rule is always satisfied for the discretization of the energy equation of a fluid C.V. in the vicinity of an adiabatic wall.

Top surface of the cavity is a free-surface exposed to atmosphere. In Fig. 4.8, the grid arrangement near a free-surface is shown. Although there is mass transfer through the interface due to evaporation, this mass transfer will be neglected in the solution of momentum equations near the boundary, hence $v=0$ at $j=NY+1$. The y -momentum equations are solved up to $j=NY$. For the pressure correction equations at $J=NY$, $a_N = 0$ and $v_N^* = v_N$ in equation (4.72).

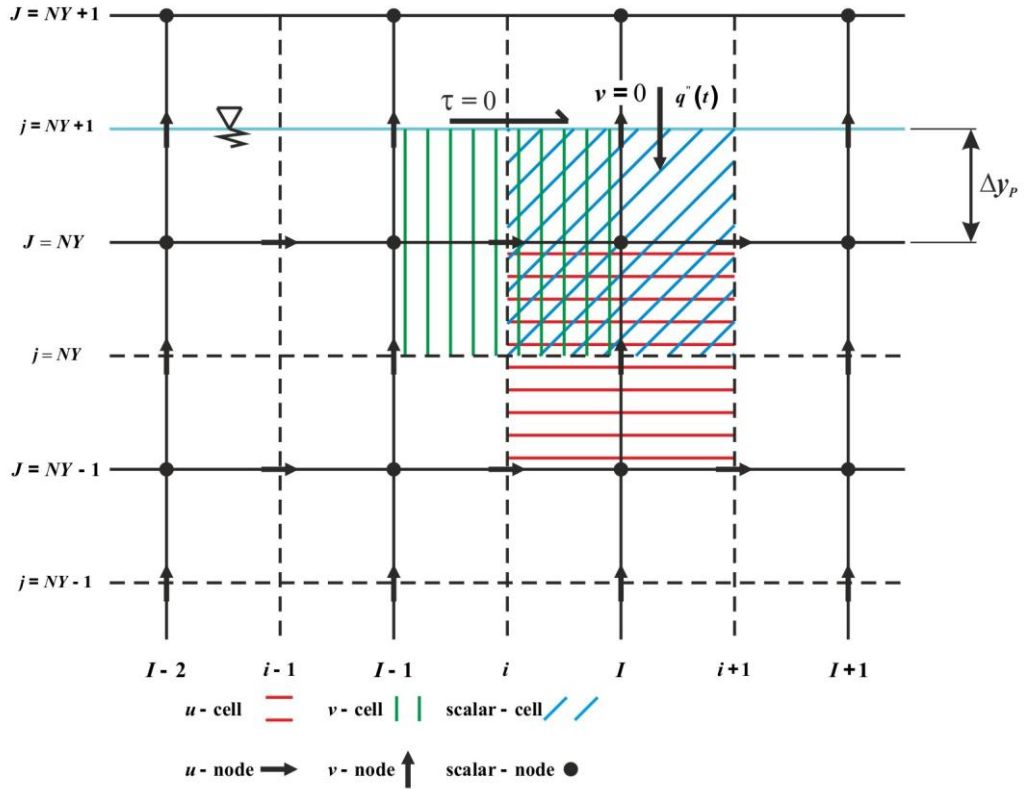


Fig. 4.8 Free-Surface Boundary Discretization

Air imposes almost no friction over water flowing under the free-surface interface hence no-shear (or slip) B.C. condition is modeled on the top surface of a u -cell in the vicinity of the air-water interface. Since no-shear is assumed, $F_{xy} = 0$ and there is no need for source term manipulations for the x - and z -momentum equations. The northern coefficients (a_N) are also set to zero for the x - and z -momentum equations.

In the discretization of the energy equation of a grid near the free surface, the top surface of the cell coincides with the interface and the heat transfers through the surface should be incorporated into the source terms of the discretized energy equation. There are three different heat transfer mechanisms occurring through the air-water interface. Convective heat transfer due to temperature difference between water and air, evaporative heat transfer due to concentration difference across the interface and solar irradiation over the interface. The first two heat transfers are always transient unless a steady temperature field within the cavity is attained. Solar irradiation can be selected constant or time varying.

$$q_S(t) = q_{conv}(t) + q_{evap}(t) - q_{solar}(t) \quad (4.80)$$

If we emphasize on the convective component only and assume that the surface temperature of the grid is equal to its nodal value $T_{I,NY,K}$

$$q_{conv} = h_{conv} A_{cell} (T_{\infty} - T_{I,NY,K}) \quad (4.81)$$

Giving $S_p = -\frac{h_{conv} A_{cell}}{c_p \Delta V} < 0$ and $S_u = \frac{h_{conv} A_{cell} T_{\infty}}{c_p \Delta V}$. Hence, the always positive coefficients rule can be satisfied regardless of the direction of heat flow. For the treatment of the heat transfer source due to evaporation, see Section 4.9.

The northern coefficient a_N of the discretized energy equation is also set to zero.

4.6 Solution of Discretized Equations

The general discretized equation (4.26) has to be solved five times during each iteration of the SIMPLE algorithm (momentum equations (4.53-4.55), pressure correction equation (4.64) and the energy equation). Any solution method of linear systems of equations, e.g. matrix inversion, Gauss elimination, Gauss-Seidel iteration could be used but since the system of equations of equation (4.26) is hepta-diagonal, hence, the coefficient matrix is full of nulls (a sparse matrix), a simple algorithm for a tri-diagonal matrix system with Gaussian elimination is frequently preferred. The algorithm is called Tri-Diagonal Matrix Algorithm (TDMA) or Thomas algorithm (after Thomas [26]).

A tri-diagonal system with N unknowns could be written as

$$a_{W_i} \phi_{i-1} + a_{P_i} \phi_i + a_{E_i} \phi_{i+1} = b_i \quad (4.82)$$

where $a_{W_1} = 0$ and $a_{E_N} = 0$. Gaussian elimination demands $O(N^3)$ operations whereas TDMA requires $O(N)$ operations only. Two sweeps of the domain is necessary to solve (4.82). In the forward sweep, the coefficients are modified

$$A_i = \begin{cases} \frac{a_{E_i}}{a_{P_i}} & i = 1 \\ \frac{a_{E_i}}{a_{P_i} - A_{i-1} a_{W_i}} & i = 2, 3, \dots, N \end{cases} \quad (4.83)$$

$$B_i = \begin{cases} \frac{b_i}{a_{P_i}} & i = 1 \\ \frac{b_i - B_{i-1} a_{W_i}}{a_{P_i} - A_{i-1} a_{W_i}} & i = 2, 3, \dots, N \end{cases} \quad (4.84)$$

The solution is achieved by the backward substitution sweep

$$\phi_i = \begin{cases} B_N & i = N \\ B_i - A_i \phi_{i+1} & i = N-1, N-2, \dots, 1 \end{cases} \quad (4.85)$$

The TDMA can be applied to equation (4.26) in a line-by-line fashion. If equation (4.26) is written as follows (the selection of western and eastern neighbors is arbitrary)

$$-a_W \phi_W + a_P \phi_P - a_E \phi_E = a_N \phi_N + a_S \phi_S + a_T \phi_T + a_B \phi_B + b \quad (4.86)$$

It is identical to the tri-diagonal system of equation (4.82) if the right hand side of equation (4.86) is assumed to be temporarily known from their previous values. Equation (4.86) is then changed in order to regard another pair (say the northern and southern neighbors) to be the unknowns of the TDMA. It is recommended to alter the TDMA sweep sequence during the solution; hence, the effect of the boundary conditions could be felt rapidly within the solution domain.

Although TDMA is recommended by many references, it is seen in the computations that Gauss-Seidel iteration is not inferior to TDMA when both algorithms are used for 2D domains. It's an iterative algorithm which uses initial values from the previous step and these initial values are updated as the domain is being swept.

$$\phi_P = (a_W \phi_W + a_E \phi_E + a_S \phi_S + a_N \phi_N + a_B \phi_B + a_T \phi_T + b) / a_P \quad (4.87)$$

For both of the algorithms it should be noted that the domain should be swept many times more for the pressure correction equations, actually only 1 sweep of the domain seems sufficient for the momentum equations and energy equation whereas less than 50 sweeps for the pressure correction equations are found to be insufficient.

4.7 Monitoring Convergence

Convergence of the solution within a time step should be monitored in order to be able to advance in time. This can be achieved by checking how well the discretization equation (4.26) is satisfied [23]. The difference of the LHS and the RHS of equation (4.26) is called the residual of the discretization equation.

$$R = a_E \phi_E + a_W \phi_W + a_N \phi_N + a_S \phi_S + a_T \phi_T + a_B \phi_B + b - a_P \phi_P \quad (4.88)$$

Obviously the residual should vanish when the solution converges. The absolute value of this residual could be used as a convergence criterion. However, commercial CFD codes (e.g. ANSYS FLUENT [27]) use scaled residuals over the whole solution domain.

$$R_\phi = \frac{\sum_{\text{all grids}} |a_E \phi_E + a_W \phi_W + a_N \phi_N + a_S \phi_S + a_T \phi_T + a_B \phi_B + b - a_P \phi_P|}{\sum_{\text{all grids}} |a_P \phi_P|} \quad (4.89)$$

ANSYS FLUENT's default criterion of convergence is the decreasing of scaled residuals below 10^{-3} for momentum equations and below 10^{-6} for the energy equation [27].

For the continuity equation, residual for a grid point is

$$R = \rho \Delta y (u_e - u_w) + \rho \Delta x (v_s - v_n) \quad (4.90)$$

The scaled residual over the whole domain is;

$$R_\phi = \frac{\sum_{\text{all grids}} |\rho \Delta y (u_e - u_w) + \rho \Delta x (v_s - v_n)|}{R_{\text{scaling}}} \quad (4.91)$$

R_{scaling} can be selected as the maximum cumulative absolute residuals over the whole domain in the first five iterations of the first time step of the computation. Default criterion of convergence is the decreasing of scaled residuals below 10^{-3} for the continuity equation.

4.8 Under-Relaxation

Under-relaxation, restraining the speed of solution by balancing the newly achieved solution with the previous solution is a must for the SIMPLE algorithm. If under-relaxation is not performed, the algorithm is susceptible to divergence [21, 23]. At the end of each iteration, pressure and velocity are under-relaxed as

$$p = p^* + \alpha_p p' \quad (4.92)$$

$$u^{new} = \alpha_u u + (1 - \alpha_u) u^{old} \quad (4.93)$$

$$v^{new} = \alpha_v v + (1 - \alpha_v) v^{old} \quad (4.94)$$

$$w^{new} = \alpha_w w + (1 - \alpha_w) w^{old} \quad (4.95)$$

The under-relaxation factors α_p , α_u , α_v , and α_w are all between zero and unity. Pressure-correction equation needed the highest under-relaxation with a value of 0.3, whereas momentum equations needed under-relaxations of 0.7 during the simulations.

Under-relaxation can also be applied to the energy equation yet it is not as crucial as the other flow equations. Only slight under-relaxation $\alpha_T = 0.9$ could be used if it is needed though no under-relaxation of the energy equation is necessary in our computations.

$$T^{new} = \alpha_T T + (1 - \alpha_T) T^{old} \quad (4.96)$$

4.9. Linearization of the Source Term and Always Positive Coefficients Rule

Although it was mentioned in the temporal discretization of the general transport equation that fully implicit scheme is unconditionally stable, it is actually not correct. Transient SIMPLE algorithm is susceptible to divergence [21, 23]. To ensure stable solution during time marching, always positive coefficients rule for the final discretized equation of the control volume integrated general transport equation should be employed. Combining equations (4.26) and (4.34)

$$a_p \phi_p = a_E \phi_E + a_W \phi_W + a_N \phi_N + a_S \phi_S + a_T \phi_T + a_B \phi_B + \rho \phi_p^0 \frac{\Delta V}{\Delta t} + \bar{S} \Delta V \quad (4.97)$$

In the above equation, all of the coefficients should be positive (actually non-negative) to ensure stable solutions. The coefficients $a_E, a_W, a_N, a_S, a_T, a_B,$ and a_p are always positive irrespective of the selected discretization scheme for the convective terms. The source term \bar{S} can be a zeroth, first, or higher order polynomial of the transport variable ϕ_p . In any case, the source term can be linearized in the form of

$$\bar{S} = S_U + S_p \phi_p \quad (4.98)$$

The second coefficient on the right hand side of the above equation, S_p is subtracted from the coefficient of ϕ_p in equation (4.97). Hence the coefficient of ϕ_p becomes $a_p - S_p$. Thus, in order to assure positive coefficients for the general discretized equation, S_U should be non-negative and S_p should be non-positive.

$$S_U \geq 0 \text{ and } S_p \leq 0 \quad (4.99)$$

To exemplify source term linearization, the near boundary cells affected by the Dirichlet or von Neumann boundary conditions could be examined. In Fig. 4.9, a typical near boundary temperature cell is represented. The heat flux shown in the figure could also be in the opposite direction (heat loss from the cell). The heat flux could originate from a specified temperature, heat flux, or convective heat flux.

When the specified heat flux is into the temperature cell, the source is positive

$$\bar{S} = S_U + S_P T_P = \frac{1}{\Delta V} \frac{q'' \Delta y}{c_p} > 0 \quad (4.100)$$

Since q'' is positive (into the cell). Hence the non-trivial selection of $S_U = \frac{1}{\Delta V} \frac{q'' \Delta y}{c_p}$ and $S_P = 0$ would satisfy the criterion in equation (4.99).

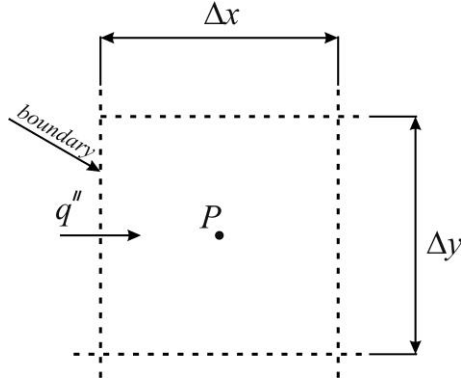


Fig. 4.9 A Typical Near Boundary Temperature Cell

If the specified heat flux on the boundary is from the cell to the boundary, then the source is negative.

$$\bar{S} = S_U + S_P T_P = -\frac{1}{\Delta V} \frac{q'' \Delta y}{c_p} < 0 \quad (4.101)$$

Equation (4.99) cannot be satisfied automatically. Source term linearization should be tried. Equation (4.101) can be rewritten as

$$\bar{S} = S_U + S_P T_P = -\frac{1}{\Delta V} \frac{q'' \Delta y}{c_p} = \frac{1}{\Delta V} \frac{q'' \Delta y}{c_p} - 2 \frac{1}{\Delta V} \frac{q'' \Delta y}{c_p} \frac{T_P}{T_P} \quad (4.102)$$

If instead of using the variable T_P in the denominator on the last term of the above equation, the previously known temperature value T_P^* from the previous time step is used, the above equation will be achieved approximately and equation (4.99) is satisfied.

$$S_U = \frac{1}{\Delta V} \frac{q'' \Delta y}{c_p} > 0 \text{ and } S_P = -2 \frac{1}{\Delta V} \frac{q'' \Delta y}{c_p} \frac{1}{T_P^*} < 0$$

When the boundary of Fig. 4.9 is an isothermal wall boundary, the source term will be:

$$\bar{S} = S_U + S_P T_P = \frac{1}{\Delta V} \frac{k(T_{wall} - T_P) \Delta y}{\frac{\Delta x}{2} c_P} \quad (4.103)$$

$$S_U = \frac{1}{\Delta V} \frac{k T_{wall} \Delta y}{\frac{\Delta x}{2} c_P} > 0 \text{ and } S_P = -\frac{1}{\Delta V} \frac{k \Delta y}{\frac{\Delta x}{2} c_P} < 0$$

Regardless of the direction of the heat transfer. So equation (4.99) would be satisfied.

When the boundary of Fig. 4.9 is a convective heat transfer boundary, the source term will be:

$$\bar{S} = S_U + S_P T_P = \frac{1}{\Delta V} \frac{h(T_\infty - T_P) \Delta y}{c_P} \quad (4.104)$$

$$S_U = \frac{1}{\Delta V} \frac{h T_\infty \Delta y}{c_P} > 0 \text{ and } S_P = -\frac{1}{\Delta V} \frac{h \Delta y}{c_P} < 0$$

Satisfying equation (4.99) regardless of the heat transfer direction.

When at the boundary there is also evaporative heat transfer, the contribution of the evaporative heat transfer to the source term of the discretized energy equation would be

$$\bar{S} = S_U + S_P T_P = \frac{1}{\Delta V} \frac{h_m (\phi \rho_w (@T_\infty) - \rho_w (@T_P)) h_{fg} (@T_P) \Delta y}{c_P} \quad (4.105)$$

Since the evaporative heat transfer from the water body to air, $\bar{S} < 0$, the simple selection of

$$S_U = \frac{1}{\Delta V} \frac{h_m (\phi \rho_w (@T_\infty) - \rho_w (@T_P)) h_{fg} (@T_P) \Delta y}{c_P} < 0 \text{ and } S_P = 0$$

would contradict equation (4.99). Actually evaporative and convective heat transfers occur simultaneously through a free-surface and if the magnitude of $S_U = \frac{1}{\Delta V} \frac{h_m \Delta y}{c_P}$

from the convective heat transfer is higher than the magnitude of $S_U = \frac{1}{\Delta V} \frac{h_m (\phi \rho_w (@T_\infty) - \rho_w (@T_P)) h_{fg} (@T_P) \Delta y}{c_P}$ from the evaporative heat transfer,

addition of the two components may or may not give $S_U \geq 0$. So, to be on the safe side, source term linearization should be applied to equation (4.105). The following form

$$\begin{aligned} \bar{S} = S_U + S_P T_P = & \frac{1}{\Delta V} \frac{h_m(\rho_w(@T_P) - \phi \rho_w(@T_\infty)) h_{fg}(@T_P) \Delta y}{c_p} \\ & - 2 \frac{1}{\Delta V} \frac{h_m(\rho_w(@T_P) - \phi \rho_w(@T_\infty)) h_{fg}(@T_P) \Delta y}{c_p} \frac{T_P}{T_P^*} \end{aligned} \quad (4.106)$$

is sufficient in order to yield

$$S_U = \frac{1}{\Delta V} \frac{h_m(\rho_w(@T_P) - \phi \rho_w(@T_\infty)) h_{fg}(@T_P) \Delta y}{c_p} > 0$$

and

$$S_P = -2 \frac{1}{\Delta V} \frac{h_m(\rho_w(@T_P) - \phi \rho_w(@T_\infty)) h_{fg}(@T_P) \Delta y}{c_p} \frac{1}{T_P^*} < 0$$

CHAPTER 5

THE COMPUTER CODE

The computer code is written in standard C++ programming language. Any standard C++ compiler (e.g. Visual C++, GNU's GCC) would compile the code. The IDE used is a freeware IDE named Dev-C++ 4.9.9.2 [28]. The IDE is bundled with the freeware GNU compiler collection GCC. The version of the compiler set is 4.5.0. It is only necessary to open the "main.cpp" file of the code inside the IDE and compile and run. For other IDE's and other operating system environments (Dev-C++ is a Windows based IDE), a makefile may be necessary to prepare in order to compile and run the code.

The flow chart of the program is presented in Fig. 5.1. The flow chart is in essence parallel to the transient SIMPLE algorithm (Fig. 4.4) and is represented one to one in the main function of the code. Prior to the main function, the constants of the flow, the variables and the functions are declared with a header file "cavity_2D.h". The constants of the flow, geometry parameters, parameters of algorithms used are all read into the program from an input file named "input.cpp". Hence once the code is compiled successfully and an executable file is gained, only the parameters inside the input file is altered to have different simulations.

Three sets of variables for (u, v, P , and T) are needed to be stored in memory for a transient SIMPLE code, one set is the working variable set, the values of which change within a time step at every iteration (or inner loop in Fig. 5.1). One set stores the values of the previous iterative step and is renewed with the values of the working variable set at the end of each iteration of a time step. Last set stores the values of the previous time step and is renewed at the end of each time step (outer loop). These three sets of variables (along with other variables such as coefficients naturally) are initiated by the setIC (set initial condition) function. At this level the real time is at zero. The function setBCs (set boundary conditions) sets the boundary conditions of the flow.

The algorithm is started with the outer loop (time marching) and the time is incremented by the time step. At this step an auxiliary function named startAnOuterIteration is called in order to do the processing of some data necessary to be done before inner iterations of the time step is started. These processing of data is the computation of convective and evaporative heat transfer coefficients from the free-surface temperature data, temporal

determination of the heat flux lost from the cavity to its two vertical side walls, computation of the various heat loss items and thermal energy storage rate of the cavity.

The inner loop starts. The inner loop is intended to achieve an acceptable solution (bounded by the residual limits) of a specific time step. The `set_u_Coefficients` function, as the name implies, sets the coefficients of the discretized x -momentum equation (4.46). Then the discretized x -momentum equation is solved using the Tri-Diagonal Matrix Algorithm or Gauss-Seidel Iteration. Hence with these two functions, the discretized x -momentum equation is solved using the guessed pressure and velocity fields and an intermediate u velocity field. This u velocity field along with the guessed v velocity field and guessed pressure field are used in the calculation of the y -momentum equation. After a guess for the velocity field is gotten, the outlet boundary condition should be updated with `updateOutletBC` function (see Section 4.5) which extrapolates the outlet BC variables from the interior solution.

Next the coefficients of the pressure-correction equation are determined, and pressure correction field is solved. With this pressure-correction field, the pressure field and velocity field are corrected by `correct_and_underrelax_P_u_v_w` function in accordance with equations (4.49) and (4.59) to (4.61). This function also performs under-relaxation to pressure and velocity fields. The under-relaxation factors used in the code are the default values of ANSYS FLUENT for a wide-variety of problems.

The coefficients of the energy equation are computed with the corrected pressure and velocity values with `set_T_Coefficients`, and the energy equation is solved with TDMA or Gauss-Seidel Iteration.

The `computeResiduals` function computes the residuals according to equations (4.89) and (4.91). If all of the residual values are less than the desired limiting values (also taken from ANSYS FLUENT) the inner loop is terminated, outer loop operates, time is forwarded one step. If the residuals are not small enough, inner loop turns once again.

Finally, the function `checkSteadiness` will check whether steady conditions are reached within the medium. In the experiments, steadiness criterion was almost no change in temperature field in 15 minutes. In the program, the energy conservation equation in the rate form for the cavity can be traced (equation 7.28). When the time rate derivative term vanishes, it can be concluded that steady-state condition within the cavity is achieved. Actually, in the runs the program is let go to run further beyond steady-state in order to be conservative.

Even the 2D simulations last for hours of computation time. To avoid loss of data if a power loss occurs, at every 10 minutes of simulation time, flow variables are stored to backup files. The simulation can be restarted from a backup file if the program is informed the simulation time and the backup file of that simulation time.

Also at every 10 minutes of the simulation time, output files appropriate for post-processing within MATLAB and Tecplot software packages are written onto the hard-drive. MATLAB is easier to use and more flexible to automate post-processing while Tecplot outputs better looking graphs.

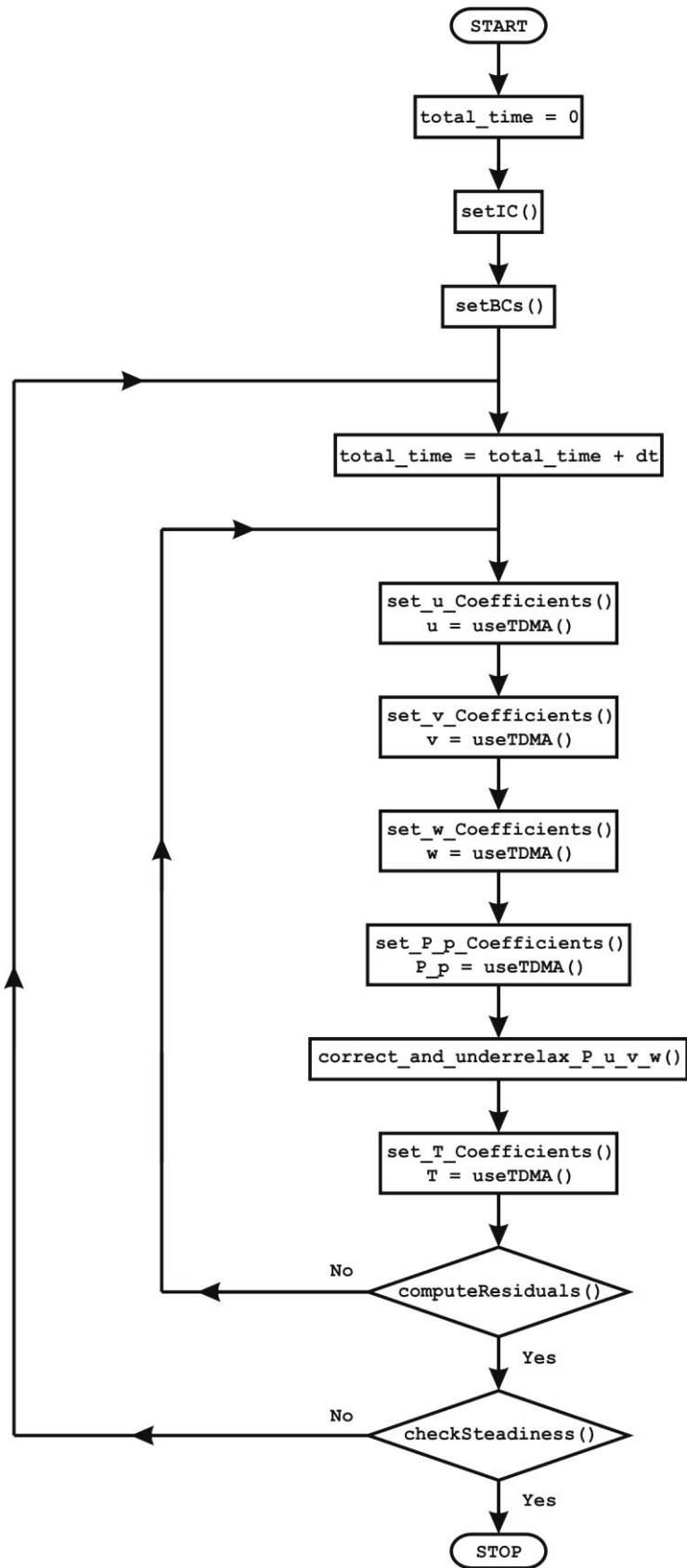


Fig. 5.1 Flow Chart of the Program

CHAPTER 6

VALIDATION OF THE CODE

6.1 2D Laminar Steady Flow within a Lid-Driven Cavity

The validation of the 2D code is started with the simplest benchmark problem for 2D flows, the famous lid-driven cavity problem. The boundaries of the square cavity are walls. The top wall moves to the right horizontally while the three other walls are stationary. The velocity of the wall and the kinematic viscosity of the hypothetical fluid inside the cavity are selected such that the flow inside the cavity is laminar. The governing equations are as follows;

$$\frac{\partial u}{\partial x} + \frac{\partial v}{\partial y} = 0 \quad (6.1)$$

$$\rho u \frac{\partial u}{\partial x} + \rho v \frac{\partial u}{\partial y} = -\frac{\partial p}{\partial x} + \mu \left(\frac{\partial^2 u}{\partial x^2} + \frac{\partial^2 u}{\partial y^2} \right) \quad (6.2)$$

$$\rho u \frac{\partial v}{\partial x} + \rho v \frac{\partial v}{\partial y} = -\frac{\partial p}{\partial y} + \mu \left(\frac{\partial^2 v}{\partial x^2} + \frac{\partial^2 v}{\partial y^2} \right) \quad (6.3)$$

The comparison of the results with the results from literature is satisfactory (see Fig. 6.1). The next step is to increase the complexity of the cavity by adding an inlet and an outlet to the cavity hence introducing two types of momentum equation boundaries to the code. The flow inside the cavity is 2D laminar steady flow without energy equation and the model is next section's model without energy equation. The result is the same as next section's $Ri=0$ case with only the momentum equations and continuity equation are solved.

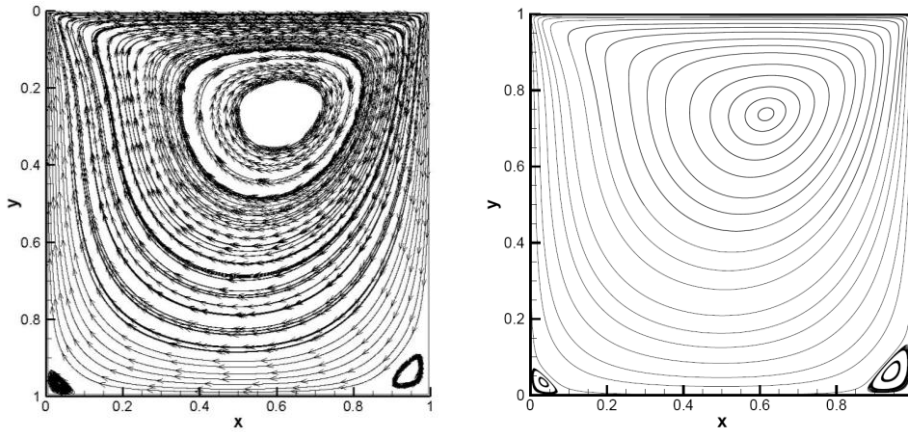


Fig. 6.1 Comparison of Streamlines for Lid-Driven Cavity, $Re = 100$,
On the Left, Output of the Code, On the Right, from [29]

6.2 2D Laminar Steady Flow with Energy Equation within a Cavity with 1 Inlet and 1 Outlet

Next, laminar steady flow and energy equation within a 2D cavity with 1 inlet and 1 exit is modeled. Model is based on the study of Saha et. al. [30] from the literature in order to make comparison easily. The geometry of the flow is shown in Fig. 6.2.

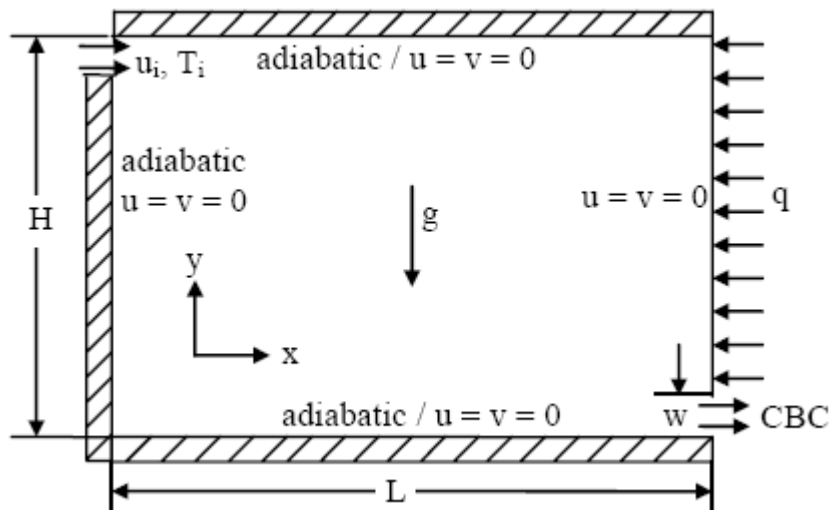


Fig. 6.2 Schematic Configuration of the Cavity, from [30]

Cooler fluid ($T_i = 1$) is fed from the inlet at the upper left corner (which has a height of $h = 0.1H$), entrains the cavity which has no-slip wall boundaries and adiabatic thermal boundaries except the right vertical wall which is heated with a constant heat flux $q = 1$ and leaves the cavity from the outlet at the lower right corner which has the same height as the inlet.

The governing equations are;

$$\frac{\partial u}{\partial x} + \frac{\partial v}{\partial y} = 0 \quad (6.4)$$

$$\rho u \frac{\partial u}{\partial x} + \rho v \frac{\partial u}{\partial y} = -\frac{\partial p}{\partial x} + \mu \left(\frac{\partial^2 u}{\partial x^2} + \frac{\partial^2 u}{\partial y^2} \right) \quad (6.5)$$

$$\rho u \frac{\partial v}{\partial x} + \rho v \frac{\partial v}{\partial y} = -\frac{\partial p}{\partial y} + \mu \left(\frac{\partial^2 v}{\partial x^2} + \frac{\partial^2 v}{\partial y^2} \right) - \rho g \beta (T - T_i) \quad (6.6)$$

$$\rho c u \frac{\partial T}{\partial x} + \rho c v \frac{\partial T}{\partial y} = k \left(\frac{\partial^2 T}{\partial x^2} + \frac{\partial^2 T}{\partial y^2} \right) \quad (6.7)$$

The non-dimensional forms are as follows;

$$\frac{\partial U}{\partial X} + \frac{\partial V}{\partial Y} = 0 \quad (6.8)$$

$$U \frac{\partial U}{\partial X} + V \frac{\partial U}{\partial Y} = -\frac{\partial P}{\partial X} + \frac{1}{Re} \left(\frac{\partial^2 U}{\partial X^2} + \frac{\partial^2 U}{\partial Y^2} \right) \quad (6.9)$$

$$U \frac{\partial V}{\partial X} + V \frac{\partial V}{\partial Y} = -\frac{\partial P}{\partial Y} + \frac{1}{Re} \left(\frac{\partial^2 V}{\partial X^2} + \frac{\partial^2 V}{\partial Y^2} \right) - \frac{Gr}{Re^2} \theta \quad (6.10)$$

$$U \frac{\partial \theta}{\partial X} + V \frac{\partial \theta}{\partial Y} = \frac{1}{Re Pr} \left(\frac{\partial^2 \theta}{\partial X^2} + \frac{\partial^2 \theta}{\partial Y^2} \right) \quad (6.11)$$

Where, $Gr = \frac{g \beta q H^4}{k \nu^2}$, $Re = \frac{u_i H}{\nu}$, $Pr = \frac{\nu}{\alpha}$, $Ri = \frac{Gr}{Re^2}$

In the study of Saha et. al. [30], Reynolds number and Prandtl numbers are kept constant at values $Re = 100$ and $Pr = 0.71$ whereas Richardson number is varied. Our code is

tuned to reveal these dimensionless parameters by utilizing a hypothetical fluid with desired thermophysical properties. The flow variables and cavity geometry are also input as the dimensionless values from the paper. For example inputting $u_i = 1$, $H = 1$, and hypothetical $\nu = 0.01$ and $\alpha = 1/71$ yields $Re = 100$ and $Pr = 0.71$.

Variation of Richardson number is achieved by changing the gravitational acceleration while keeping β , q , k values unity. For example zero gravity gives $Gr = 0$ and $Ri = 0$ while $g = 5$ gives $Gr = 50000$ and $Ri = 5$.

The streamlines and isotherms for different Richardson numbers from [30] is presented in Fig. 6.3. Saha et. al. used their code which was written with FEM. Our FVM code's corresponding streamlines and isotherms (generated from the output files of the code with Tecplot) are presented in Fig. 6.4 thru Fig. 6.7.

The matching of the streamlines and isotherms from Saha et. al. [30] and our code seems quite satisfactory.

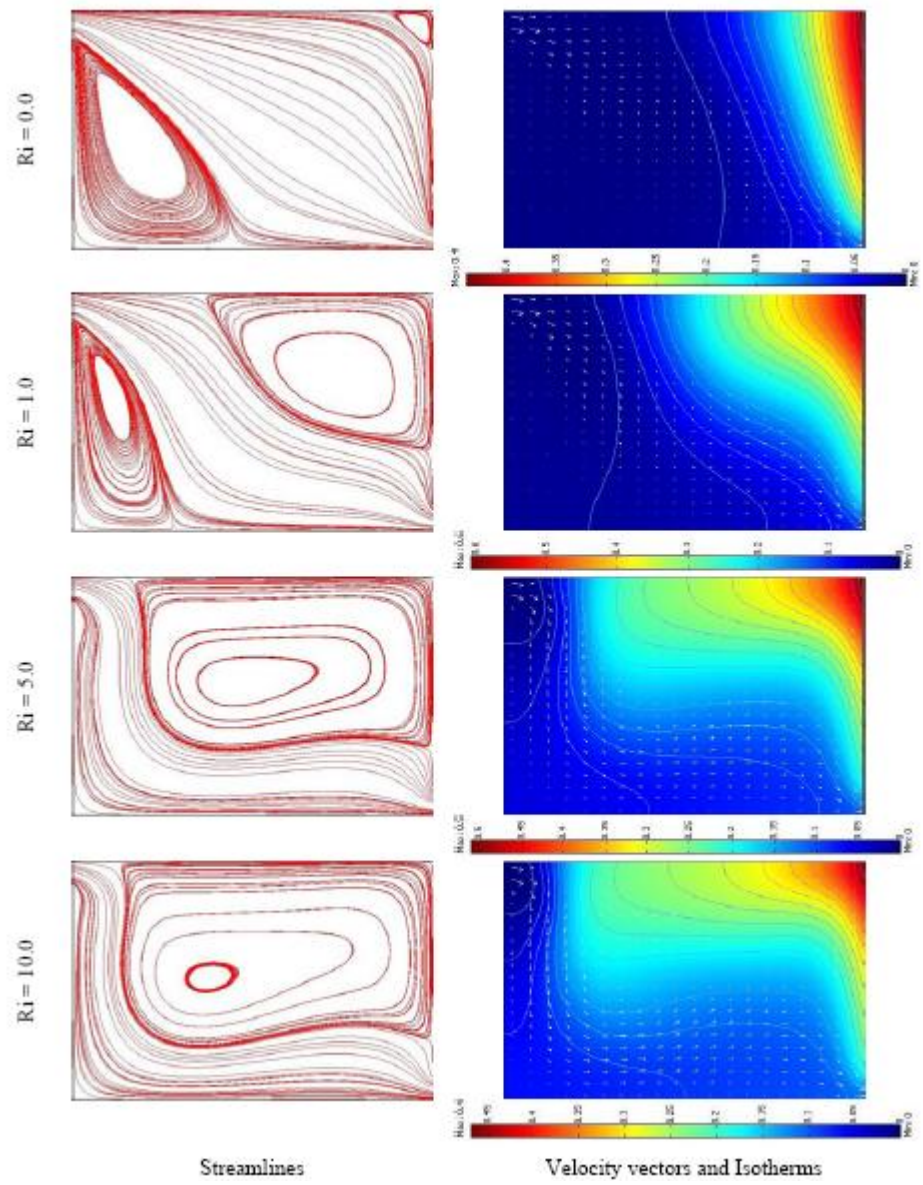


Fig. 6.3 Variation of Streamlines and Isotherm Contours for Different Ri values, from [30]

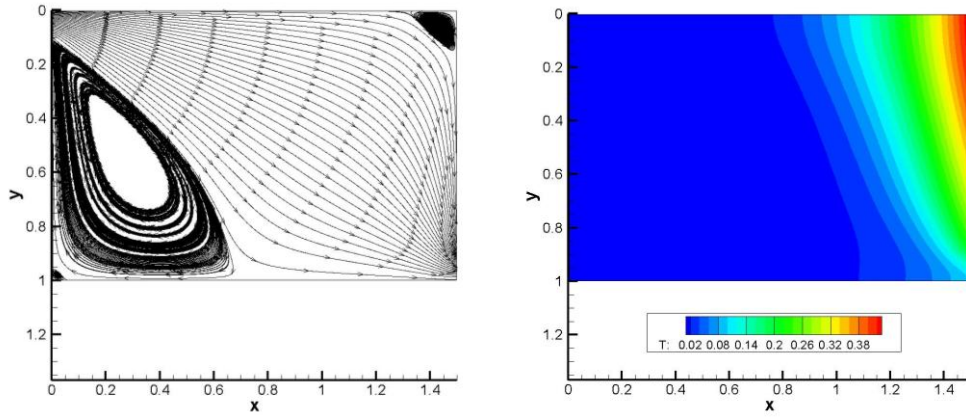


Fig. 6.4 Streamlines and Isotherms for $Ri = 0$ ($Re = 100$, $Pr = 0.71$)

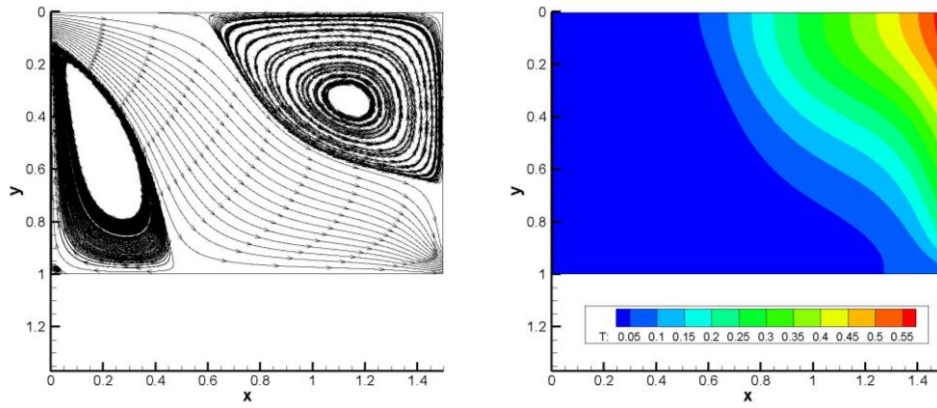


Fig. 6.5 Streamlines and Isotherms for $Ri = 1$ ($Re = 100$, $Pr = 0.71$)

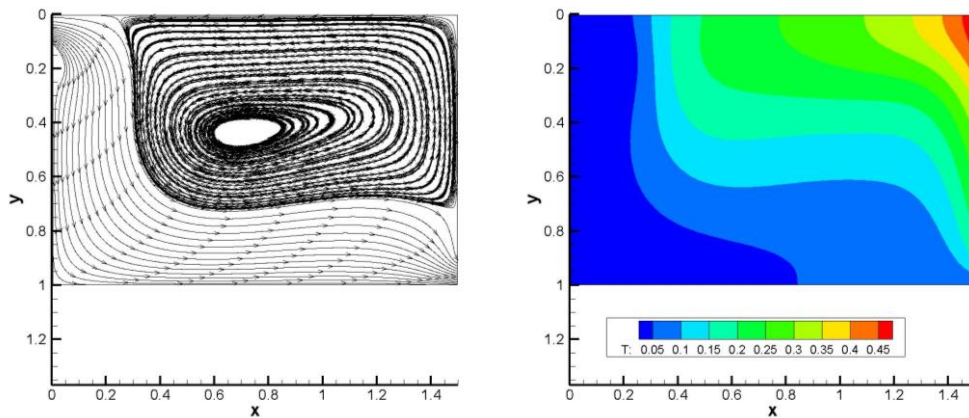


Fig. 6.6 Streamlines and Isotherms for $Ri = 5$ ($Re = 100$, $Pr = 0.71$)

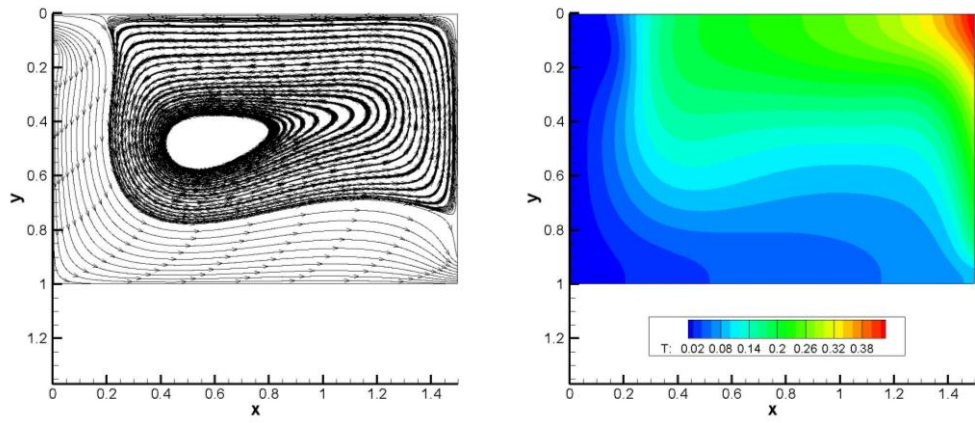


Fig. 6.7 Streamlines and Isotherms for $Ri = 10$ ($Re = 100$, $Pr = 0.71$)

CHAPTER 7

RESULTS AND DISCUSSIONS

7.1 The Geometry, Initial Condition, and Boundary Conditions

The geometry and the boundary conditions of the 2D cavity is shown in Fig. 7.1. Initially stagnant water at a uniform temperature fills the cavity up to a height of H . The cavity is flow-through having one inlet at the top of one side and one outlet at the bottom of the opposite side. Warmer water is fed to the cavity from the inlet and relatively cooler water is drained from the outlet. The I.C. and B.C.'s in mathematical formulation are as follows:

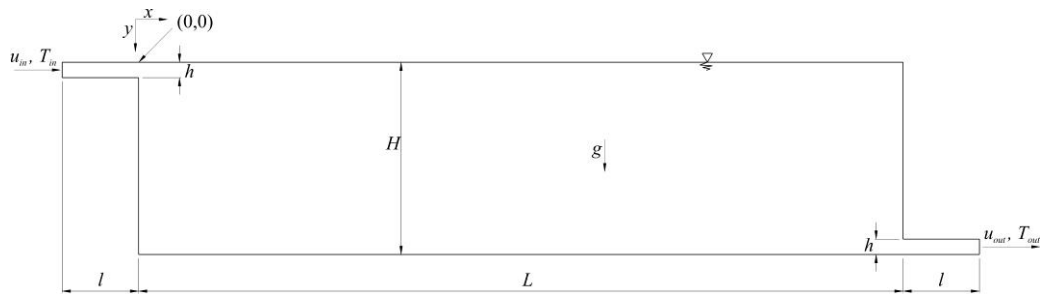


Fig. 7.1 2D Cavity Geometry

At $t = 0$;

$$u = v = 0 \quad \text{and} \quad T = T_{ic} \quad (7.1)$$

for the cavity, the inlet, and the outlet.

For $t > 0$;

The inlet BC's are;

$$u = u_{in} \quad \text{and} \quad T = T_{in} \quad (7.2)$$

for $x = -l, 0 \leq y \leq h$

The upper and lower walls of inlet have no-slip boundary and no heat transfer;

$$u = v = \frac{\partial T}{\partial y} = 0 \quad (7.3)$$

for $-l \leq x \leq 0, y = 0$ and $y = h$

The upper and lower walls of outlet also have no-slip and no heat transfer;

$$u = v = \frac{\partial T}{\partial y} = 0 \quad (7.4)$$

for $L \leq x \leq L+l, y = H-h$ and $y = H$

The outlet boundary conditions are;

$$u = U_{out}(y) \quad (7.5)$$

$$T = T_{out}(y) \quad (7.6)$$

for $x = L+l, H-h \leq y \leq H$

The variations of the velocity profile and the temperature profile at the outlet are computed iteratively from the interior solutions during the computations. The velocity profile can be computed by assuming the outlet either as a velocity outlet or a pressure outlet. The discretization of both of the outlet types are presented in Section 4.5. The crucial point at the solution of the outlet velocity profile is that the selected outlet type must satisfy mass conservation.

The bottom of the cavity has no-slip and is adiabatic;

$$u = v = \frac{\partial T}{\partial y} = 0 \quad (7.7)$$

for $0 \leq x \leq L, y = H$

Top surface is a free surface with no-shear velocity boundary and has a transient heat transfer through the surface. This transient surface has convective and evaporative losses, losses since in all of the simulations the temperature of the ambient air is cooler than surface temperature of water, and a solar gain, if applicable.

$$\frac{\partial u}{\partial y} = v = 0 \quad \text{and} \quad \frac{\partial T(x,0)}{\partial y} = \frac{q_s(t)}{k_w} \quad (7.8)$$

for $0 \leq x \leq L, \quad y=0$

The vertical walls of the cavity have no-slip boundary condition;

$$u = v = 0 \quad (7.9)$$

for $x=0, \quad h \leq y \leq H$ and $x=L, \quad 0 \leq y \leq H-h$

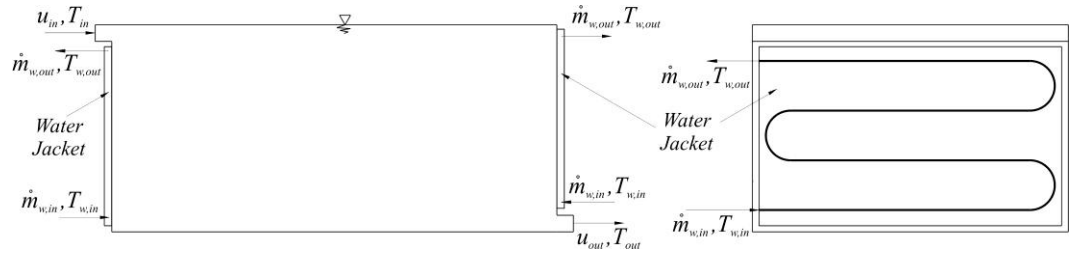


Fig. 7.2 Schematic Drawing of Experimental Set-up
Showing the Water Jackets, Front and Side Views

For the treatment of the thermal boundary condition of the vertical walls, the schematic drawing of the experimental set-up, presented in Fig. 7.2 should be considered. In the experiments, in order to attain a strong thermal stratification within the cavity, large amount of heat is transferred from the cavity by circulating high mass flow rates of relatively cool water through the side wall jackets. This, in fact, induces complex thermal boundary conditions on the vertical side walls, which cannot be merely represented by a simple isothermal or isoflux boundary condition. The situation is examined profoundly in the following section.

7.2 Examination of the Thermal Boundary Condition on the Vertical Side Walls

In this section, different thermal boundary conditions on the vertical side walls will be examined and the optimum amongst them will be selected in order to be able to use as the selected thermal B.C. on the vertical side walls in the subsequent sections. The selection criterion will be the comparison of the results with experimental data obtained by the author previously. In order to see solely the effect of different thermal B.C.'s on the vertical side walls, in the following simulations, all of the thermophysical properties of water, geometry parameters of the 2D cavity, and every other hydrodynamic and thermal

boundary conditions of the cavity will be kept constant. All of the simulations will be run for 600 minutes. The geometry and flow parameters of all simulations can be found in Table B.1.

The thermophysical properties of water used in the simulations are

$$\rho = 997 \frac{\text{kg}}{\text{m}^3}, \quad \mu = 855 \times 10^{-6} \frac{\text{kg}}{\text{ms}}, \quad k = 0.613 \frac{\text{W}}{\text{mK}},$$

$$c_p = 4179 \frac{\text{J}}{\text{kgK}}, \quad \beta = 276.1 \times 10^{-6} \frac{1}{\text{K}}$$

And the gravitational acceleration is $g = 9.81 \frac{\text{m}}{\text{s}^2}$.

The geometric parameters, initial condition and boundary conditions are selected similar to a set of experiments performed by the author [17] in his master thesis.

$$L = 2\text{m}, \quad l = 0.2\text{m}, \quad H = 0.5\text{m}, \quad h = 0.04\text{m}$$

$$T_{ic} = T_{amb} = 20^\circ\text{C}, \quad T_{in} = 50^\circ\text{C}, \quad u_{in} = 1.5 \times 10^{-3} \frac{\text{m}}{\text{s}} \quad \text{or} \quad \dot{m}_{in} = 215 \frac{\text{kg}}{\text{hr}}$$

In the first simulation, the vertical side walls will be regarded as isothermal walls;

$$T = T_{wl} = \text{const.} \tag{7.10}$$

for $x=0, \quad h \leq y \leq H$ and $x=L, \quad 0 \leq y \leq H-h$

The constant temperature value assigned to the vertical walls in Simulation 1 is $T_{wl} = 10^\circ\text{C}$. The development of the vertical temperature profile at the middle of the cavity, i.e. at $x = L/2 = 1\text{m}$, can be seen in Fig. 7.3. The profiles are plotted at 30 minute intervals. The slow penetration of the effect of relatively hot inlet water within the cavity can be seen clearly even in this first simulation. Although at intermittent profiles some strong levels of vertical thermal stratification can be seen, as time goes by and the cavity approaches a steady thermal field, at around $t = 450\text{min}$ or so, there is only weak vertical thermal stratification left in the cavity. Comparison of Fig. 7.3 and experimental data of Fig. 7.4 shows that isothermal vertical wall boundary condition (or at least the wall temperature of $T_{wl} = 10^\circ\text{C}$) is not sufficient to generate a strong thermal stratification in the cavity. Strong vertical thermal stratification in a body can be achieved by large heat losses in horizontal directions hence first thing to do to improve the situation is to lower the wall temperature so that more heat will be lost through the vertical side walls. In Simulation 2, wall temperature is decreased to 0°C and the resulting vertical temperature development is presented in Fig. 7.5.

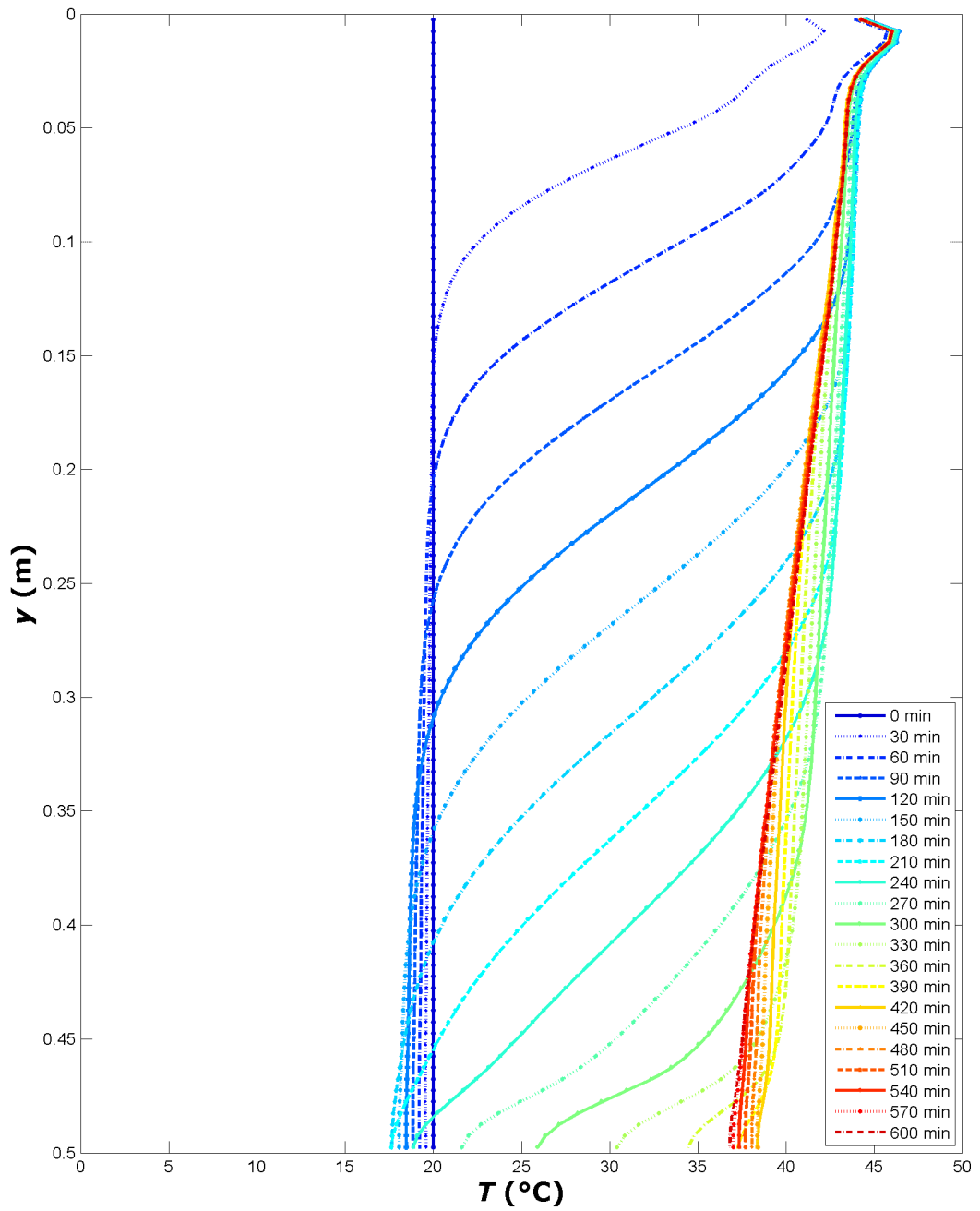


Fig. 7.3 Development of Vertical Temperature Profile within Cavity at $x = 1\text{ m}$ for Simulation 1

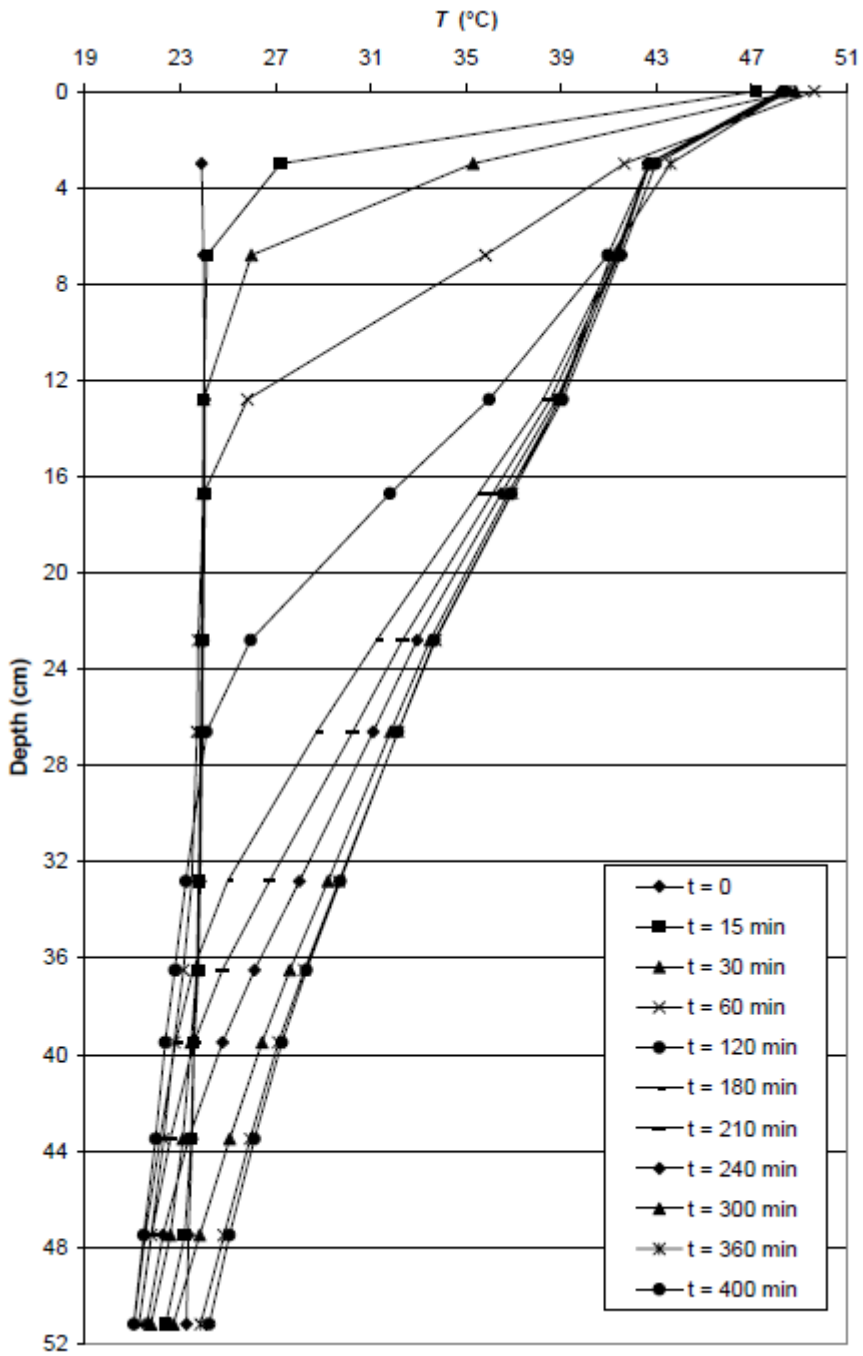


Fig. 7.4 Development of Vertical Temperature Profile within Cavity, from [17]

Comparison of Fig. 7.3 and 7.5 reveals that by decreasing the isothermal wall temperature 10°C , a slightly stronger thermal stratification could be achieved. The temperature values near the surface for the two simulations are quite comparable yet the bottom temperature of Simulation 2 is around 35°C whereas it is around 37°C for Simulation 1. The overall effect is yet insufficient when Simulation 2 is compared with the experimental data of Fig. 7.4. It can be concluded that isothermal wall BC for the vertical side walls is not sufficient to exert a heat transfer potent enough to induce a strong vertical thermal stratification in the cavity. Decreasing further the value of the isothermal wall temperature would be trivial since two-phase flow model is not used in the simulations.

One thing to mention for the temperature profiles of Fig. 7.3 and 7.5 is that near the free surface, the effect of convective heat transfer to the environment is obvious. This trend could not be captured during experimentation due to lack of enough thermocouples near the surface.

Another thermal boundary condition that could be applied upon the vertical walls would be linearly decreasing (with depth) wall temperature

$$T = T_{wl}(y) = T_{wl1} + \frac{T_{wl2} - T_{wl1}}{H} y \quad (7.11)$$

for $x=0, h \leq y \leq H$ and $x=L, 0 \leq y \leq H-h$

where $T_{wl1} = T_{wl}(0) > T_{wl2} = T_{wl}(H)$

A sample simulation for $T_{wl1} = 10^{\circ}\text{C} > T_{wl2} = 0^{\circ}\text{C}$ is run and the development of vertical temperature profile within the cavity is supplied in Fig. B.1 in Appendix.

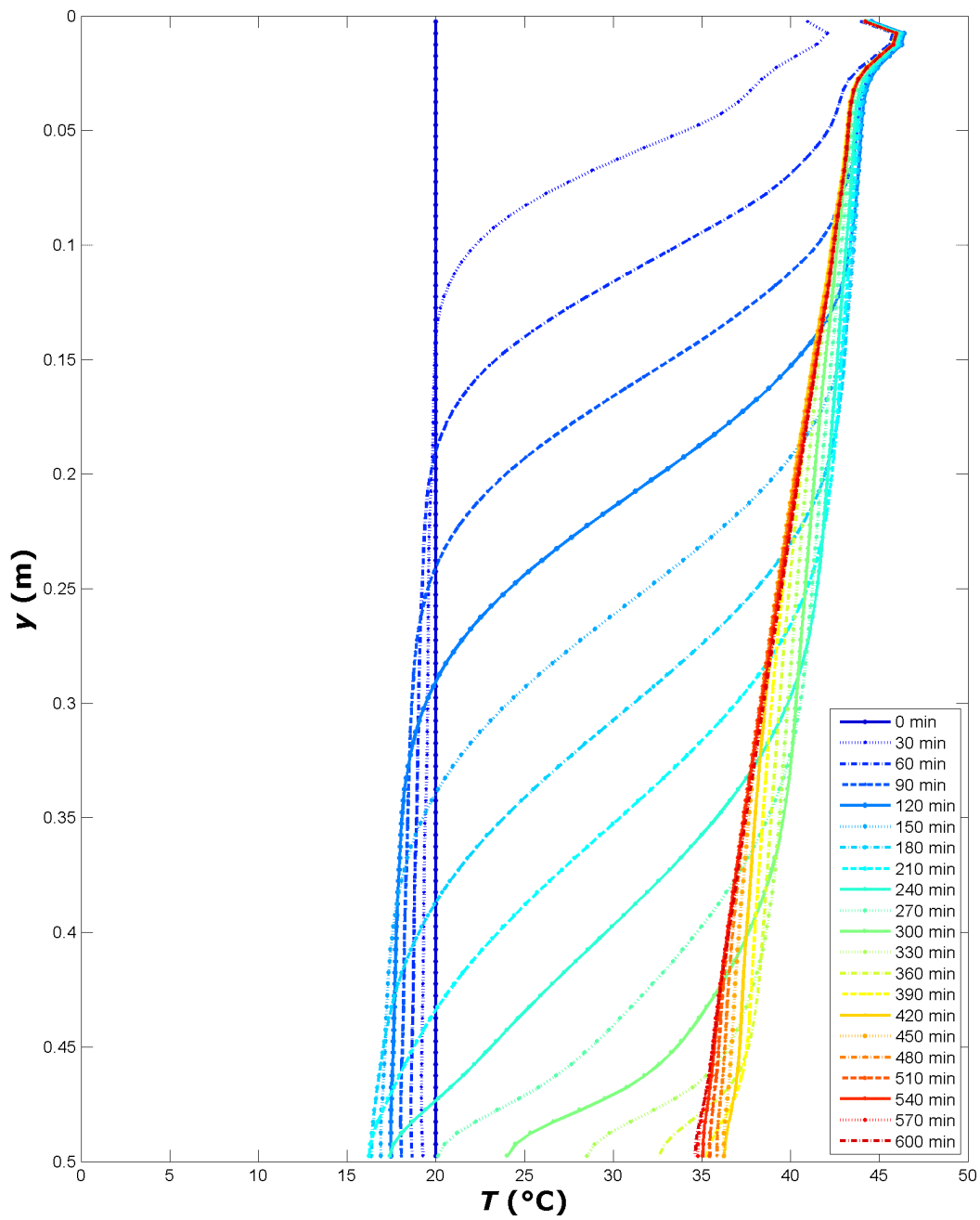


Fig. 7.5 Development of Vertical Temperature Profile within Cavity at $x = 1\text{ m}$ for Simulation 2

The next form of thermal boundary to be applied to the vertical walls is isoflux thermal boundary condition.

$$\frac{\partial T}{\partial x} = -\frac{1}{k_w} q''_{wl} \quad (7.12)$$

for $x=0, h \leq y \leq H$ and $x=L, 0 \leq y \leq H-h$

In Simulation 4 (see Fig. 7.6), a constant and steady value of $q''_{wl} = 4000 \text{ W/m}^2$ is applied to the vertical side walls. The numerical value for the heat flux is the maximum measured value in a similar experiment. The maximum value in an experiment during the charging period occurs when a steady temperature distribution within the cavity is attained, since by this time the cavity is at its maximum load and its losses are at their maxima.

First thing to notice in the figure that a stronger vertical thermal stratification at the end of the charging period could be achieved. The temperature near the surface, just like the previous simulations stays around 45°C but the bottom temperatures falls down to around 29°C . Although the level of stratification is still not enough, it is promising.

Another thing worth noting is that the cooling of the cavity during the charging period well behind the initial temperature of the cavity which is 20°C . This is a direct consequence of extracting $q''_{wl} = 4000 \text{ W/m}^2$ from the very start of the simulation when there should be almost no heat loss due to low thermal energy content of the cavity. In reality, when a cavity is charged by relatively warm inlet water and cooled from the side walls by circulating cooling water inside some heat exchangers attached onto the side walls, the heat transferred from the cavity should slowly develop as the thermal energy stored within the storage slowly increases. This issue will be addressed in the following simulations.

Before a transient wall heat flux is applied to the vertical side walls, the effect of a higher wall heat flux on the cavity is examined. A higher constant and steady heat flux of $q''_{wl} = 6000 \text{ W/m}^2$ is applied in Simulation 6 and the temperature profiles of Fig. 7.7 is obtained.

As the heat flux extracted from the side surfaces is increased one half, the resulting steady vertical temperature profile is quite stratified and in fact it is close to experimental results. But the cooling of the lower portions of the cavity below the initial temperature is also more pronounced.

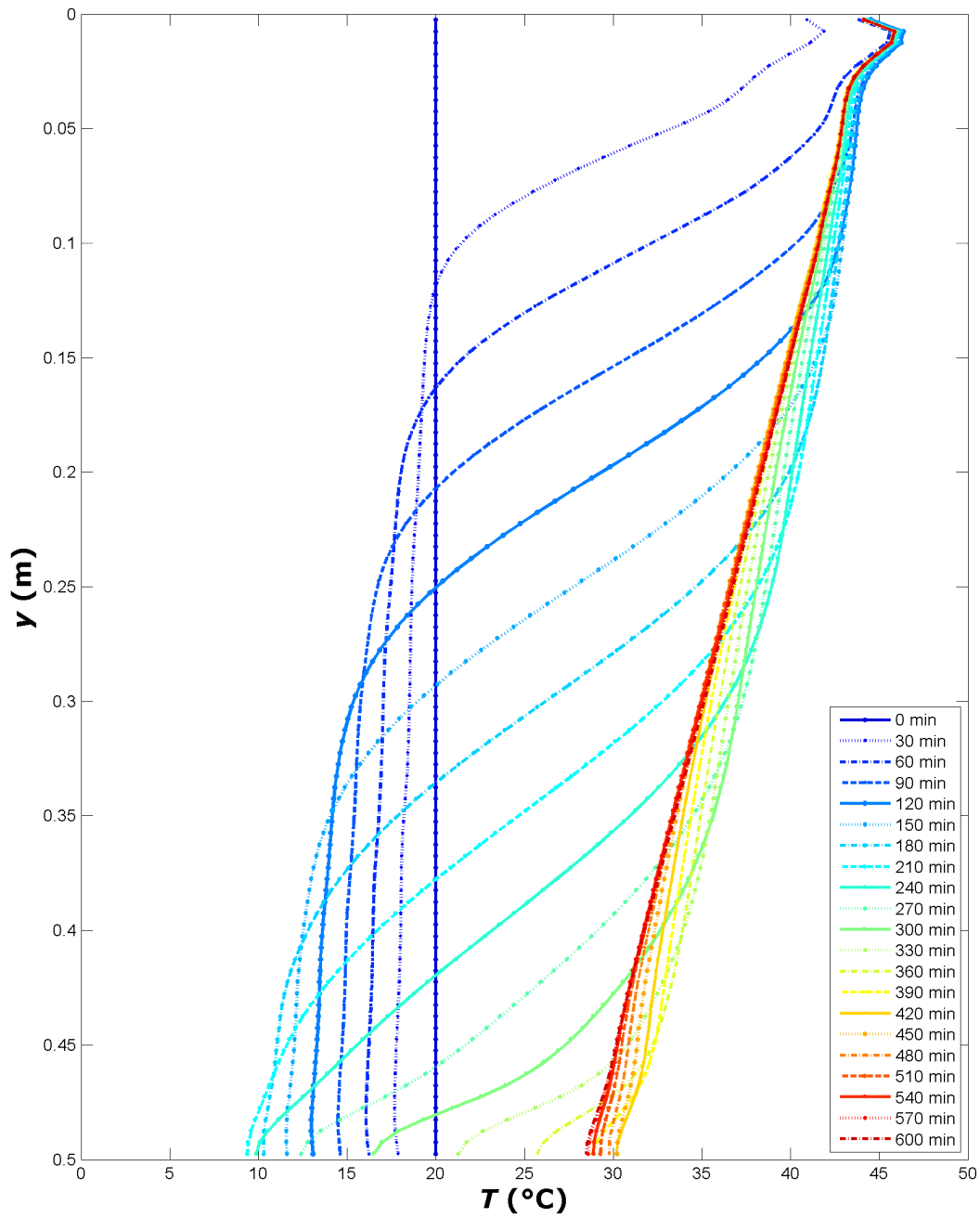


Fig. 7.6 Development of Vertical Temperature Profile within Cavity at $x = 1\text{ m}$ for Simulation 4

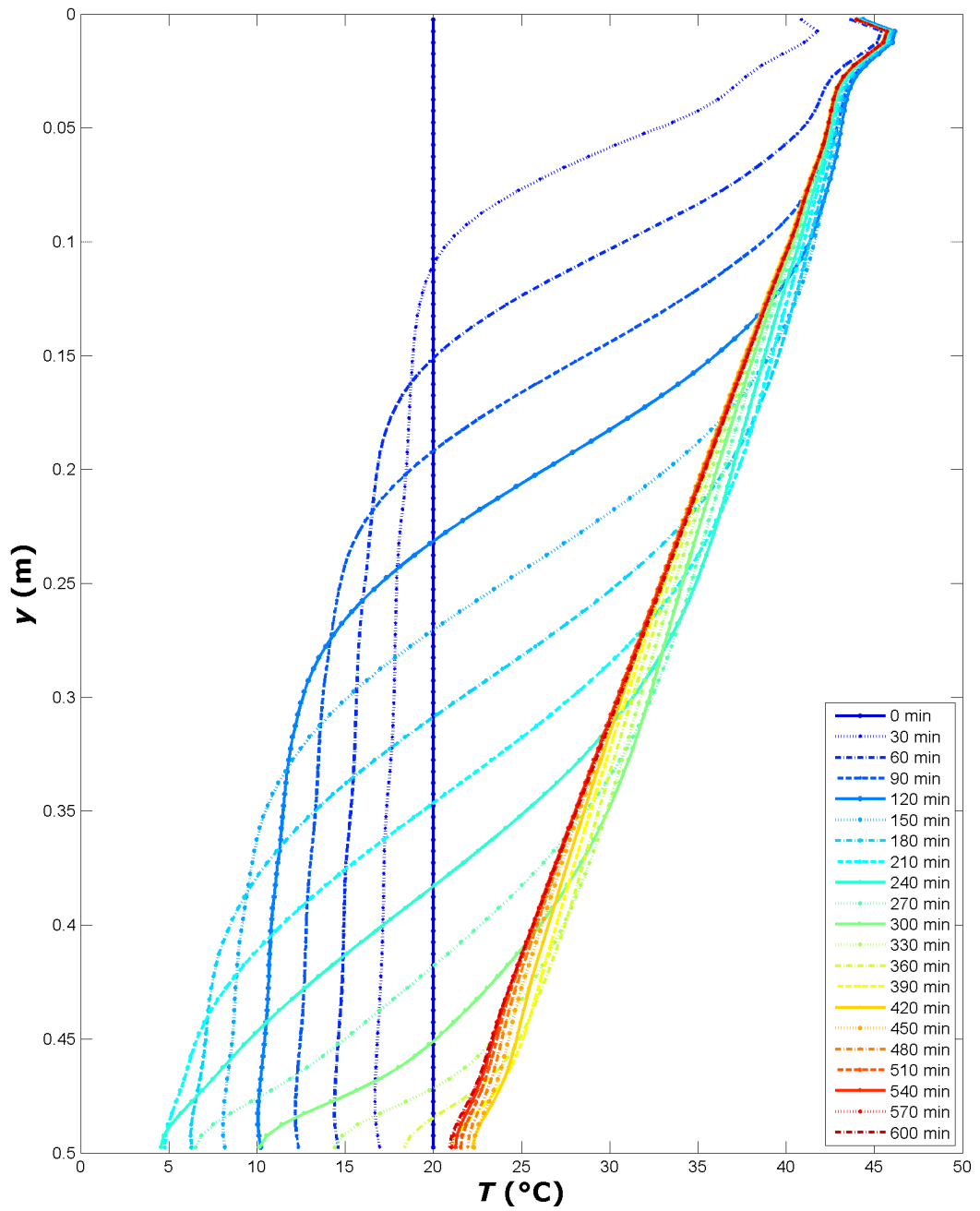


Fig. 7.7 Development of Vertical Temperature Profile within Cavity at $x = 1\text{ m}$ for Simulation 6

Altering the constant and steady heat flux boundary on the side walls to constant yet transient boundary seems more reasonable in order to better simulate the heat exchangers attached to the vertical side walls of the cavity. In order to do that, the transient change of the side wall heat flux will be approximated to experimental data. Wall heat flux variation with time in a typical experiment can be found in Table B.2 in Appendix. The data in the table is actually coarsened data from an experiment. The number of data points is lowered. The wall heat flux in the experiments would not change after about $t = 300$ min (before the cavity attains a steady thermal profile) so the same trend is also followed in the computations.

In the Simulation 8, this data from Table B.2 is used and the resulting vertical temperature profiles are presented in Fig. 7.8. By comparing Fig. 7.6 and 7.8, it is seen that by using a temporally changing but spatially non-changing wall heat flux improves somewhat the problem of the cooling of the water in the lower regions of the cavity way below the initial water temperature. Yet it is insufficient. On top of changing the wall heat flux temporally, the heat flux should be changed spatially too. Also, just like increasing the constant heat flux value of Simulation 6 (Fig. 7.6) gives a stronger steady thermal stratification than of Simulation 4 (Fig. 7.5), the values of Table B.2 can be accentuated to a desired maximum heat flux rate by simply multiplying the values of Table B.2 by the desired value and dividing all of the values by the maximum value at the table (which is 3900 W/m^2).

$$q''_{wl}(t) = \frac{q''_{wl_max}}{3900 \text{ W/m}^2} q''_{wl_TableB.1}(t) \quad (7.13)$$

As an example, if a temporal wall heat flux distribution with a maximum heat flux value of 6000 W/m^2 is desired, utilizing equation (7.13) will yield a heat flux which is presented in Fig. 7.9.a. The figure shows the wall heat flux applied to the vertical side walls at different times up to 300 min, at that time q''_{wl} reaches its maximum value of 6000 W/m^2 and stays at that value until the end of the charging process.

When a time-varying heat flux characterized by the values in Table B.2 or in Fig. 7.9.a is applied to the cavity, we simply extract equal amounts of thermal energy from the higher and lower regions of the cavity. Yet thermal stratification in vertical direction exists in the medium, water temperature is highest near the free surface and lowest near the bottom surface. Hence extracting equal amounts of thermal energy in the vertical direction is erroneous. In Fig. 7.9.b, c, and d, three different heat flux variations are presented that have not only temporal variations, but also spatial variations.

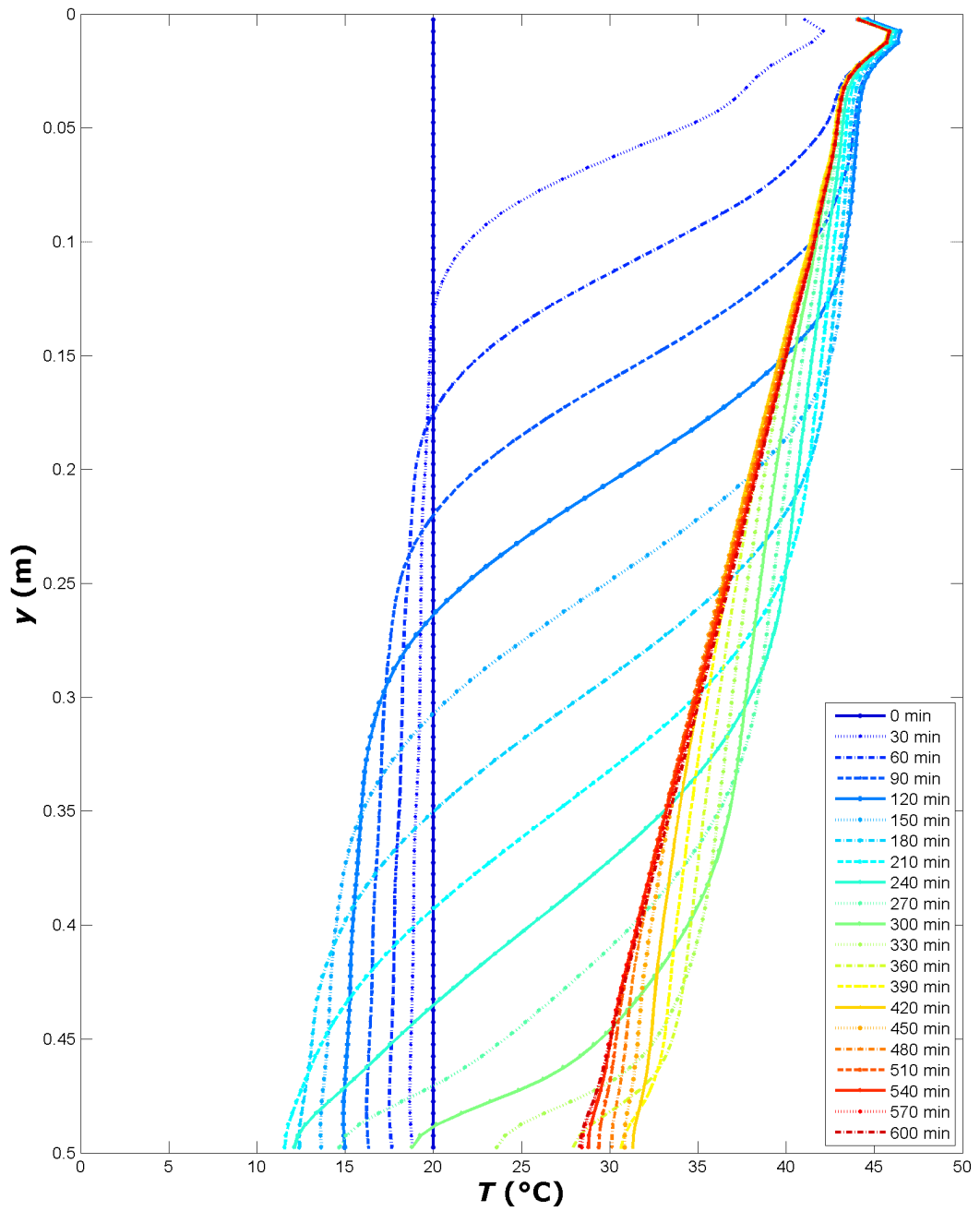
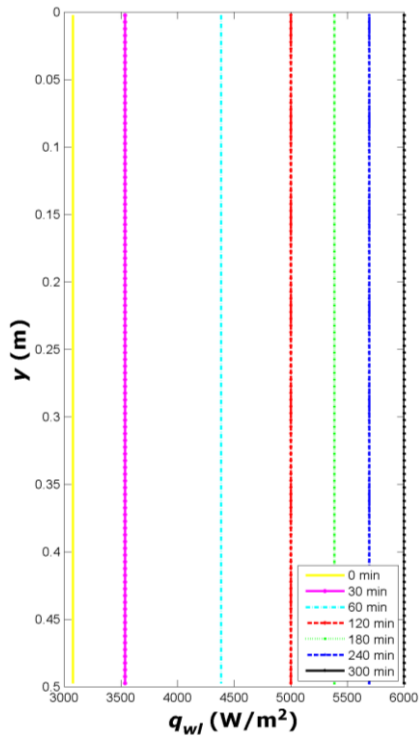
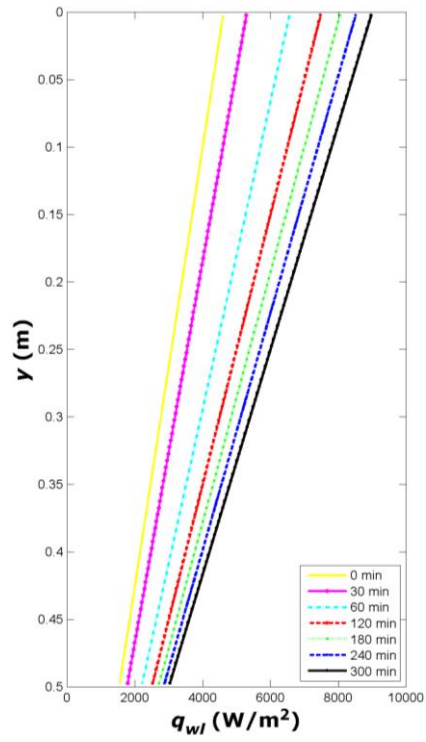


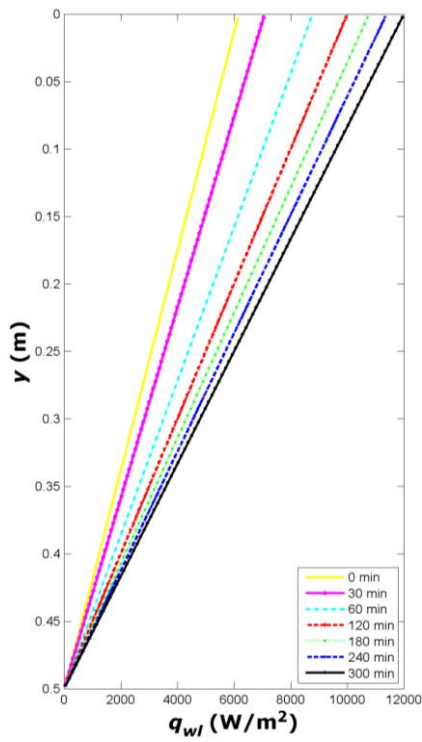
Fig. 7.8 Development of Vertical Temperature Profile within Cavity at $x = 1\text{ m}$ for Simulation 8



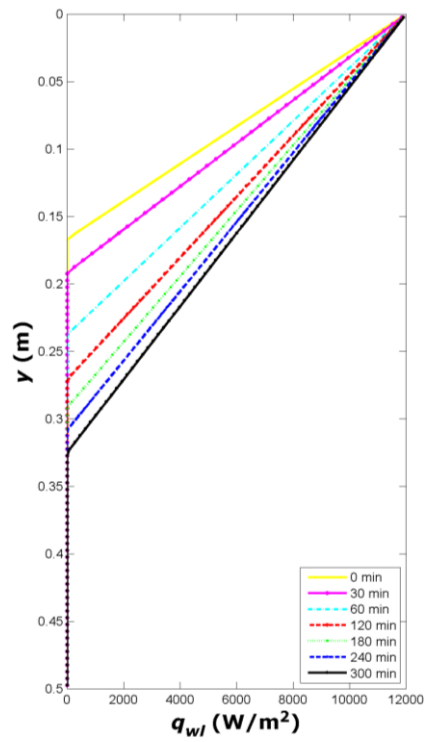
(a)



(b)



(c)



(d)

Fig. 7.9 Different Spatial & Temporal Heat Flux Patterns for Vertical Side Walls

All of the thermal boundary conditions in Fig. 7.9 have the same area under the $q''_{wl}(y,t)$ vs. y at any equal time. That is, the area under the perpendicular trapezoidal region at any time of Fig. 7.9.b is equal to the rectangular area of Fig 7.9.a at the same time, and the vertex of the triangle of Fig 7.9.c at the free-surface is twice the value of the value of the heat flux of Fig. 7.9.a at the same time. Also for the triangular variation of Fig. 7.9.d, the penetration depth is calculated such that the area of the triangles bounded by the penetration depth and twice the value of the heat flux of Fig. 7.9.a are once again equal to the areas of rectangles of Fig. 7.9.a.

Development of vertical temperature profile figures for the four side heat flux patterns shown in Fig. 7.9 are shown in Figures 7.10 to 7.13. By looking at the figures we may conclude that all of them shows final strongly stratified thermal profiles towards the end of simulations. The over-cooling of the lower regions of the cavity is least pronounced in Fig. 7.13. This simulation devices the B.C. depicted in Fig. 7.9.d. A slowly penetrating in depth heat flux boundary on the vertical side surfaces.

Thus from now on, in the simulations the selected vertical side wall thermal B.C. will be the one depicted in Fig. 7.9.d.

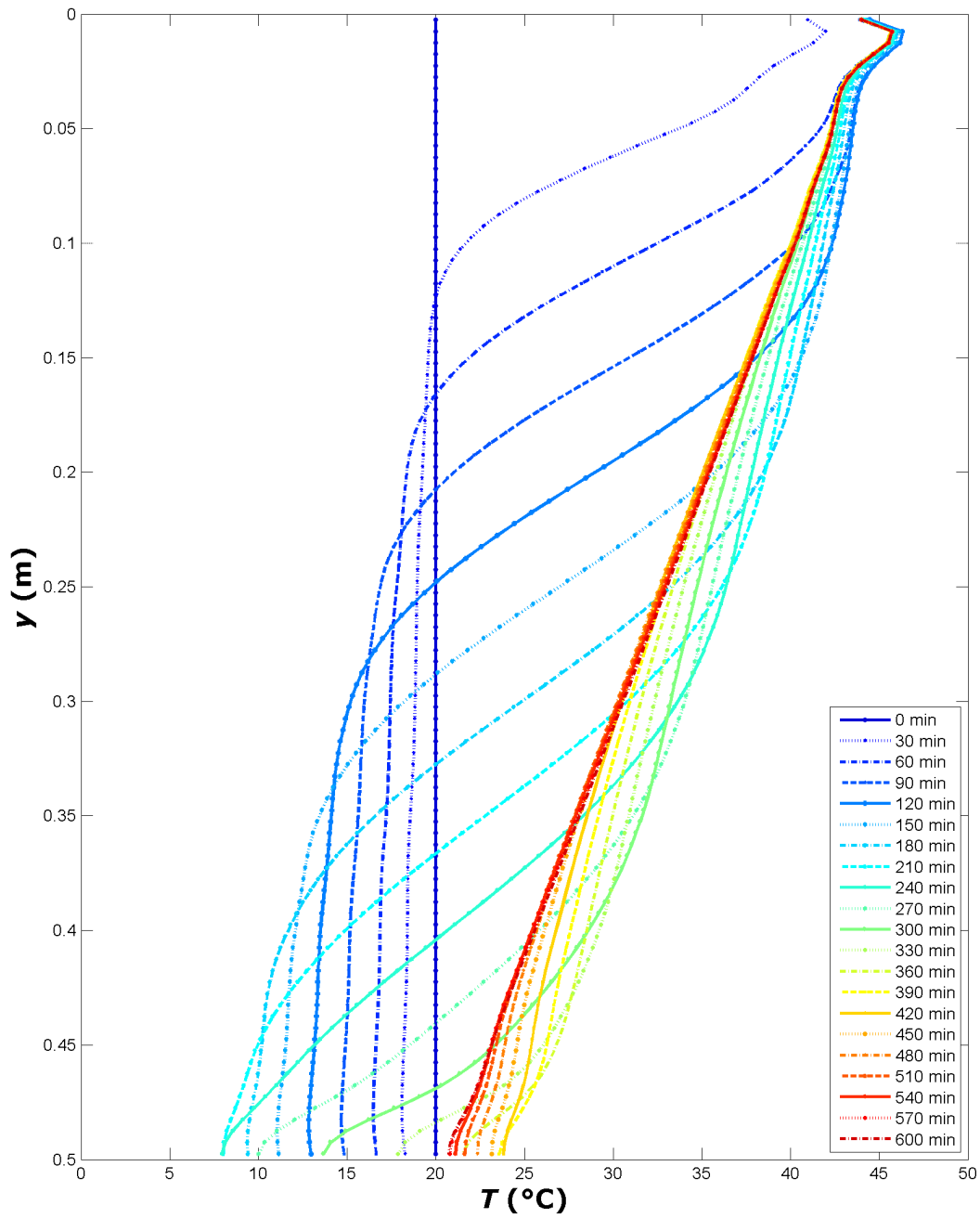


Fig. 7.10 Development of Vertical Temperature Profile within Cavity at $x = 1\text{m}$ for Simulation 10

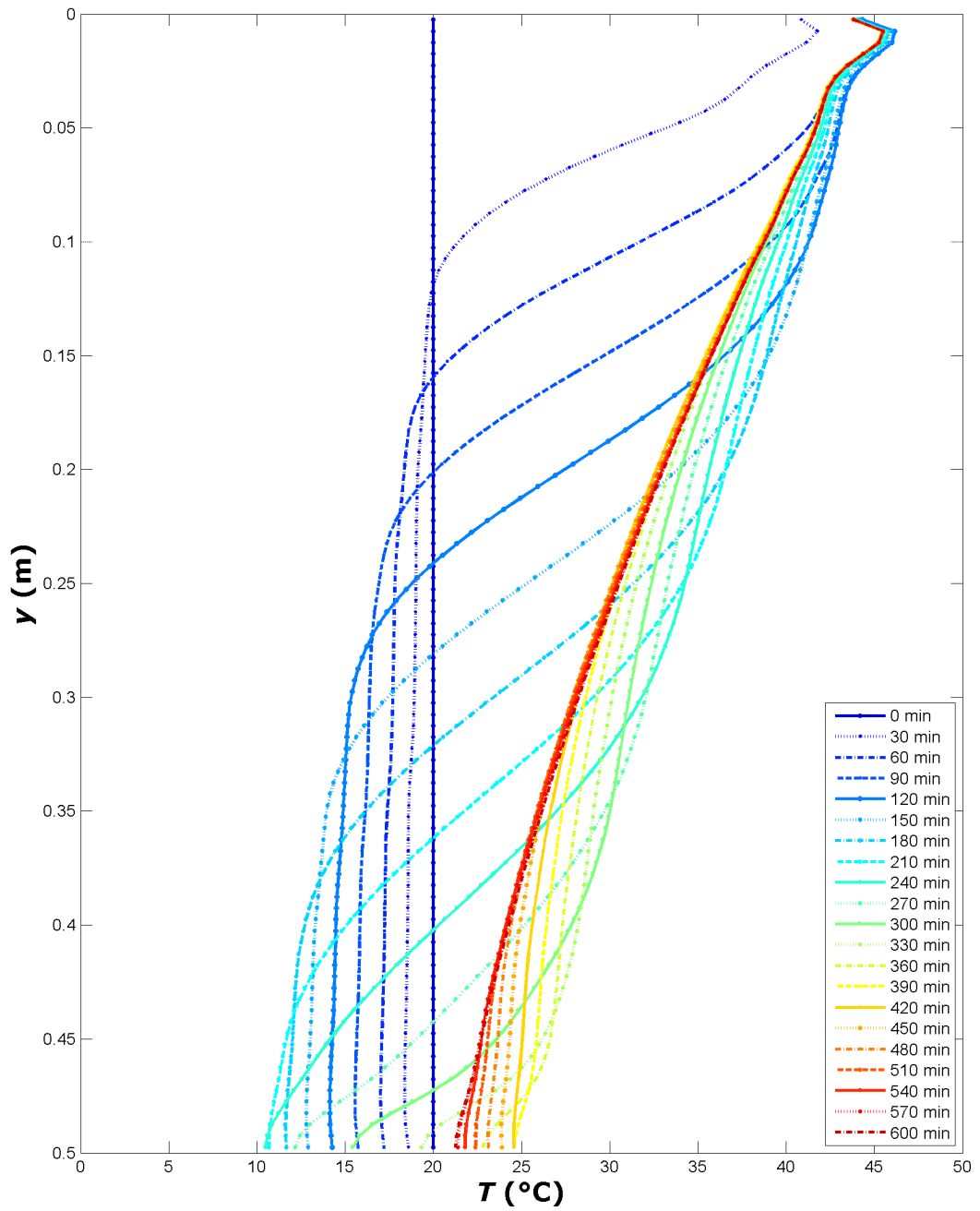


Fig. 7.11 Development of Vertical Temperature Profile within Cavity at $x = 1$ m for Simulation 12

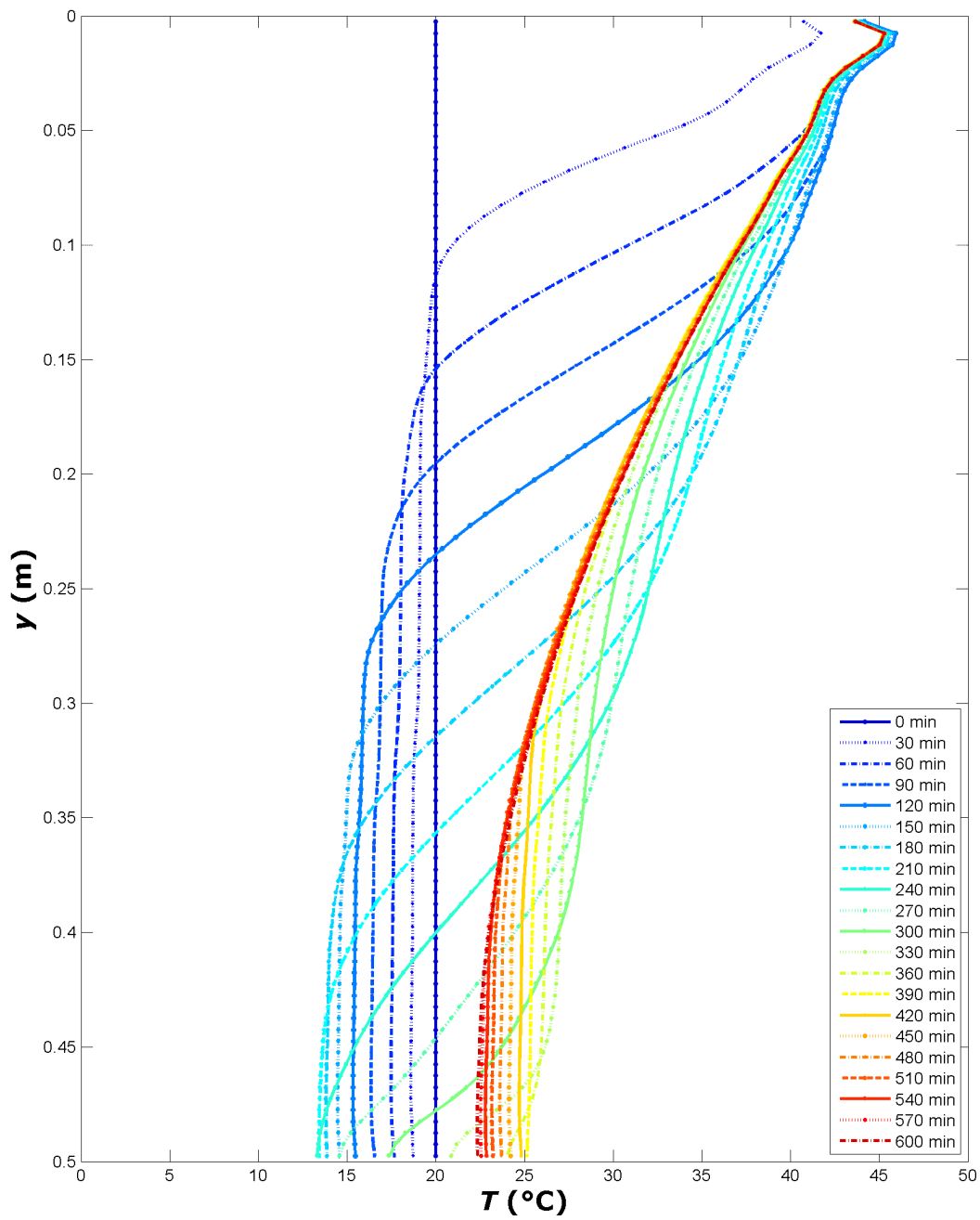


Fig. 7.12 Development of Vertical Temperature Profile within Cavity at $x = 1\text{m}$ for Simulation 13

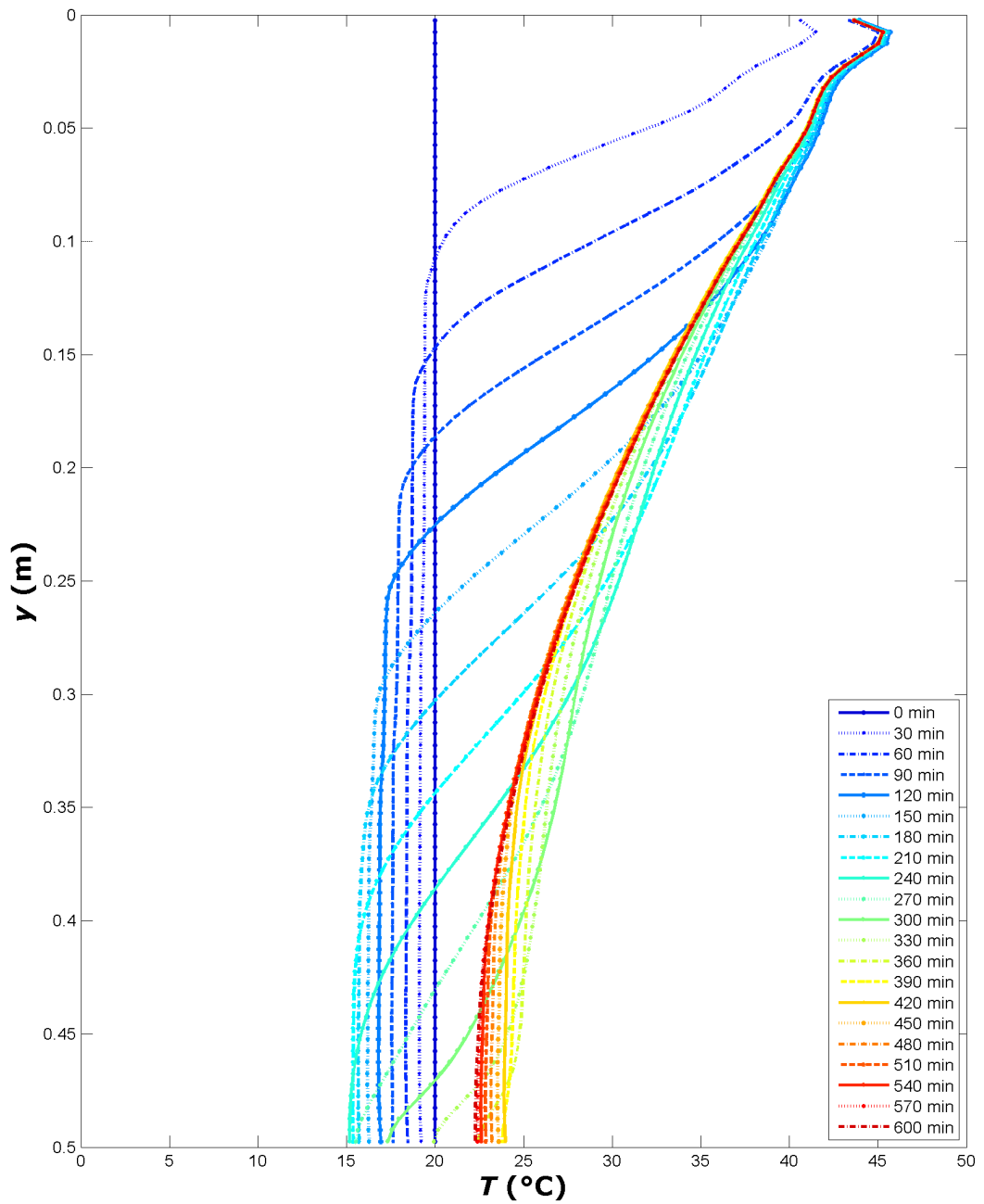


Fig. 7.13 Development of Vertical Temperature Profile within Cavity at $x = 1$ m for Simulation 14

7.3 Conservation of Energy Equation for the Cavity in Time-Rate Form

The 1st Law of Thermodynamics for the cavity in the time-rate form could be written as;

$$\frac{dE_{st}}{dt} = \dot{E}_{in} - \dot{E}_{out} \quad (7.14)$$

The energy inflow to the CV is simply the enthalpy of hot water that is supplied to the cavity.

$$\dot{E}_{in} = \dot{H}_{in} \quad (7.15)$$

The energy outflow from the C.V. is the summation of the total heat loss rates and the enthalpy outflow of the relatively cooler water exiting the outlet. Heat losses are from the free surface to the ambient and from the two vertical side walls.

$$\dot{E}_{out} = \dot{H}_{out} + \dot{Q}_{free_surface} + \dot{Q}_{side_wall1} + \dot{Q}_{side_wall2} \quad (7.16)$$

Hence the energy equation becomes;

$$\frac{dE_{st}}{dt} = \dot{H}_{in} - \dot{H}_{out} - \dot{Q}_{free_surface} - \dot{Q}_{side_wall1} - \dot{Q}_{side_wall2} \quad (7.17)$$

The enthalpy transfer terms can be grouped as;

$$\dot{H}_{in} - \dot{H}_{out} = \dot{m}_{in} h_{in} - \dot{m}_{out} h_{out} = \rho h u_{in} h_{in} - \rho \int_{H-h}^H u(L+l, y) h(L+l, y) dy \quad (7.18)$$

Since u_{in} and h_{in} are constants, they can be put within the integral in equation (7.18)

$$\dot{m}_{in} h_{in} - \dot{m}_{out} h_{out} = \rho \int_{H-h}^H [u_{in} h_{in} - u(L+l, y) h(L+l, y)] dy \quad (7.19)$$

At this moment, if the velocity profile at the outlet, $u(L+l, y)$, is roughly approximated to be equal to the inlet velocity

$$u(L+l, y) \cong u_{in} \quad (7.20)$$

Then the net enthalpy transfer rate to the cavity becomes;

$$\begin{aligned}
\dot{H}_{in} - \dot{H}_{out} &\cong \rho u_{in} \int_{H-h}^H [h_{in} - h(L+l, y)] dy \\
&= \rho c_p u_{in} \int_{H-h}^H [T_{in} - T(L+l, y)] dy
\end{aligned} \tag{7.21}$$

An average outlet temperature can be computed with the computational data at any time.

$$T_{out} = \frac{1}{h} \left[\int_{H-h}^H T(L+l, y) dy \right] \tag{7.22}$$

In the end the net enthalpy transfer becomes;

$$\dot{H}_{in} - \dot{H}_{out} = \rho c_p h u_{in} (T_{in} - T_{out}) \tag{7.23}$$

There are convective and evaporative heat losses from the free surface. Also there may be solar radiation onto the free surface.

$$\begin{aligned}
\dot{Q}_{free_surface} &= \dot{Q}_{conv} + \dot{Q}_{evap} - \dot{Q}_{solar} = \int_0^L h_{conv} (T(x,0) - T_{amb}) dx \\
&+ \left[\int_0^L h_{evap} (\rho_w (@T(x,0)) - \phi \rho_w (@T_{amb})) h_{fg} (@T(x,0)) dx \right] - q''_{solar} L
\end{aligned} \tag{7.24}$$

The heat loss rate from the vertical side walls can be computed from the appropriate wall heat flux function over the walls;

$$\dot{Q}_{side_wall1} + \dot{Q}_{side_wall2} = \int_h^H q''_{wl}(0, y) dy + \int_0^{H-h} q''_{wl}(L, y) dy \tag{7.25}$$

Finally, the energy conservation equation becomes;

$$\begin{aligned}
\frac{dE_{st}}{dt} &= \rho c_p h u_{in} (T_{in} - T_{out}) + \int_0^L h_{conv} (T(x,0) - T_{amb}) dx \\
&+ \left[\int_0^L h_{evap} (\rho_w (@T(x,0)) - \phi \rho_w (@T_{amb})) h_{fg} (@T(x,0)) dx \right] - q''_{solar} L \\
&+ \int_h^H q''_{wl}(0, y) dy + \int_0^{H-h} q''_{wl}(L, y) dy
\end{aligned} \tag{7.26}$$

Monitoring of the rate of energy storage term $\frac{dE_{st}}{dt}$ is a mean for determination of steadiness in the computation. As the rate of energy storage vanishes (during charging),

no more energy is stored within the cavity, the energy input rate to the cavity is equal to energy output rate from the cavity, and hence steady velocity and temperature fields are achieved within the cavity.

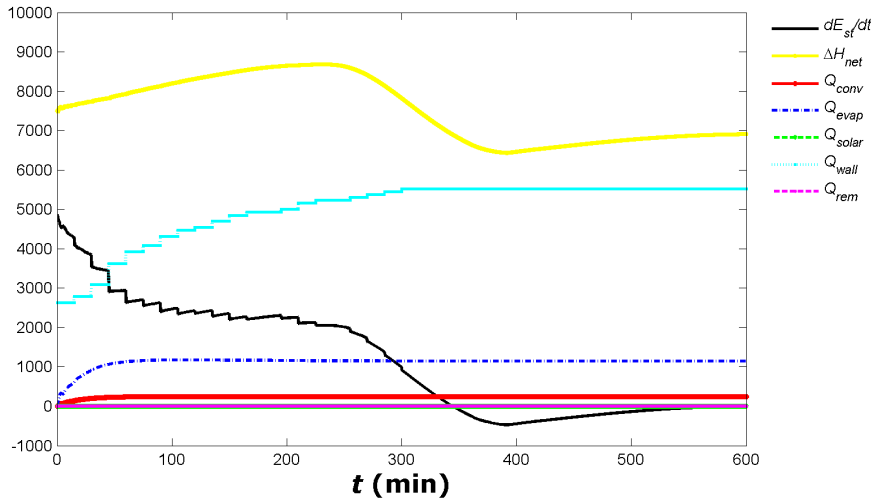


Fig. 7.14 Variation of Components of Energy Equation in Time-Rate Form for Simulation 14

The temporal variations of the components in the Conservation of Energy Equation for Simulation 14 is plotted in Fig. 7.14. The heat removal rate plot is redundant since there is no heat removal in this simulation. Also there is no solar radiation on the free-surface. The heat loss from the side walls show a stepwise variation up to 300min due to the stepwise variation of the heat flux boundary condition applied on the vertical walls. This stepwise variation is directly transferred to the rate of change of energy storage. The energy storage rate reaches negative values at around $t=350$ min, thus cavity loses energy at that interval. Furthermore the rate of energy storage decreases until a bottom is reached before $t=400$ min. After this time negative energy storage rate slowly diminishes and the cavity reaches steady flow around $t=550$ min. The variations after $t=600$ min up to $t=1200$ min can be found in Fig. B.2 in Appendix, emphasizing the steadiness of the flow after around $t=550$ min.

The cause of the negative storage rate interval can be seen in Fig. 7.13. Around this $t=350$ min, the temperature of the region adjacent to the bottom surface increases fast, yielding a rapid increase in the enthalpy loss from the cavity through the outlet. In addition, in Fig. B.6, development of vertical temperature profile nearest the side wall at $x=2$ m for Simulation 14 is presented. These are the vertical temperature profiles developing within the cavity closest to the outlet. Same trend can also be followed in this figure.

Examination of Fig. 7.14 reveals that the rate of convective and evaporative heat losses attains steady values way before the flow reaches steady-state. Though these losses are calculated from the interface temperature that is updated at every time interval, the losses reach their steady and maximum values at around $t = 50 \text{ min}$, indicating that the near surface regions reach steady-state early in the simulations.

The steadiness check can be also done by comparison of the velocity fields at successive time periods. The streamlines of the flow field supplied in the next section can be a tool for this steadiness check.

Yet another tool for the steadiness check of the flow can be the comparison of the temperature field of the flow at successive time periods. Temperature field at different times for a simulation will also be presented in the next section. Also as previously done, monitoring the development of vertical temperature profile within the cavity can be a tool at determining the flow steadiness. As flow approaches steadiness, successive vertical temperature profiles almost coincide.

7.4 The Flow Field

The developing velocity vectors within the cavity (excluding the inlet and the outlet) for Simulation 14 are presented in Fig. 7.15. From the start until the end, velocity vectors with highest magnitudes occur near the free-surface, since a free surface has no friction to the flow. Actually velocity magnitudes of around 0.0085 m/s , more than 5.5 times the inlet velocity magnitude of 0.0015 m/s are seen at the interface.

The regions close to the other three boundaries have high velocity magnitudes also. Region on top of the bottom surface has high velocity magnitudes due the suction effect of the outlet whereas regions close to the vertical side walls have high velocity magnitudes due the cooling of these regions with natural convection.

The region away from the boundaries, roughly $0.2 < x < 1.8 \text{ m}$ and $0.2 < y < 0.45 \text{ m}$ is almost motionless.

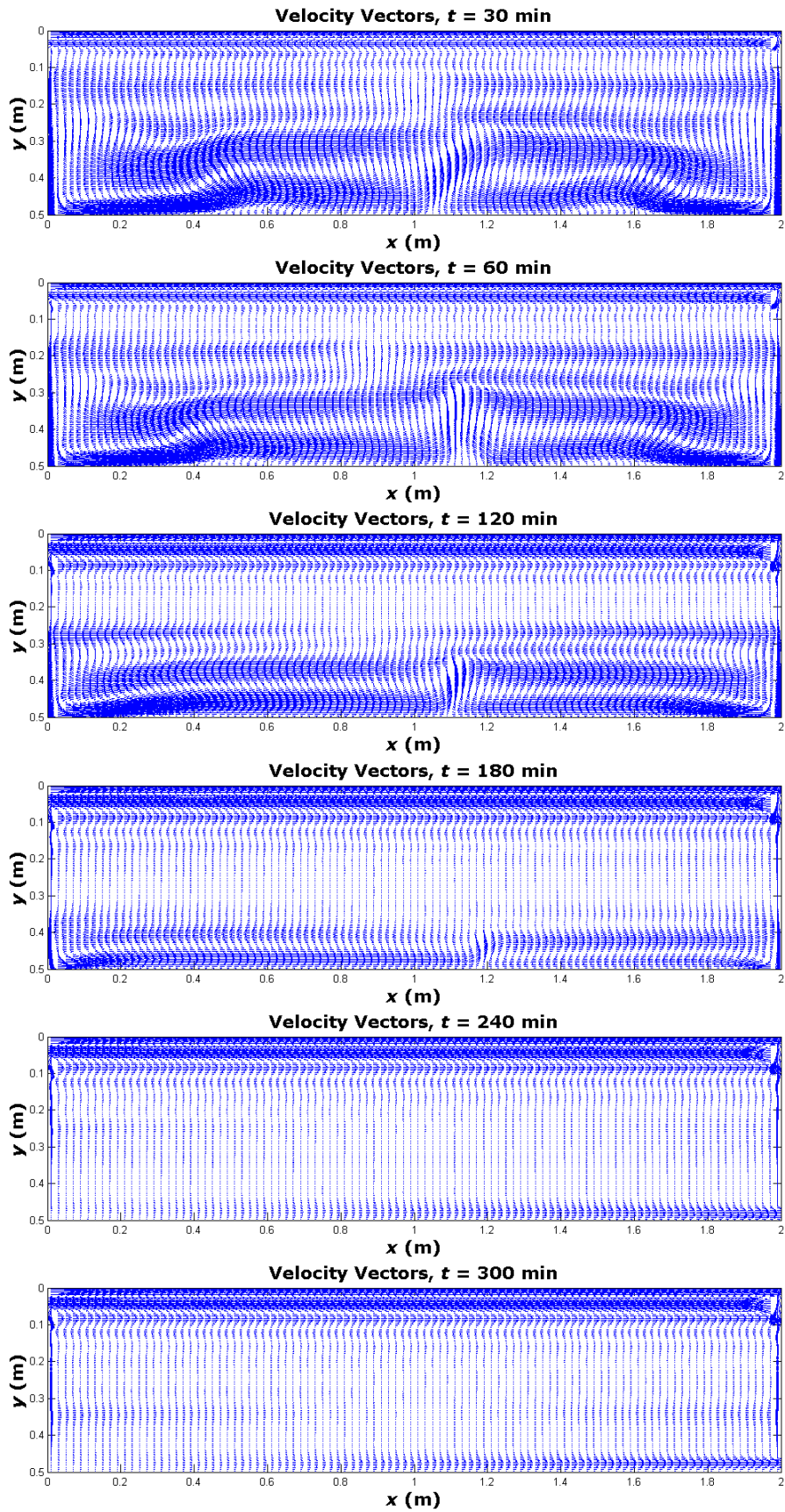


Fig. 7.15 Velocity Vectors within the Cavity during Charging, for Simulation 14

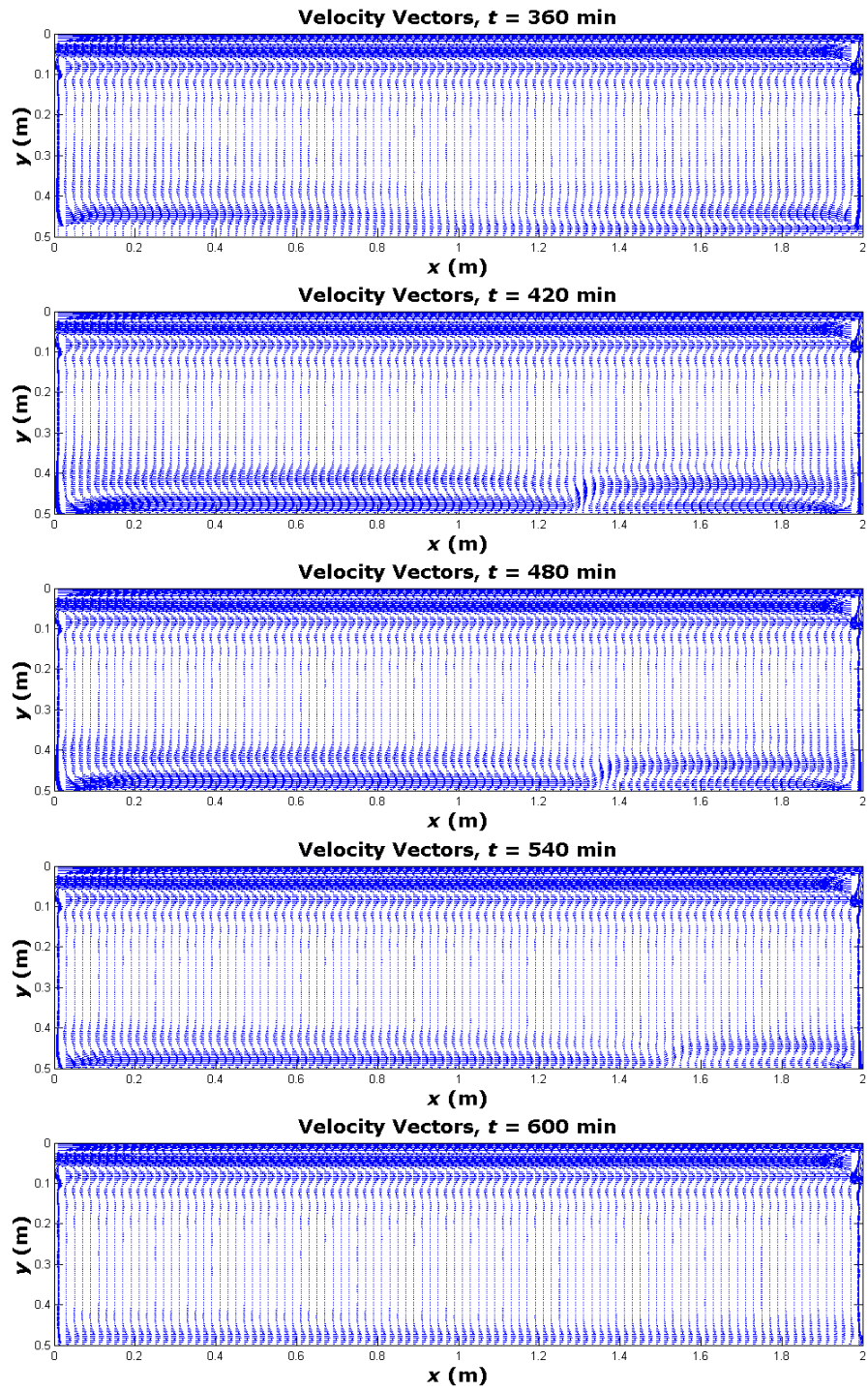


Fig. 7.15 (cont'd)

Streamlines within the cavity and the inlet and the outlet during charging are shown in Fig. 7.16 for Simulation 14. At first glance, the flow does not seem to reach steady-state, since the streamlines do change towards the end of the simulation within the region away from the boundaries. But as previously noted, flow is almost motionless within this region and any minute change in velocity within this region is reflected in the streamlines of Fig. 7.16 as some considerable change.

The flow near the top surface makes a back and forth motion, first it entrains in the vicinity of the interface, reaches the vertical side wall, changes direction and slides down under the newly coming fluid layer from the inlet. Actually at $t = 30$ min this reversed flow even goes all the way across the cavity and leaves from the outlet. As the time goes on, this back and forth motion becomes quite steady and can be seen within around first 40% of the depth as the simulation comes close to the end.

Transient development of temperature distribution within the cavity is presented in Fig. 7.17. A layer by layer temperature development is seen in all of the simulation. Region in the vicinity of the free-surface attains steady temperature values in the very beginning of the run due to the relatively fast convective currents. Away from the boundaries, development is slow indicating that the main heat transfer mode is diffusion.

Away from the vertical side walls, the thermal stratification within the y -direction is quite uniform and does not change with x -direction. This almost uniform temperature distribution in x -direction can also be seen by comparing the vertical temperature profile development of Fig. 7.13 (which is plotted at $x = 1$ m of the cavity) with four different vertical temperature profile development graphs, Fig. B.3 thru B.6 plotted at $x = 0$ m, $x = 0.25$ m, $x = 1.75$ m, and $x = 2.0$ m in Appendix.

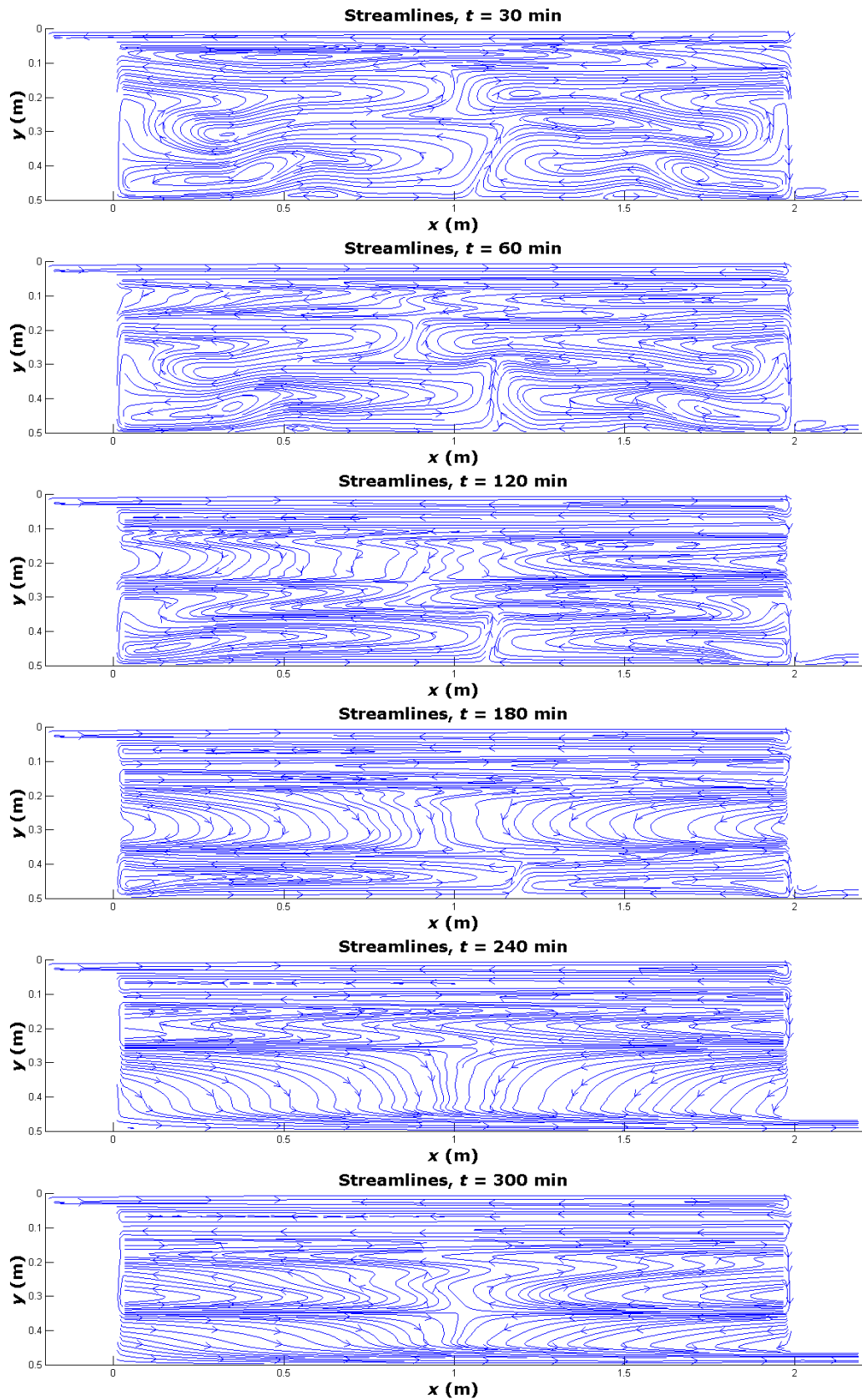


Fig. 7.16 Streamlines within the Cavity during Charging for Simulation 14

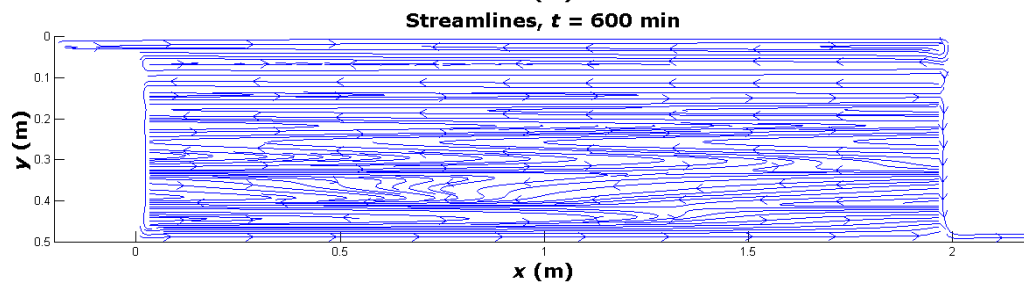
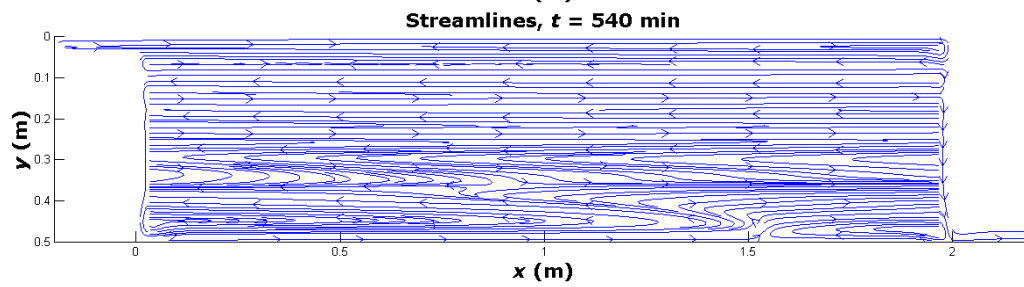
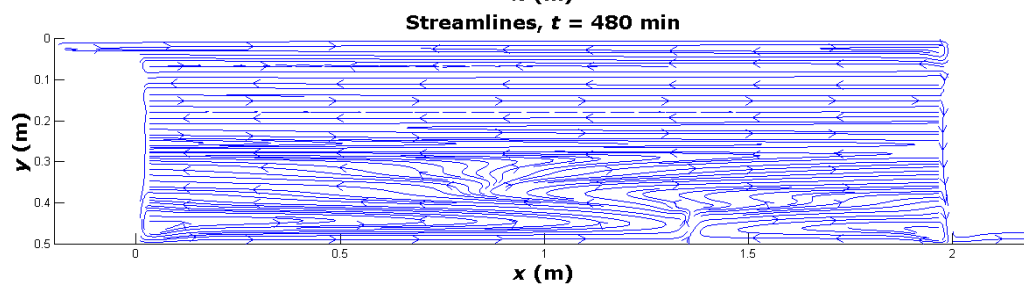
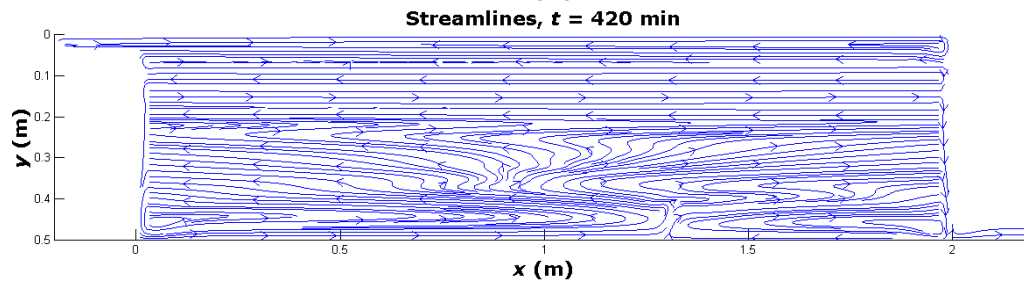
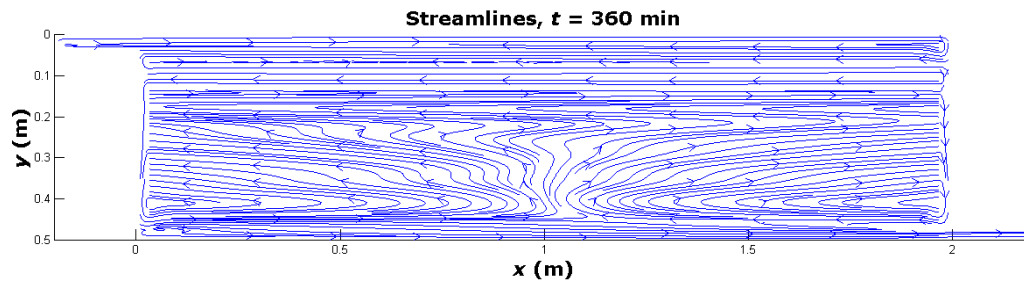


Fig. 7.16 (cont'd)

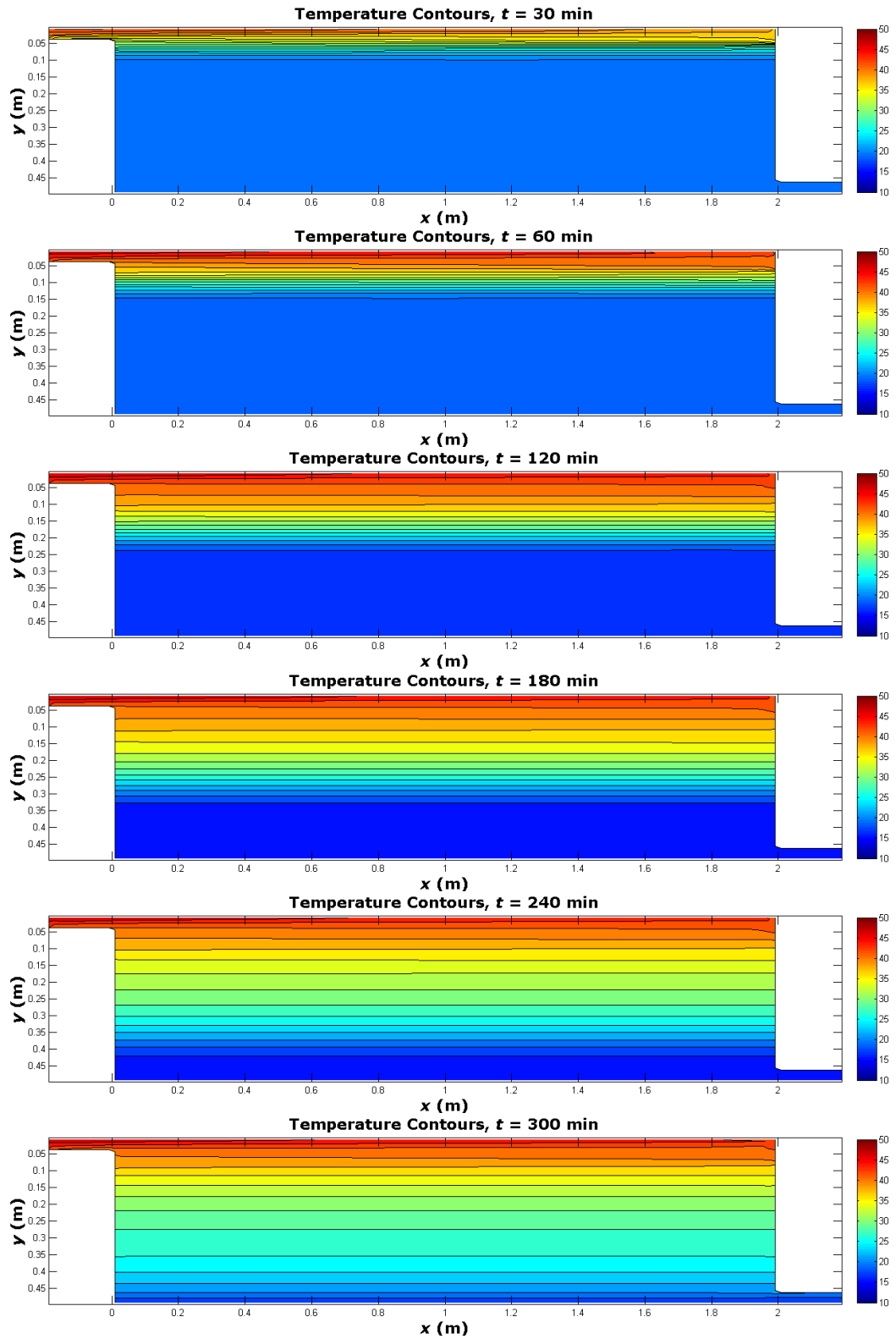


Fig. 7.17 Temperature Distribution within the Cavity and the Inlet and the Outlet during Charging for Simulation 14

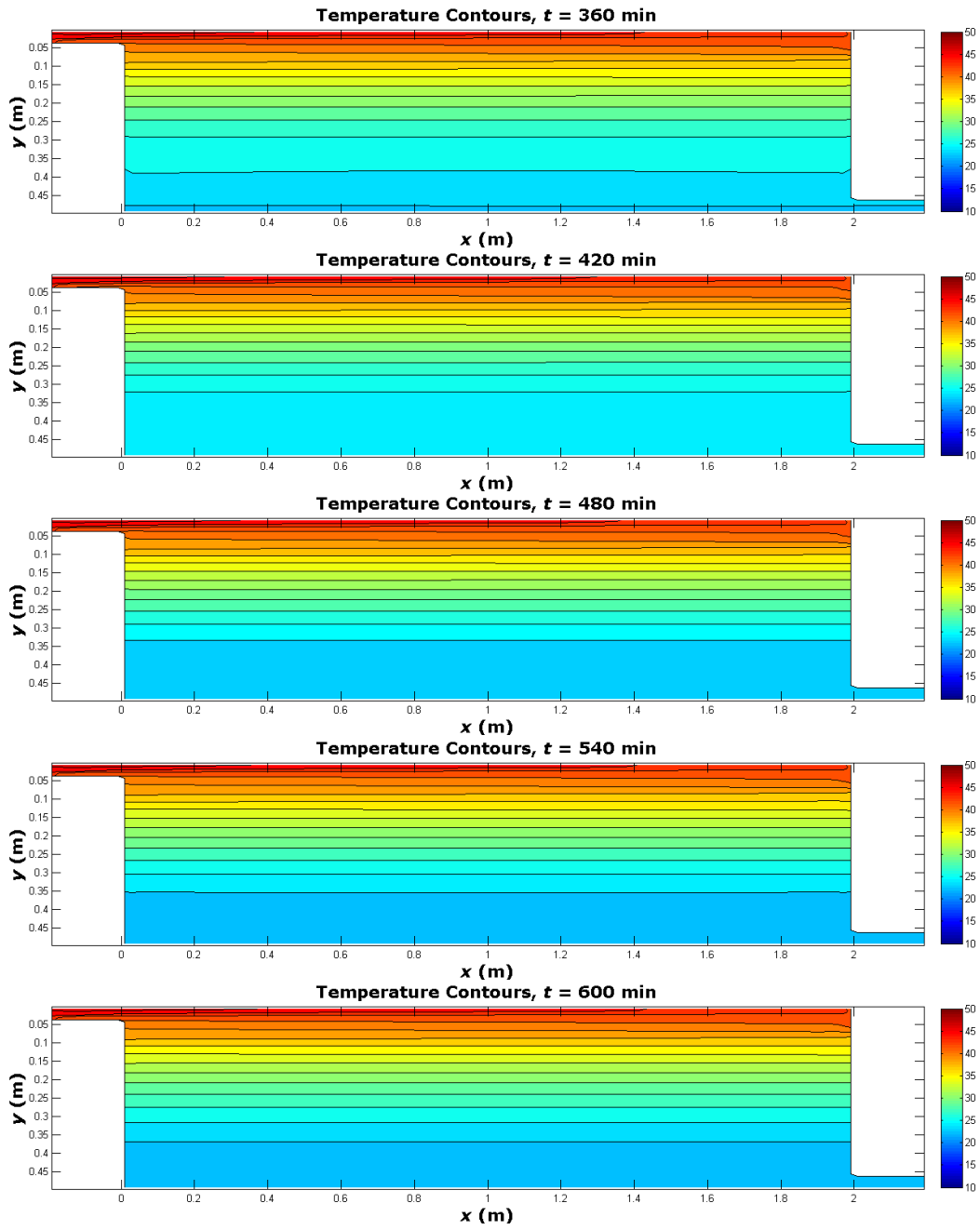


Fig. 7.17 (cont'd)

7.5 Dimensionless Bulk Temperature, θ

Dimensionless Bulk Temperature, θ , is defined as the ratio of the difference of bulk temperature, T_b , of the storage medium at any time t and initial temperature T_{ic} , to the difference between inlet charging temperature, T_{in} , and initial water temperature T_{ic} .

$$\theta(t) = \frac{T_b(t) - T_{ic}}{T_{in} - T_{ic}} \quad (7.27)$$

Bulk temperature for a rectangular 2D cavity at any time can be defined as;

$$T_b(t) = \frac{E_{st}(t)}{\rho c_p HL} + T_{ic} \quad (7.28)$$

Stored thermal energy within the cavity at any time can be calculated by;

$$E_{st} = \rho c_p \int_0^L \int_0^H [T(x, y, t) - T_{ic}] dy dx \quad (7.29)$$

Hence the bulk temperature becomes;

$$T_b(t) = \frac{1}{HL} \int_0^L \int_0^H [T(x, y, t) - T_{ic}] dy dx + T_{ic} = \frac{1}{HL} \int_0^L \int_0^H T(x, y, t) dy dx \quad (7.30)$$

Dimensionless bulk temperature is bounded by unity from above. It gets its steady value, θ_L , after the charging of the cavity is complete.

Dimensionless bulk temperature represents the available energy that can be stored within the storage unit. When θ reaches its steady value of θ_L during the charging process, no further energy storage within the storage unit is possible. A steady-state temperature distribution is achieved in the storage unit at this time and heat removal process can be started. During the heat removal process, if simultaneous charging of the storage unit is stopped, the calculation of θ becomes meaningless by its definition, since charging temperature, T_{in} , is undefined. On the other hand, if simultaneous charging of the storage unit is continued during the heat removal process, θ decreases asymptotically to another steady value. From this time on energy input rate to the storage unit becomes equal to the heat removal rate from the storage unit plus the rate of total heat loss.

Variation of the dimensional bulk temperature of the cavity for Simulation 14 is presented in Fig. 7.18. It reaches a peak value of 0.36 at $t = 330$ min and after reaches a steady value of 0.33. Thus, the trend of losing, rather than gaining, energy for the cavity

for an interval before reaching a steady-state mentioned before in Section 7.3 can also be seen in the variation of dimensionless bulk temperature of the cavity.

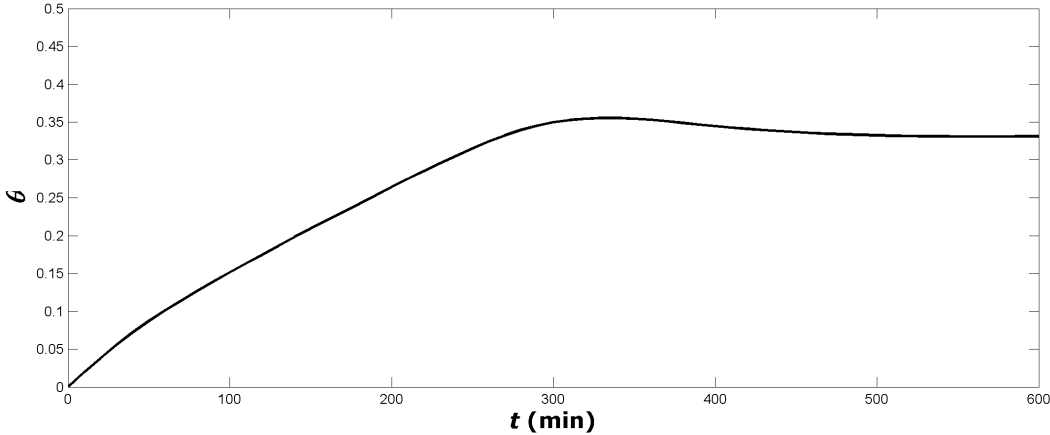


Fig. 7.18 Variation of Dimensionless Bulk Temperature Distribution within the Cavity during Charging for Simulation 14

7.6 Effect of Initial Temperature

Fig. 7.19 thru 7.21 show the vertical temperature development of three simulations, whose only differences from Simulation 14 (see Fig. 7.13) are the initial and ambient temperatures. The initial and ambient temperatures are $T_{ic} = 16^{\circ}\text{C}$, $T_{amb} = 16^{\circ}\text{C}$ in Simulation 15, $T_{ic} = 20^{\circ}\text{C}$, $T_{amb} = 16^{\circ}\text{C}$ in Simulation 16, and $T_{ic} = 24^{\circ}\text{C}$, $T_{amb} = 16^{\circ}\text{C}$ in Simulation 17.

Comparison of the figures reveal that, as the initial temperature increased, the final steady temperature profile shows almost no change from the bottom surface to the free surface. Hence it can easily be concluded that cavity with lower initial temperature stores more energy.

The initial temperature profile is away from the final temperature profile in Fig. 7.19, but as the initial temperature increases, the difference between the steady temperature profile and the initial temperature profile decreases. In fact, in Fig. 7.21 the two profiles even intersect. It can be concluded that in a relative sense, more energy is stored when the initial temperature of the cavity is lower.

The variations of dimensionless bulk temperature are shown in Fig. 7.22. Again the higher storage performance of a cavity with lower initial temperature can be seen.

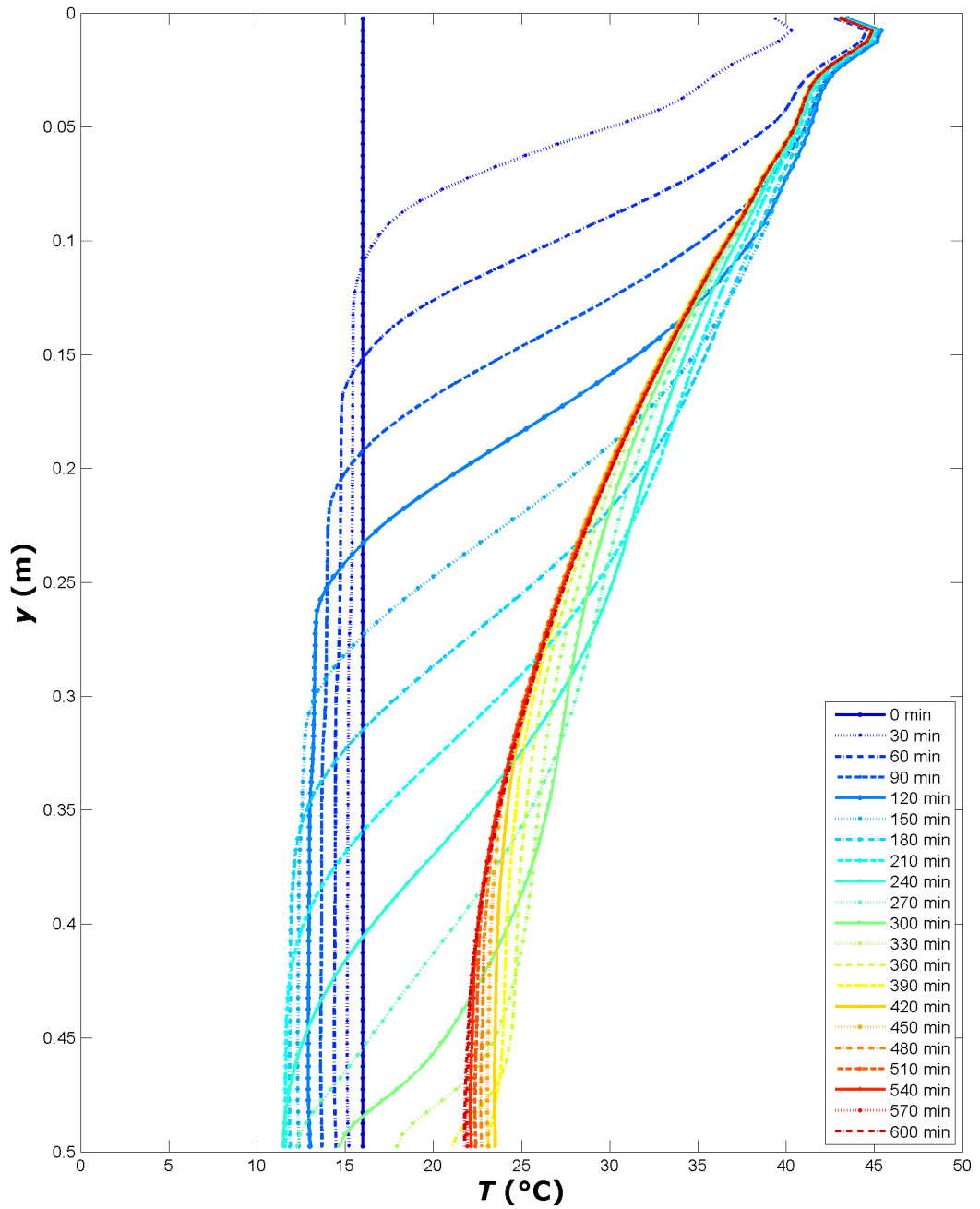


Fig. 7.19 Development of Vertical Temperature Profile within Cavity at $x = 1$ m for Simulation 15, $T_{ic} = 16^{\circ}\text{C}$, $T_{amb} = 16^{\circ}\text{C}$

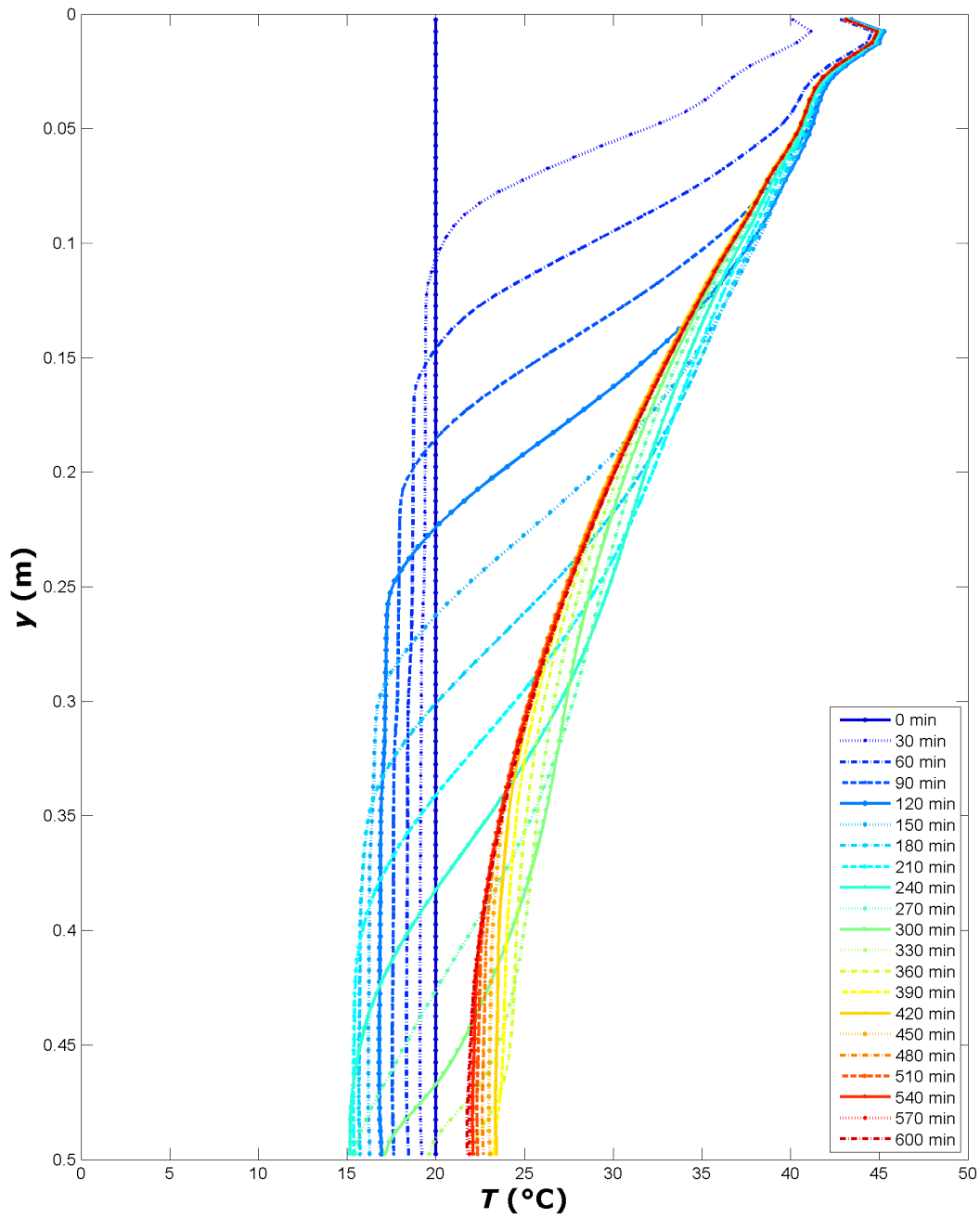


Fig. 7.20 Development of Vertical Temperature Profile within Cavity at $x = 1\text{m}$ for Simulation 16, $T_{ic} = 20^\circ\text{C}$, $T_{amb} = 16^\circ\text{C}$

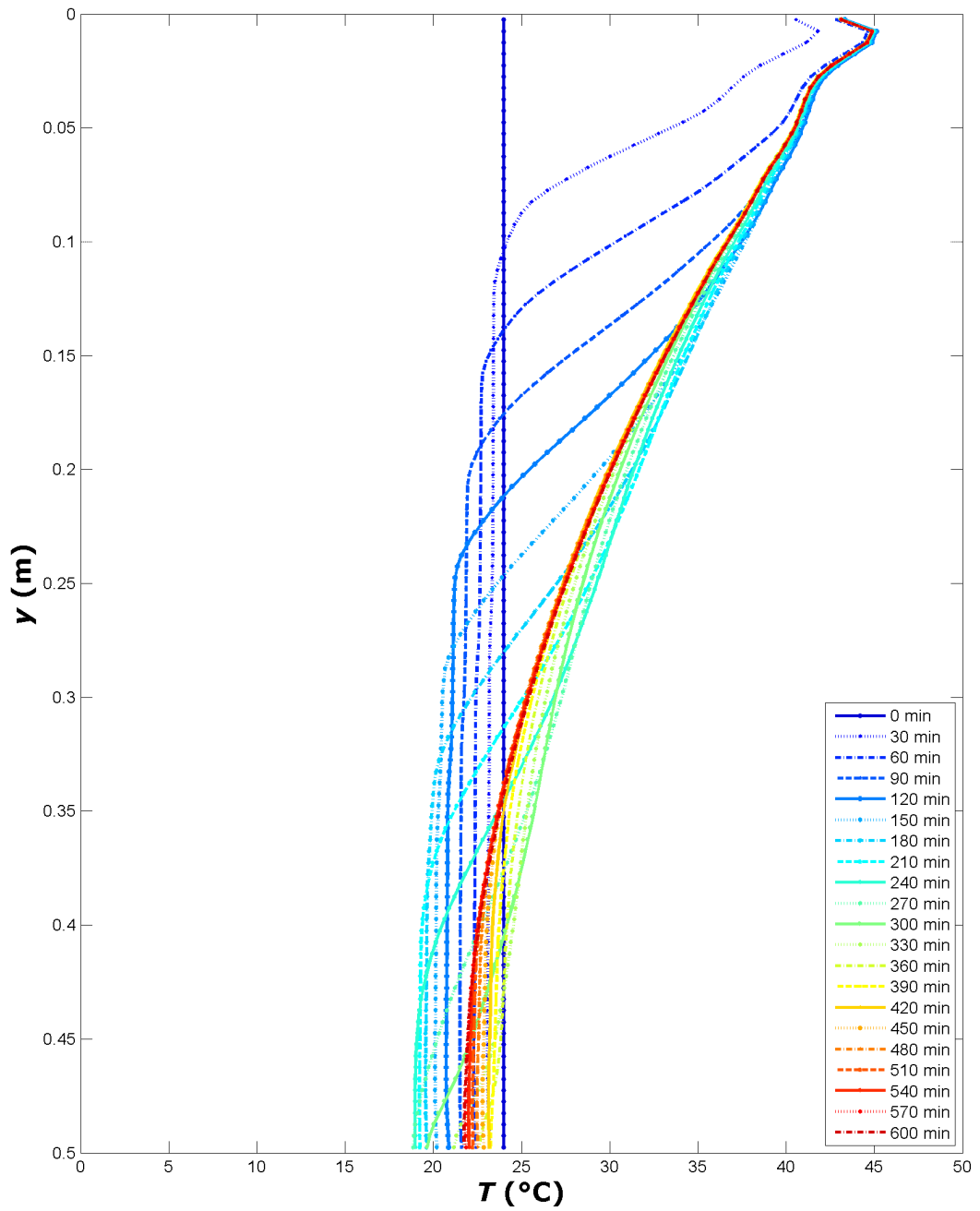


Fig. 7.21 Development of Vertical Temperature Profile within Cavity at $x = 1$ m for Simulation 17, $T_{ic} = 24^{\circ}\text{C}$, $T_{amb} = 16^{\circ}\text{C}$

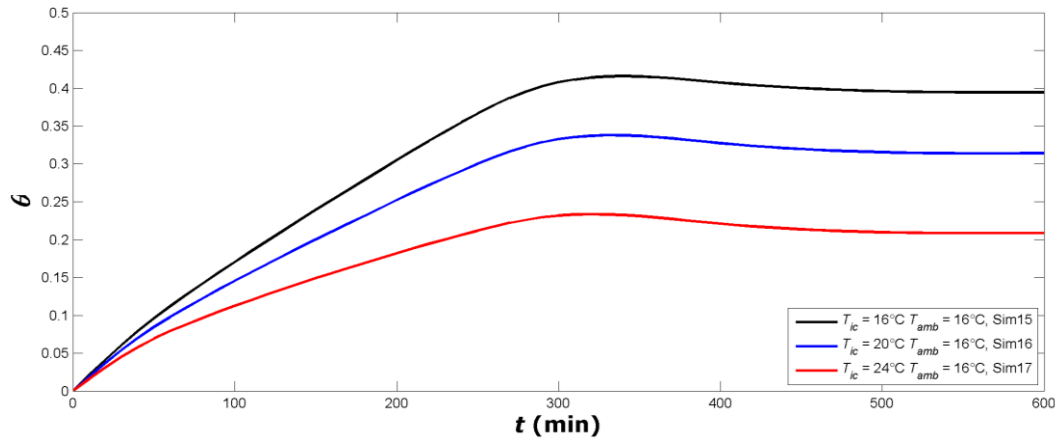


Fig. 7.22 Variation of Dimensionless Bulk Temperature Distribution within the Cavity during Charging for Simulations 15, 16, and 17

7.7 Effect of Ambient Temperature

Fig. 7.23 shows the vertical temperature development of Simulation 19, whose only difference from Simulation 14 (see Fig. 7.13) and from Simulation 16 (see Fig. 7.20) is the ambient temperature. The ambient temperatures are $T_{amb} = 24^{\circ}\text{C}$ in Simulation 14, $T_{amb} = 16^{\circ}\text{C}$ in Simulation 16, and $T_{amb} = 10^{\circ}\text{C}$ in Simulation 19.

Comparison of the figures reveals that, the steady vertical temperature profile for Simulation 19 has the lowest temperature values from top to bottom. As the ambient temperature decreases, the temperature difference between the surface of the cavity and the ambient increases, contributing to a higher heat loss through the free-surface.

The variations of dimensionless bulk temperature are shown in Fig. 7.24. Again the higher storage performance of a cavity with higher ambient temperature can be seen.

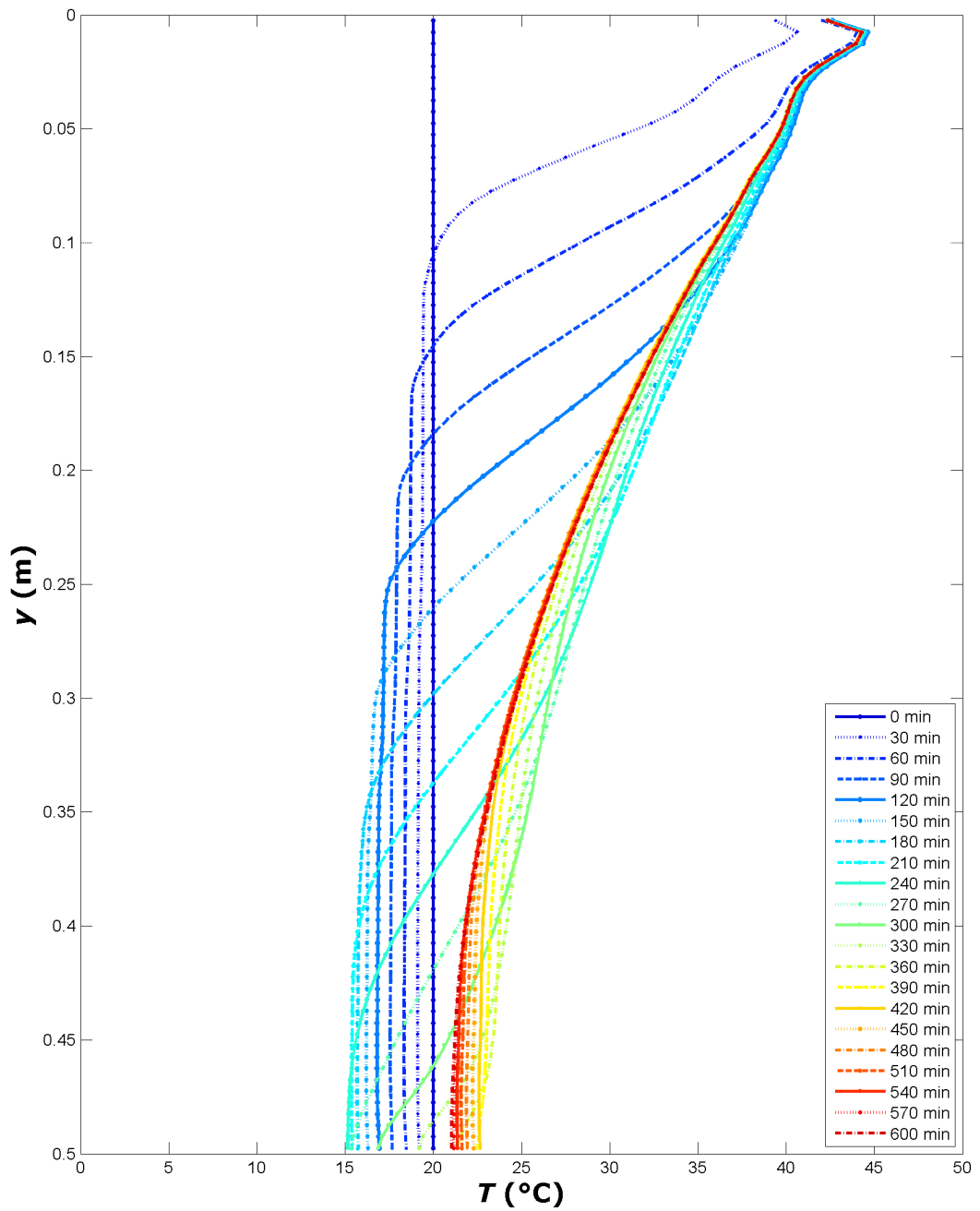


Fig. 7.23 Development of Vertical Temperature Profile within Cavity at $x = 1$ m for Simulation 19, $T_{ic} = 20^\circ\text{C}$, $T_{amb} = 10^\circ\text{C}$

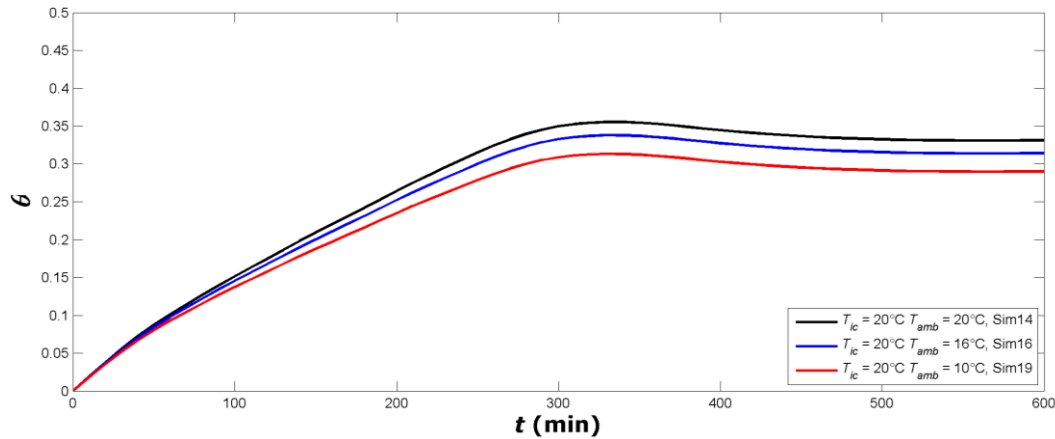


Fig. 7.24 Variation of Dimensionless Bulk Temperature Distribution within the Cavity during Charging for Simulations 14, 16, and 19

7.8 Effect of Inlet Temperature

The effect of inlet temperature on the charging of the cavity is examined by comparing two simulations that differ only in the inlet temperature of water. In Simulation 14 (see Fig. 7.13) inlet temperature is 50°C while in Simulation 20, the inlet temperature is 40°C . The vertical temperature development of Simulation 20 can be found in Fig. 7.25. The comparison of the variations of dimensionless bulk temperature of Simulations 14 and 20 are shown in Fig. 7.26.

The steady-state vertical temperature profile of Simulation 20 shows lower values than the steady-state vertical temperature profile of Simulation 14. If a one-to-one comparison of temperature values at same depths is performed, the temperature difference is found to be around $8\text{--}9^{\circ}\text{C}$ which is lower than the charging temperature difference of the simulations. This is due to the fact that losses from the free-surface increase as the charging temperature is increased.

Comparison of the time variations of dimensionless bulk temperature within the cavity in Fig. 7.26 shows that when every other parameter is kept constant, increasing the charging temperature results in a better thermal storage performance.

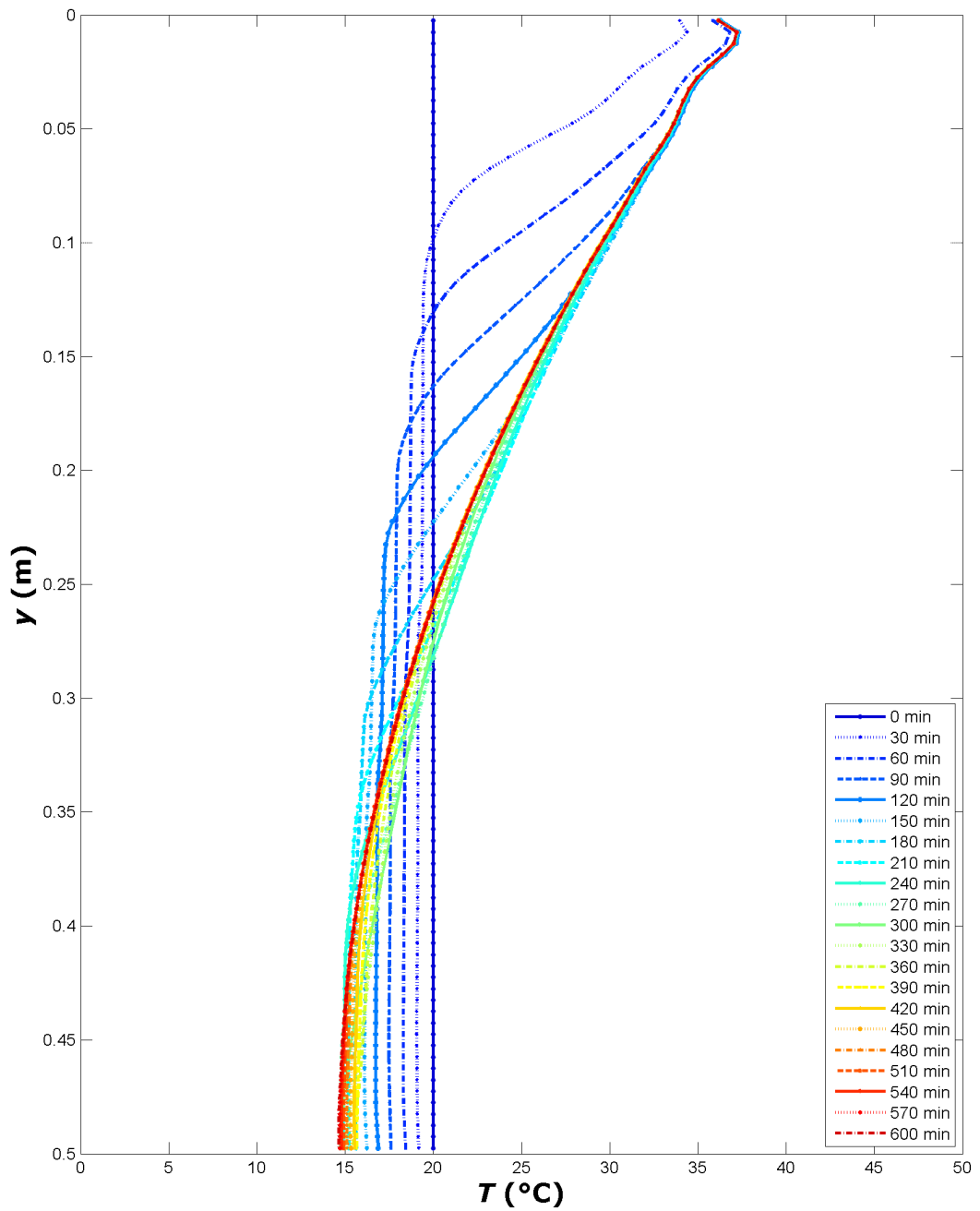


Fig. 7.25 Development of Vertical Temperature Profile within Cavity at $x = 1$ m for Simulation 20, $T_{in} = 40^{\circ}\text{C}$

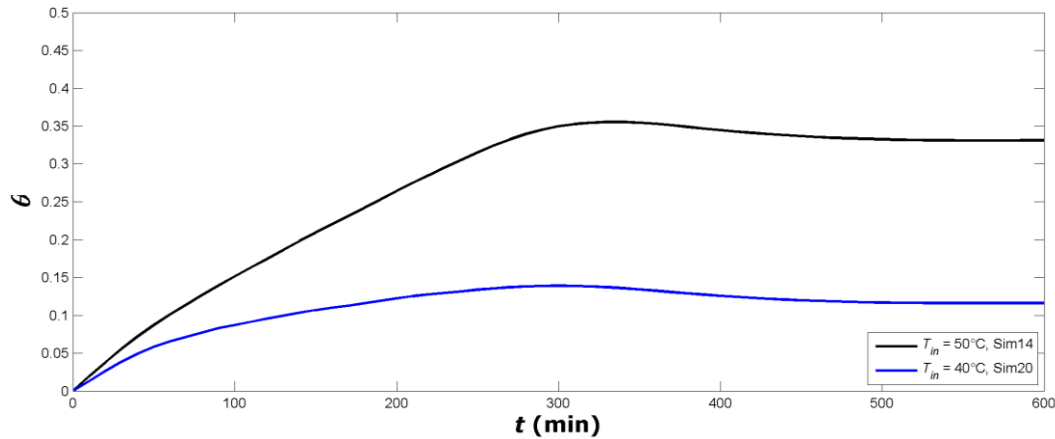


Fig. 7.26 Variation of Dimensionless Bulk Temperature within the Cavity during Charging for Simulations 14 and 20

7.9 Effect of Solar Radiation

The effect of constant solar radiation on the free-surface of cavity can be examined by comparing the vertical temperature profiles of Fig. 7.13 (no solar radiation), Fig. 7.27 (constant solar radiation of 200W/m^2), and Fig. 7.28 (constant solar radiation of 400W/m^2).

Increasing the solar radiation on the free-surface of the cavity increases the rate of penetration of energy into lower levels of the cavity. If temperature profiles at the same time are selected, higher the solar radiation, deeper the effect on energy storage. Dimensionless bulk temperature variation curves (Fig. 7.29) confirm the simple expectation that higher the solar radiation, higher the storage performance.

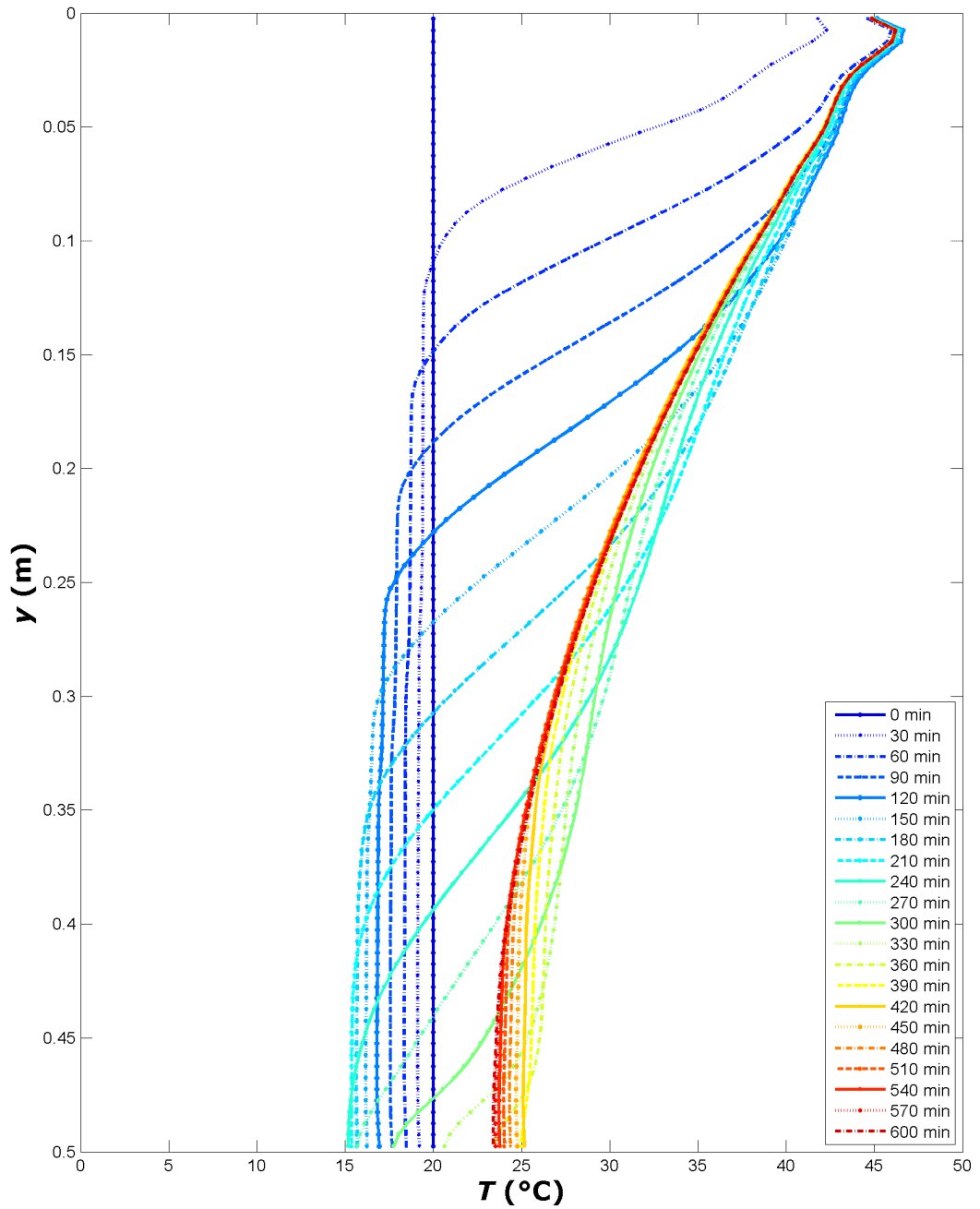


Fig. 7.27 Development of Vertical Temperature Profile within Cavity at $x = 1\text{ m}$
for Simulation 21, $q''_{solar} = 200\text{ W/m}^2$

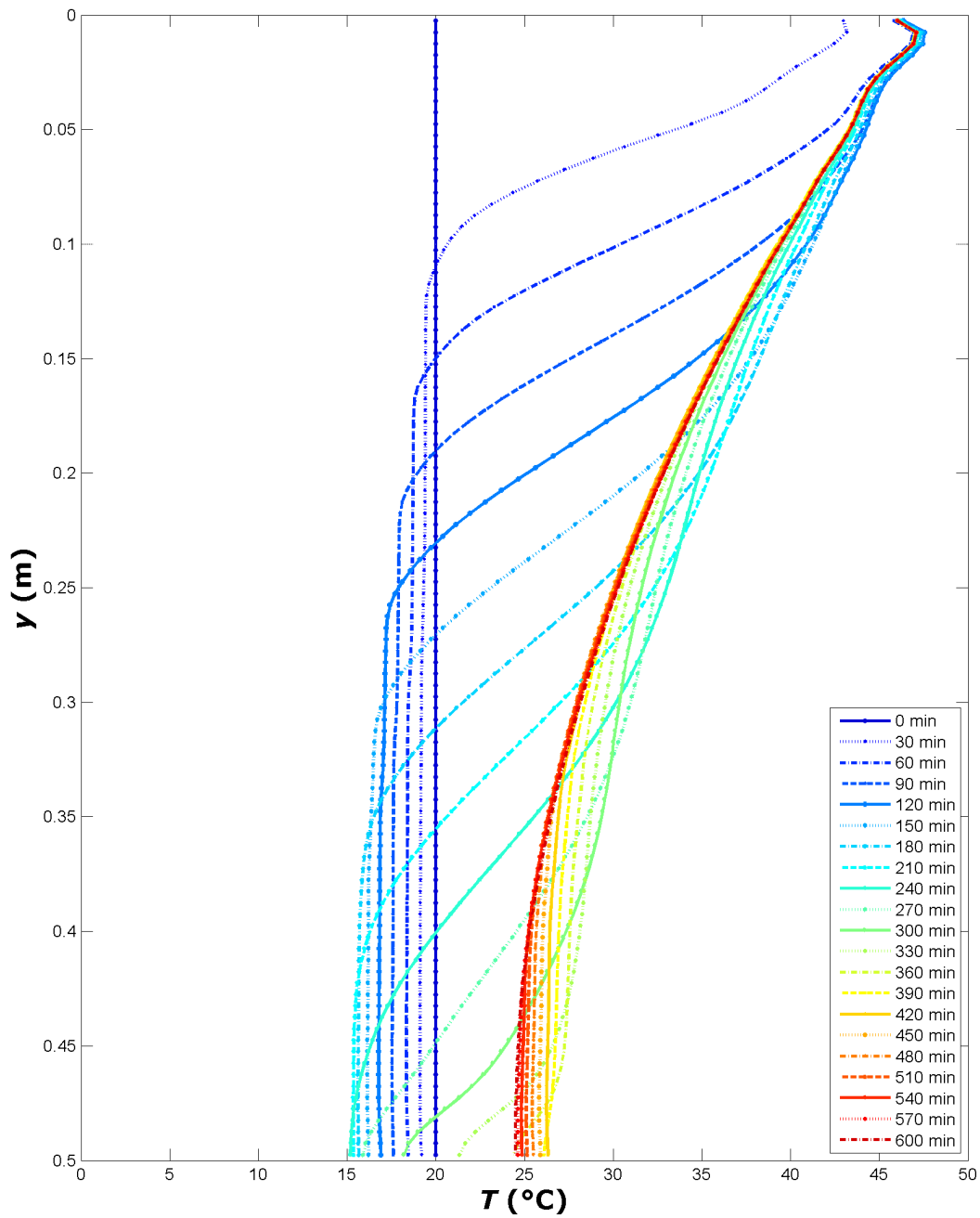


Fig. 7.28 Development of Vertical Temperature Profile within Cavity at $x = 1\text{m}$
for Simulation 22, $q''_{solar} = 400\text{W/m}^2$

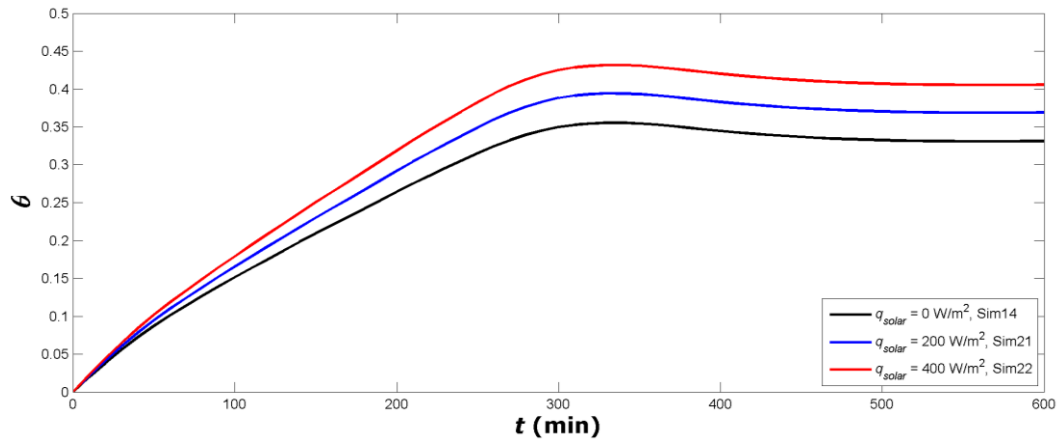


Fig. 7.29 Variation of Dimensionless Bulk Temperature within the Cavity during Charging for Simulations 14, 21 and 22

7.10 Lower Aspect Ratio

The aspect ratio for all the simulations so far was $A = H/L = 0.5/2.0 = 0.25$. A lower aspect ratio, $A = 0.15$, is simulated by decreasing the height of the cavity to 0.3m while keeping the length unchanged. The development of vertical temperature profiles within this shallower cavity is presented in Fig. 7.30. For a comparison with experimental data, Fig. 2.1 could be used.

Although the simulation is run up to $t = 600$ min, steady-state is achieved way before this time, at around $t = 330 - 360$ min.

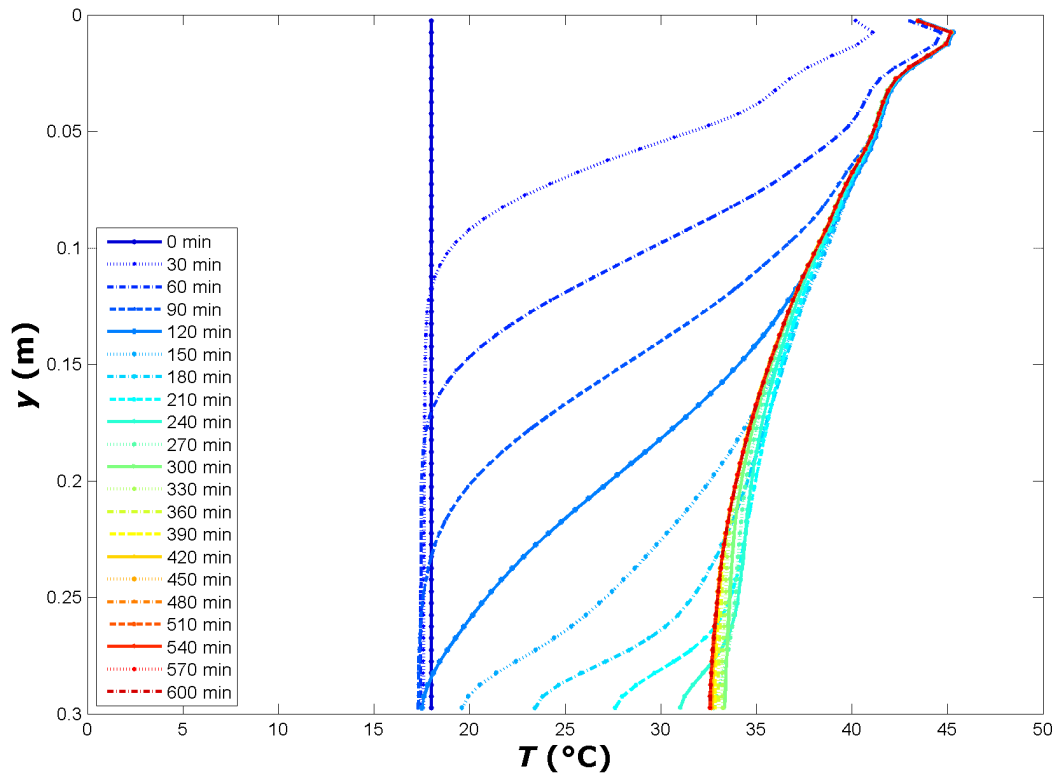


Fig. 7.30 Development of Vertical Temperature Profile within Cavity at $x = 1\text{ m}$ for Simulation 23, $A = 0.15$

7.11 Heat Removal Period

Heat removal from a cavity will be performed by four rectangular tubes located at the same depth, separated from each other with an equal distance of 0.5 m. The first tube is located at 0.25 m. The height and the width of the tubes are equal and are 2 cm. The depths of the tubes are changed at different simulations.

In the code, the tubes are regarded as fluid regions with negative volumetric internal energy generation rates. Hence the tubes are regarded as negative sources in the Finite Volume Equations. In all of the simulations, this negative source is set a constant value, 750000 W/m^3 , in order to gain a constant total heat removal rate of 1200 W per unit depth of the cavity. This heat removal rate is an average value from the experiments performed and though it would change within an experiment temporally and between different experiments due to different sets of flow inputs, in the simulations, it is assumed that it does not change. Actually this means that in the simulations, the heat removal rate is not an output gained from different flow fields, different flow inputs and initial and boundary conditions but rather an equal input to different sets of cavities in order to see their response.

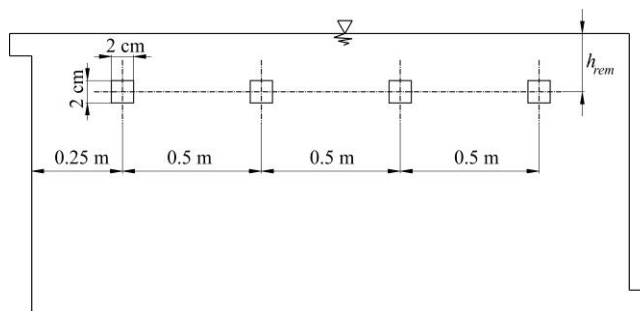


Fig. 7.31 Schematic Drawing of 2D Cavity Showing the Heat Removal Tubes

In the following simulations, the starting point, that is the charged cavity, is the same. It is the steady-state of Simulation 14, or the state of Simulation 14 at $t = 600 \text{ min}$ (see Fig. 7.13 thru 7.18). The heat removal is performed for another period of 600 minutes.

The effect of heat removal on the vertical temperature profiles can be seen in Fig. 7.31 and 7.32. The depth of heat removal tubes is 0.18 m for Simulation 14.1 and 0.06 m for Simulation 14.3. The effect of heat removal is felt more in the layers below the tubes than the layers above the tubes. In fact the effect of heat removal is felt all the way down to the bottom of the cavity whereas only a couple of centimeters above the tubes feel the effect.

Cavity reaches a steady-state in both of the simulations by compensating the extra heat loss due the heat removal by decreasing its enthalpy output due to cooling of the lower layers. The time to reach steady-state is around 360 minutes.

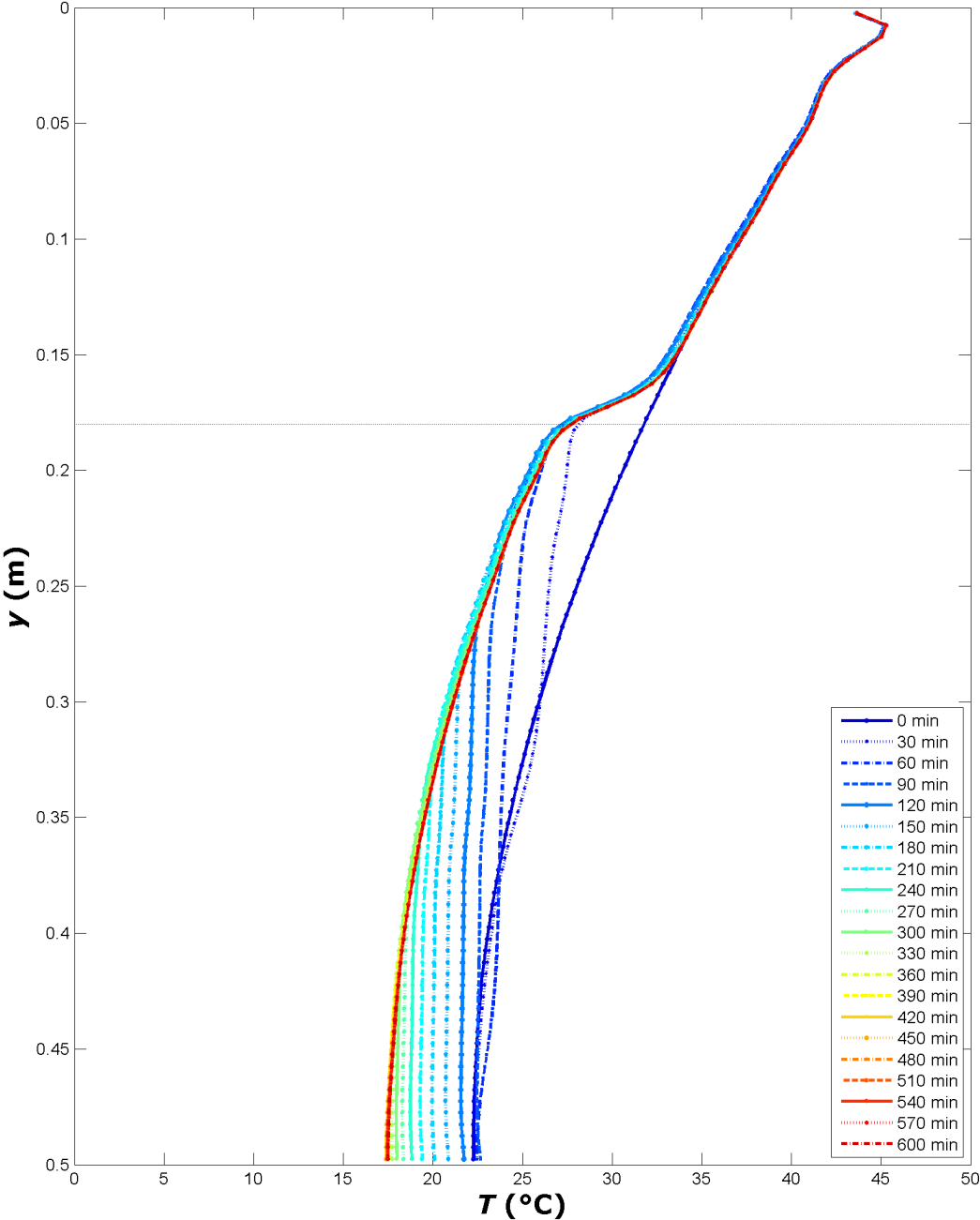


Fig. 7.32 Development of Vertical Temperature Profile within Cavity at $x = 1\text{ m}$ for Simulation 14.1, $h_{rem} = 0.18\text{ m}$

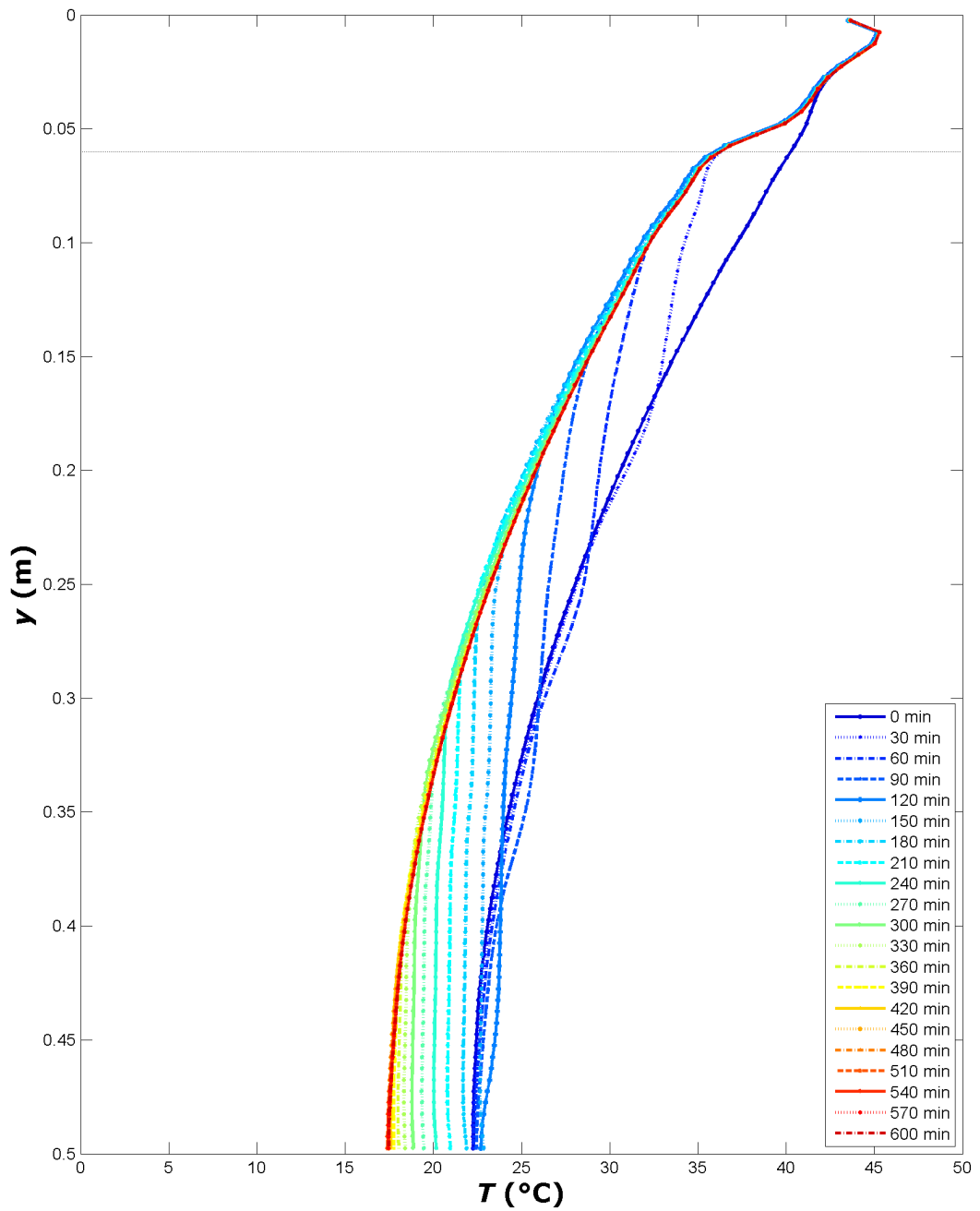


Fig. 7.33 Development of Vertical Temperature Profile within Cavity at $x = 1$ m for Simulation 14.3, $h_{rem} = 0.06$ m

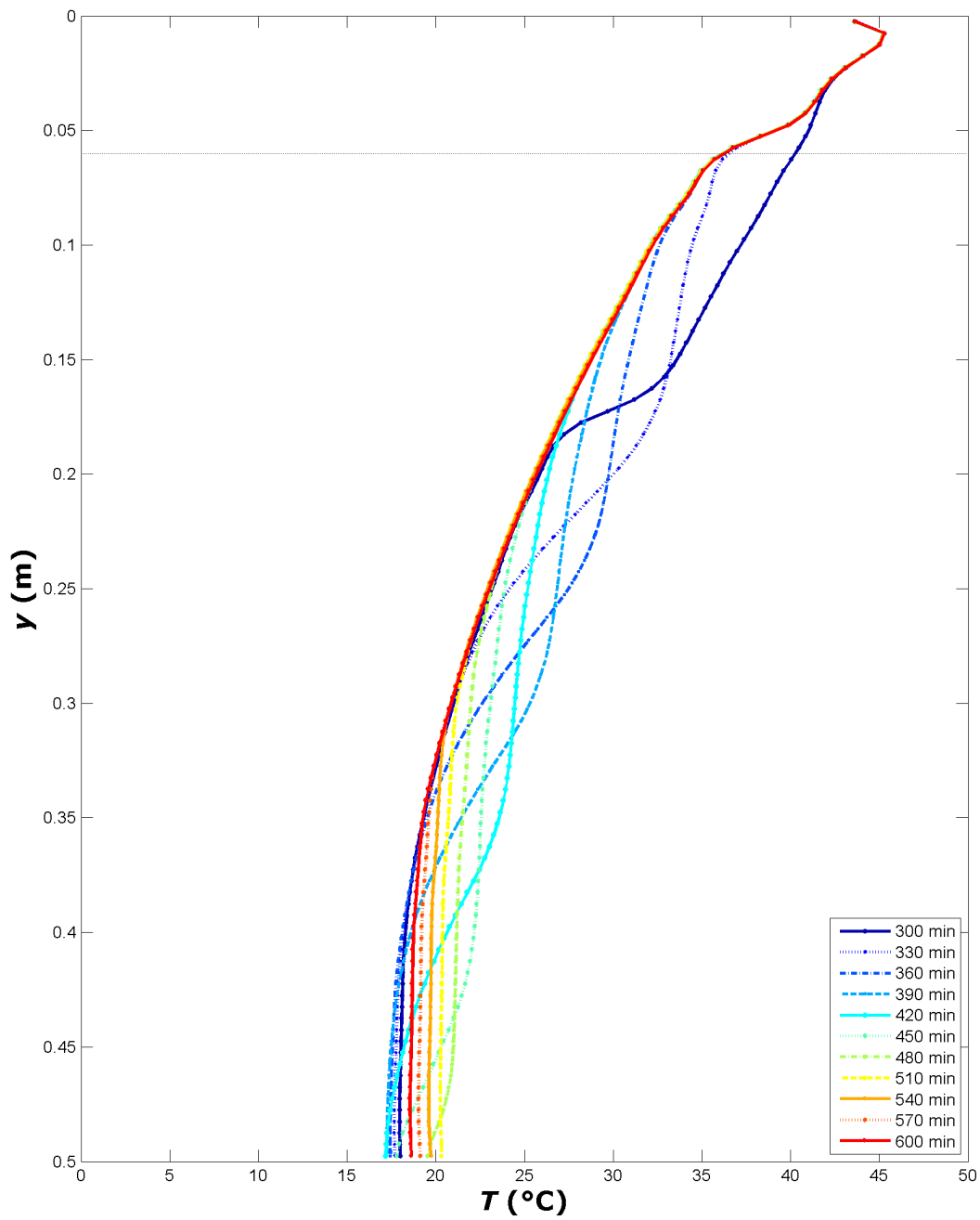


Fig. 7.34 Development of Vertical Temperature Profile within Cavity at $x = 1\text{m}$
for Simulation 14.5, $h_{rem1} = 0.18\text{m}$, $h_{rem2} = 0.06\text{m}$

In Simulation 14.5, heat is removed from $h_{rem1} = 0.18\text{m}$ in the first half of the heat removal period and from $h_{rem2} = 0.06\text{m}$ in the second half. The vertical temperature profiles for the first half of this simulation are the same as the first half of Simulation 14.1. The profiles for the second half are presented in Fig. 7.34. When the heat removal tubes are relocated, the cavity is not at a steady-state (it needs another hour to reach steadiness), when the heat removal is ceased at the end of the simulation, the cavity is not at steady-state either. As it can be seen from the figure, the relocation of the tubes disturbs the flow field fundamentally.

The temporal variations of the components in the Conservation of Energy Equation for Simulation 14.1 is plotted in Fig. 7.35 from the beginning of the charging process to the end of the heat removal. The introduction of heat removal changes the steady zero value of $\frac{dE_{st}}{dt}$ to negative values at 600 minutes. As the drained water temperature drops due to the heat removal from the cavity, the net enthalpy input to the cavity increases contributing an increase in the time rate of energy storage within the cavity until another steady-state is achieved.

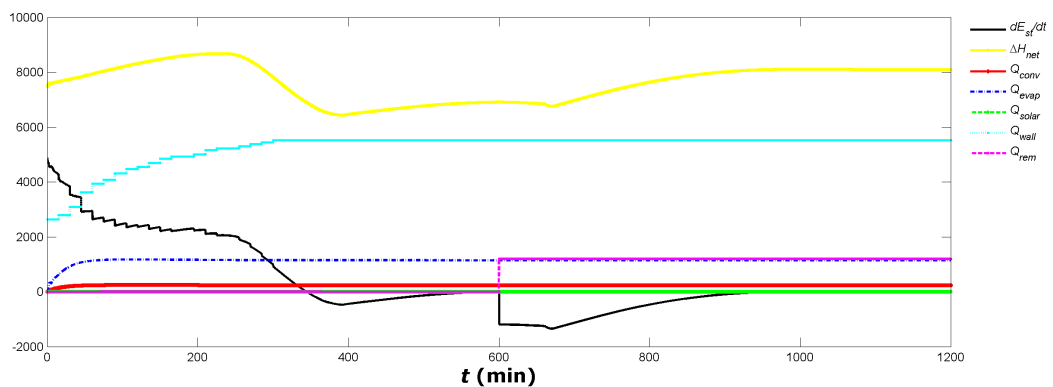


Fig. 7.35 Variation of Components of Energy Equation in Time-Rate Form for Simulation 14.1

The variation of dimensionless bulk temperature for seven different heat removal periods of seven simulations are presented in Fig. 7.36. In the first three simulations the heat removal tubes are at one location throughout the whole heat removal period whereas in the last four simulations the tubes are located at the specified depths for the indicated heat removal periods. At the end of the heat removal periods, when exactly same amount of heat is extracted from different depths and time interval combinations, it is found that Simulation 14.1 retains its stored energy most. Thus, it is better to extract heat from the lower levels of a charged cavity in order to disturb temperature field within the cavity less. Yet, heat removal from lower regions means a smaller temperature difference for the heat removal tubes to extract heat.

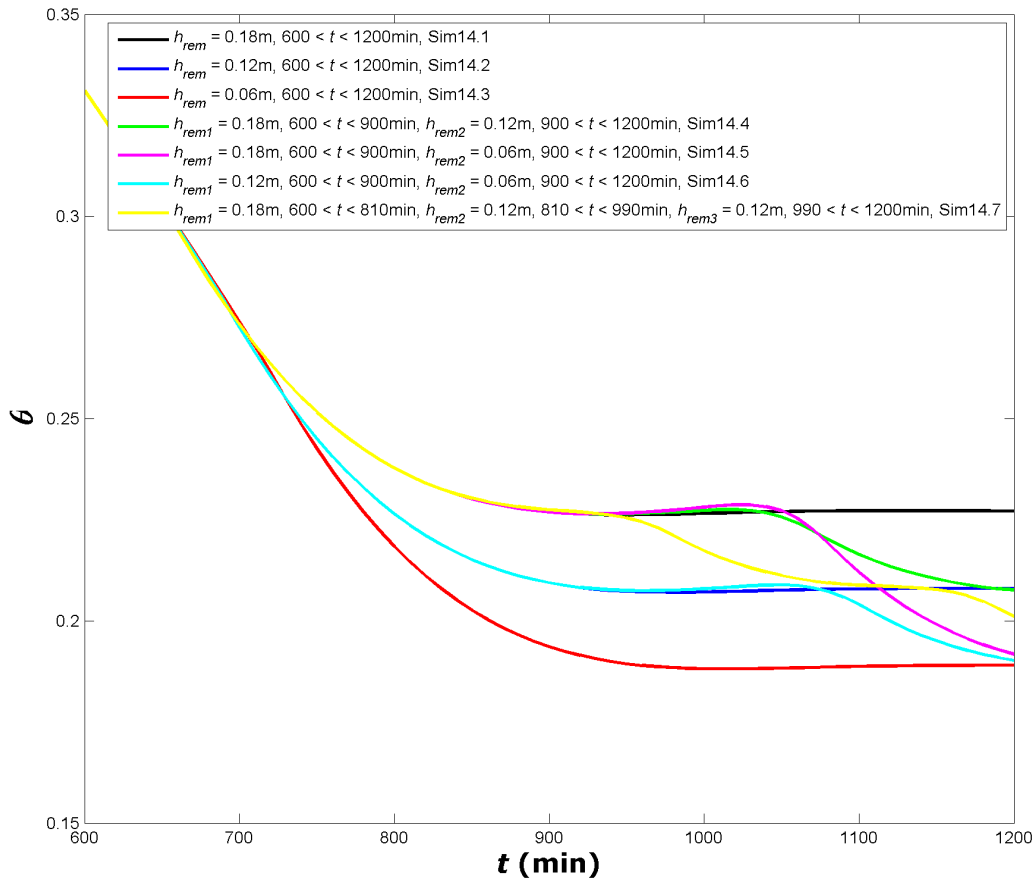


Fig. 7.36 Variation of Dimensionless Bulk Temperature within the Cavity during Charging for Simulations 14.1 thru 14.7

CHAPTER 8

CONCLUSIONS

A numerical study is performed in order to simulate a sensible energy storage filled with water with one inlet and one outlet. Relatively warm water is fed to the cavity to charge it while relatively cooler water is drained from the outlet. The top surface of the cavity is exposed to the ambient air, hence the interaction between the relatively warmer surface of the cavity and the cooler ambient air is inspected.

The mathematical model of the cavity comprised of laminar 2D transient flow of an incompressible fluid. Both the momentum equations and energy equation need to be solved simultaneously to model cavity flow since both forced and natural convection occur in a flow-through storage unit. Boussinesq Approximation is utilized in order to simplify the momentum and energy equations coupling.

Finite Volume Method is chosen to model the governing equations since FVM is the most widely used method of solution, has a rich literature to get help from, and is used by a huge portion of both the CFD/CHT coders and commercial software packages. The solution algorithm for the FVM is Semi-Implicit Method for Pressure-Linked Equations (SIMPLE) which is known for its adequacy for the solution of incompressible flows including natural convection.

The code is written in Standard C++ computer programming language. C++ is a fast, reliable, and easy to code programming language used widely by CFD/CHT programmers. Actually it is one of the two programming languages (the other one is FORTRAN) recommended for CFD/CHT coding by different sources if MATLAB is excluded since it is not an actual computer programming language.

The coding is started from the simplest form of fluid flow, namely the lid-driven cavity flow and advanced step by step introducing complexity to the model. Ports, energy equation, coupling of momentum and energy equations, complex boundary conditions, transient solution are all introduced one by one to the code. If the full mathematical model is attacked at the beginning of the coding, facing lots of errors is inevitable.

Under-relaxation should be introduced to the code at the very beginning. FVM is susceptible to divergence unless under-relaxation (under-relaxation for the momentum

equations and the pressure-correction equation is a must) is used. In all of the simulations presented in CHAPTER 7, the under-relaxation factor is 0.7 for momentum equations and 0.3 for the pressure-correction equation. The energy equation does not necessarily need under-relaxation and the under-relaxation factor is 1.0 (i.e. no under-relaxation) for the energy equation in the simulations.

Source term linearization and always positive coefficients rule are also crucial for the FV Method. When dealing with complex boundary conditions with source terms, if the source is a specified heat flux and its direction is not into the solution domain (i.e. the source is negative or is from the grid to outside), the solution will definitely diverge.

In the simulations of CHAPTER 7, rectangular grids with constant Δx and Δy values are used which simplified the code considerably. Yet a grid of 100×100 size resulted in a computation time around 20,000 seconds of one core of a powerful desktop PC. If in the future, the code is to be advanced such that it can also solve 3D cavities, special grid refinement techniques are required.

The time increment in the simulations has a constant value of 0.1 seconds (a trial-and-error value). It was tried to be increased during the iterations based on the drop in the number of iterations of the inner loop of the SIMPLE algorithm. When the number of iterations dropped to less than a few iterations, the time increment was increased. Yet the trials were all unripe and resulted in divergence of the solution.

Experimental results (obtained during the M. S. study of the author) are used for comparison. The experiments were conducted with a 3D set-up naturally and the set-up utilized complex water jackets in order to remove heat from the vertical side walls at the inlet and outlet of the storage unit. Modeling these heat exchangers in a 2D code is the most problematic part of the computer simulations. A simple Dirichlet or von Neumann boundary condition would not work. A long section is devoted for the selection of the vertical side wall thermal boundary conditions. At the end, both temporally and spatially varying thermal boundary form is selected.

The charging period of the cavity with relatively hot charging water entering the cavity through the inlet is examined. The velocity and temperature fields for the cavity are presented. The flow in the cavity reaches steady-state when the energy input to the cavity is equated by the energy losses from the cavity. At this steady-state, the storage has the highest energy content and is ready for heat extraction. The effects of initial temperature of the cavity, ambient air temperature, inlet charging temperature, and solar radiation on the free surface of the cavity are examined on the performance of the energy storage unit. It is found that lower initial storage temperature, higher ambient air temperature, higher charging water temperature, and existence of solar radiation have positive effects on the performance of the cavity.

Heat removal period from the cavity is examined. In all of the simulations with heat removal, the charging of the cavity is continued. Basic heat removal tubes with

rectangular cross-sections are modeled as negative volumetric internal energy generation sources. Physical heat removal tubes are not modeled. In the simulations, constant heat removal rate is applied irrespective of the location of the tubes. The effect of removing equal amounts of heat from the cavity from different depths on the thermal field of the cavity is examined. It is found that (actually the finding is in accordance with experimental data) the heat removal process affects the regions below the tubes more than the regions above the tubes. The effect of heat removal is seen all the way down to the bottom of the cavity whereas only a couple of centimeters above the heat removal tubes feel any disturbance. As a result, when heat is removed from a lower layer, the stored energy content of the cavity at the end of the heat removal is higher.

The present 2D code can be used as a basis for a 3D code simulating the heat removal tubes (or heat exchangers) more realistically. Simulation of an incompressible flow in 3D with combined natural and forced convection needs a lot of computer power. Instead of using CPU computation, the newly emerging GPU computing could be tried to shorten computation times.

The effect of wind on the free surface (which is actually a minor improvement) can be added. The Boussinesq approximation could be disregarded; the y -momentum equation can be solved as is since the temperature dependence of the water density can be implemented to the code quite easily.

A couple of commercial codes were tried for benchmark purposes without any success. ANSYS FLUENT does not have the exact same slip (no-shear) boundary condition (see equation (3.13)), ANSYS CFX finds the thermal field but the velocity field does not reach a steady pattern rather than a chaotically fluctuating one continuously. COMSOL Multiphysics cannot even maintain a solution. So for a commercial code user moderate as the author himself, it may be concluded that learning and perfecting a commercial code, using it to solve a complicated flow problem, failing to achieve a solution, changing the commercial code and starting from the beginning could be more time consuming than writing one's own CFD/CHT code.

To double-check the comparison of simulations with experimental data, three more simulations are run with the data of Experiment 1 from [17]. The parameters of the experiment are $A = H/L = 0.26$, $\dot{m}_m = 206 \text{ kg/hr}$, $T_m = 47.5^\circ\text{C}$, $T_{ic} = 25.2^\circ\text{C}$, $T_{amb} = 24^\circ\text{C}$, and an average maximum $q''_{wl} = 3700 \text{ W/m}^2$. The vertical temperature development curves for the three different vertical side wall thermal B.C.'s of Fig. 7.9.b, c, and d are presented in Fig. B.7, 8, and 9 respectively. The sole difference of the simulations from the experiment is that in the simulations, the mean side wall heat flux value is somewhat higher, $q''_{wl} = 5000 \text{ W/m}^2$. The temperature data points of the experiment are also presented in the figures. Comparison of the figures yields the same conclusion as of Section 7.2, vertical side wall thermal B.C. depicted in Fig. 7.9.d is the better choice among these three different side wall thermal B.C.'s.

REFERENCES

- [1] Kakaç S., Paykoç E., and Yener Y., Storage of Solar Thermal Energy, *Energy Storage Systems: Fundamentals & Applications*, ASI Proceedings, 1988.
- [2] Oberkampf W. L. and Crow L. I., Numerical study of the velocity and temperature fields in a flow-through reservoir, *J. Heat Transfer*, Vol. 98, pp. 353-359, 1976.
- [3] Lavan Z. and Thompson J., Experimental study of thermally stratified hot water storage tanks, *Solar Energy*, Vol. 19, pp. 519-524, 1977.
- [4] Çömez F., Large Scale Energy Storage, M. S. Thesis, ME Department of Middle East Technical University, 1981.
- [5] Jaluria Y. and Gupta S. K., Decay of thermal stratification in a water body for solar energy storage, *Solar Energy*, Vol. 28, No. 2, pp. 137-143, 1982.
- [6] Jaluria Y. and O'Mara B. T., Thermal field in a water body for solar energy storage and extraction due to a buoyant two-dimensional surface water jet, *Solar Energy*, Vol. 43, No. 3, pp. 129-138, 1989.
- [7] Yoo H. and Pak E.-T., Theoretical model of the charging process for stratified thermal storage tanks, *Solar Energy*, Vol. 51, No. 6, pp. 513-519, 1993.
- [8] Safi M. J. and Loc T. P., Development of thermal stratification in a two-dimensional cavity: a numerical study, *Int. J. Heat Mass Transfer*, Vol. 37, No. 14, pp. 2017-2024, 1994.
- [9] Eames P. C. and Norton B., The effect of tank geometry on thermally stratified sensible heat storage subject to low Reynolds number flows, *Int. J. Heat Mass Transfer*, Vol. 41, No. 14, pp. 2131-2142, 1998.
- [10] Hahne E. and Chen Y., Numerical study of flow and heat transfer characteristics in hot water stores, *Solar Energy*, Vol. 64, Nos 1-3, pp. 9-18, 1998.
- [11] Bouhdjar A. and Harhad A., Numerical analysis of transient mixed convection flow in storage tank: influence of fluid properties and aspect ratios on stratification, *Renewable Energy*, Vol. 25, pp. 555-567, 2002.

- [12] Ersoy Y., Numerical Solution of Laminar Mixed Convection in Cavities, M. S. Thesis, ME Department of Middle East Technical University, 1982.
- [13] Saha S., Saha G., Ali M., Islam Q., Combined Free and Forced Convection Inside a Two-Dimensional Multiple Ventilated Rectangular Enclosure, *ARPN Journal of Engineering and Applied Sciences*, Vol. 1, No. 3, pp. 23-35, 2006.
- [14] Das S.P., Chakraborty S., and Dutta P., Numerical Convection in a Two-Dimensional Enclosure Heated Symmetrically from Both Sides, *Int. Comm. Heat Mass Transfer*, Vol. 29, No. 3, pp. 345-354, 2002
- [15] Rahman M. M., Alim M. A., and Mamun M. A. H., Proceedings of the International Conference on Mechanical Engineering 2007 (ICME2007) 29- 31 December 2007, Dhaka, Bangladesh
- [16] Papanicolaou E. and Belessiotis V., Transient development of flow and temperature fields in an underground thermal storage tank under various charging modes, *Solar Energy*, Volume 83, Issue 8, August 2009, Pages 1161–1176.
- [17] Kayserilioğlu Y. S., Heat Removal from a Large Scale Warm Water Storage, M. S. Thesis, ME Department of Middle East Technical University, 2004.
- [18] Jaluria Y., Thermal Energy Storage and Extraction in Solar Ponds, B. Kılıkış and S. Kakaç (Eds.), in *Energy Storage Systems*, Kluwer Academic Publishers, 1989.
- [19] Yang K.T., Natural Convection in Enclosures, in *Handbook of Single-Phase Convective Heat Transfer*, S. Kakaç, R.K. Shah and W. Aung (Eds.), Chapter 13, John Wiley, 1987.
- [20] Incropera F. P. and DeWitt D. P., *Fundamentals of Heat and Mass Transfer*, Chap. 9, John Wiley & Sons, 1996.
- [21] Versteeg H.K., Malalasekera W., *An Introduction to Computational Fluid Dynamics, The Finite Volume Method*, Pearson Education Limited, 1995.
- [22] Spalding D.B. A Novel Finite Difference Formulation for Differential Expressions Involving Both First and Second Derivatives, *Int. J. Num. Methods.*, Vol. 4, p 551, 1972.
- [23] Patankar S.V., *Numerical Heat Transfer and Fluid Flow*, Hemisphere Publishing Corporation, Taylor & Francis Group, New York, 1980.
- [24] Leonard B.P., A Stable and Accurate Convective Modelling Procedure Based on Quadratic Upstream Interpolation , *Comput. Methods Appl. Mech. Eng.*, Vol. 19, pp. 59-98, 1979.

- [25] Patankar S.V., Spalding D.B., A Calculation Procedure for Heat, Mass and Momentum Transfer in Three-Dimensional Parabolic Flows, *Int. J. Heat Mass Transfer*, Vol. 15, p. 1787, 1972.
- [26] Thomas L.H., Elliptic Problems in Linear Difference Equations over a Network, Watson Sci. Comput. Lab. Report, Columbia University, New York, 1949.
- [27] ANSYS FLUENT 12.0 User's Guide, Release 12.0 © ANSYS, Inc. 2009-01-29.
- [28] Bloodshed Software (August 2013) <http://www.bloodshed.net/index.html>
- [29] Nakiboğlu G., Development Of An Educational CFD Software For Two Dimensional Incompressible Flows, M. S. Thesis, ME Department of Middle East Technical University, 2007.
- [30] Saha S., Mamun Md.A.H, Hossain Z., Islam A.K.M. A., Mixed Convection in an Enclosure with Different Inlet and Exit Configurations, *J. Applied Fluid Mechanics*, Vol. 1, No. 1, pp. 78-93, 2008.

APPENDIX A

DISCRETIZATION OF THE GENERAL TRANSPORT EQUATION WITH HYBRID DIFFERENCING SCHEME

The hybrid differencing scheme is a combination of second order accurate central differencing, which lacks the appropriate flow direction information (transportiveness) and the first order accurate upwind differencing scheme, which has the transportiveness property. The local Peclet number is the parameter that discriminates when to use the aforementioned two interpolation schemes. The Peclet number for the west face of a 3D C.V. (see Fig. 4.1) is

$$Pe_w = \frac{(\rho u A)_w}{(\Gamma_w A)_w} = \frac{F_w}{D_w} \quad (A.1)$$

$$\Delta x_{WP}$$

When the local Peclet number is large, the flow is convection dominated and the upwind differencing scheme is used. When the local Peclet number is low, the flow is diffusion dominated and the central differencing is used.

$$\phi_w = \begin{cases} \phi_P & \text{if } Pe_w < -2 \\ \phi_W & \text{if } Pe_w > 2 \\ \frac{\phi_W + \phi_P}{2} & \text{if } -2 < Pe_w < 2 \end{cases} \quad (A.2)$$

The net flux through the west face is the summation of the convective and diffusive fluxes

$$q_w'' = (\rho u A \phi)_w - (\Gamma A)_w \frac{(\phi_P - \phi_W)}{\Delta x_{WP}} = F_w \phi_w - D_w (\phi_P - \phi_W) \quad (A.3)$$

If $Pe_w < -2$, equation (A.3) becomes:

$$q_w'' = F_w \phi_P - D_w (\phi_P - \phi_W) = F_w \left[\left(1 + \frac{1}{Pe_w} \right) \phi_P + \frac{1}{Pe_w} \phi_W \right] = F_w \phi_P + 0 \cdot \phi_W \quad (\text{A.4})$$

Assuming $\frac{1}{Pe_w} \rightarrow 0$. Hence

$$a_w = 0 \quad (\text{A.5})$$

If $Pe_w > 2$, equation (A.3) becomes:

$$q_w'' = F_w \phi_W - D_w (\phi_P - \phi_W) = F_w \left[\left(1 + \frac{1}{Pe_w} \right) \phi_W - \frac{1}{Pe_w} \phi_P \right] = F_w \phi_W + 0 \cdot \phi_P \quad (\text{A.6})$$

Assuming $\frac{1}{Pe_w} \rightarrow 0$. Hence

$$a_w = F_w \quad (\text{A.7})$$

If $-2 < Pe_w < 2$, equation (A.3) becomes:

$$q_w'' = \frac{F_w}{2} (\phi_W + \phi_P) - D_w (\phi_P - \phi_W) = \left(\frac{F_w}{2} + D_w \right) \phi_W + \left(\frac{F_w}{2} - D_w \right) \phi_P \quad (\text{A.8})$$

Hence

$$a_w = \frac{F_w}{2} + D_w \quad (\text{A.9})$$

Similar treatments to the other five control surfaces will yield the coefficients in equation (4.35).

APPENDIX B

ILLUSTRATIVE MATERIAL

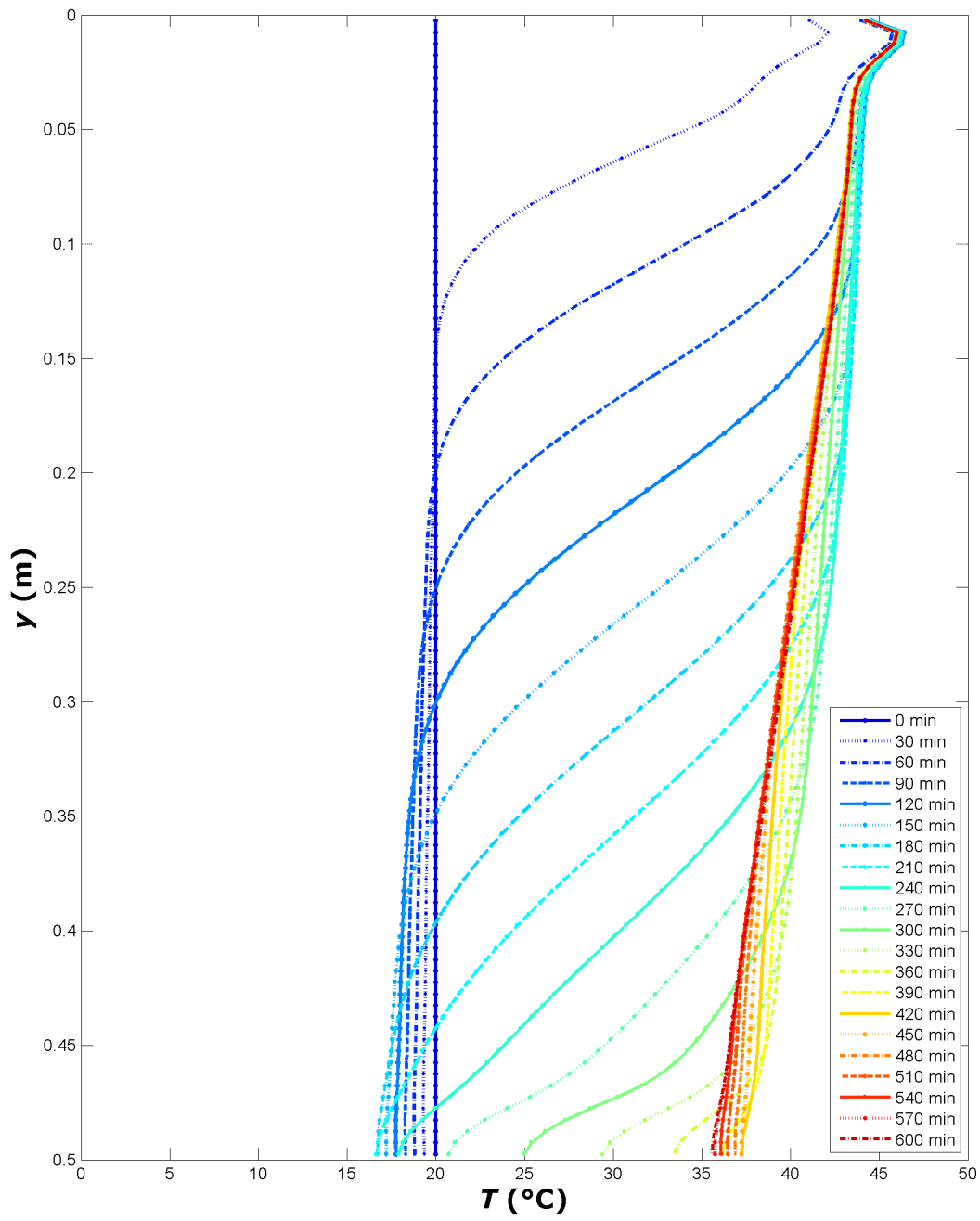


Fig. B.1 Development of Vertical Temperature Profile within Cavity at $x = 1$ m for Simulation 3

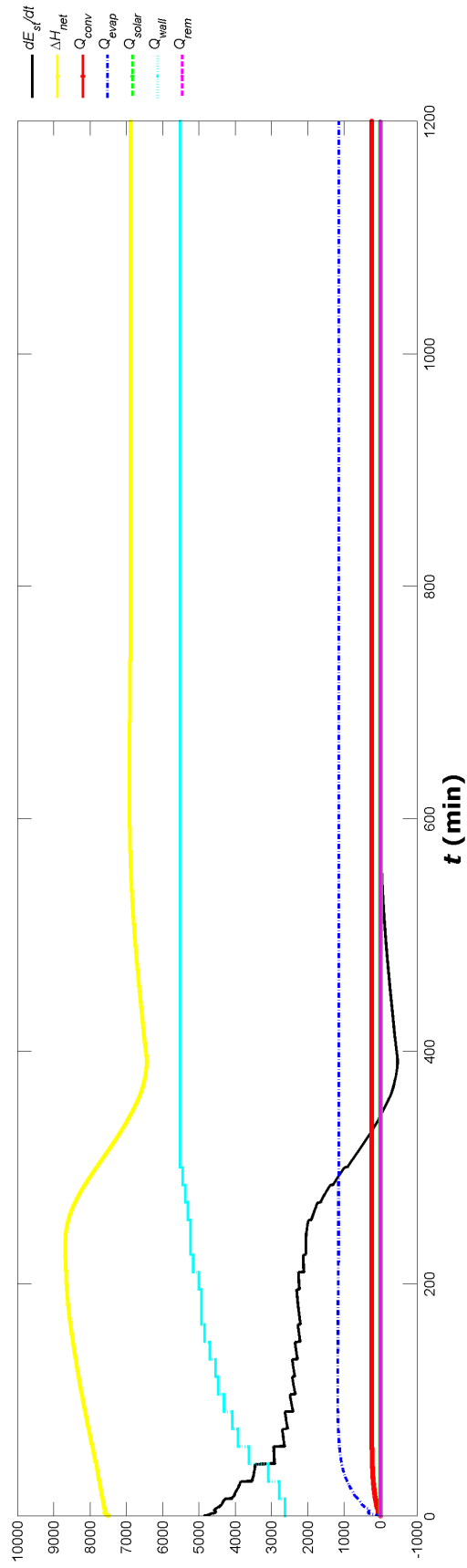


Fig. B.2 Variation of Components of Energy Equation in Time-Rate Form up to 1200 minutes for Simulation 14

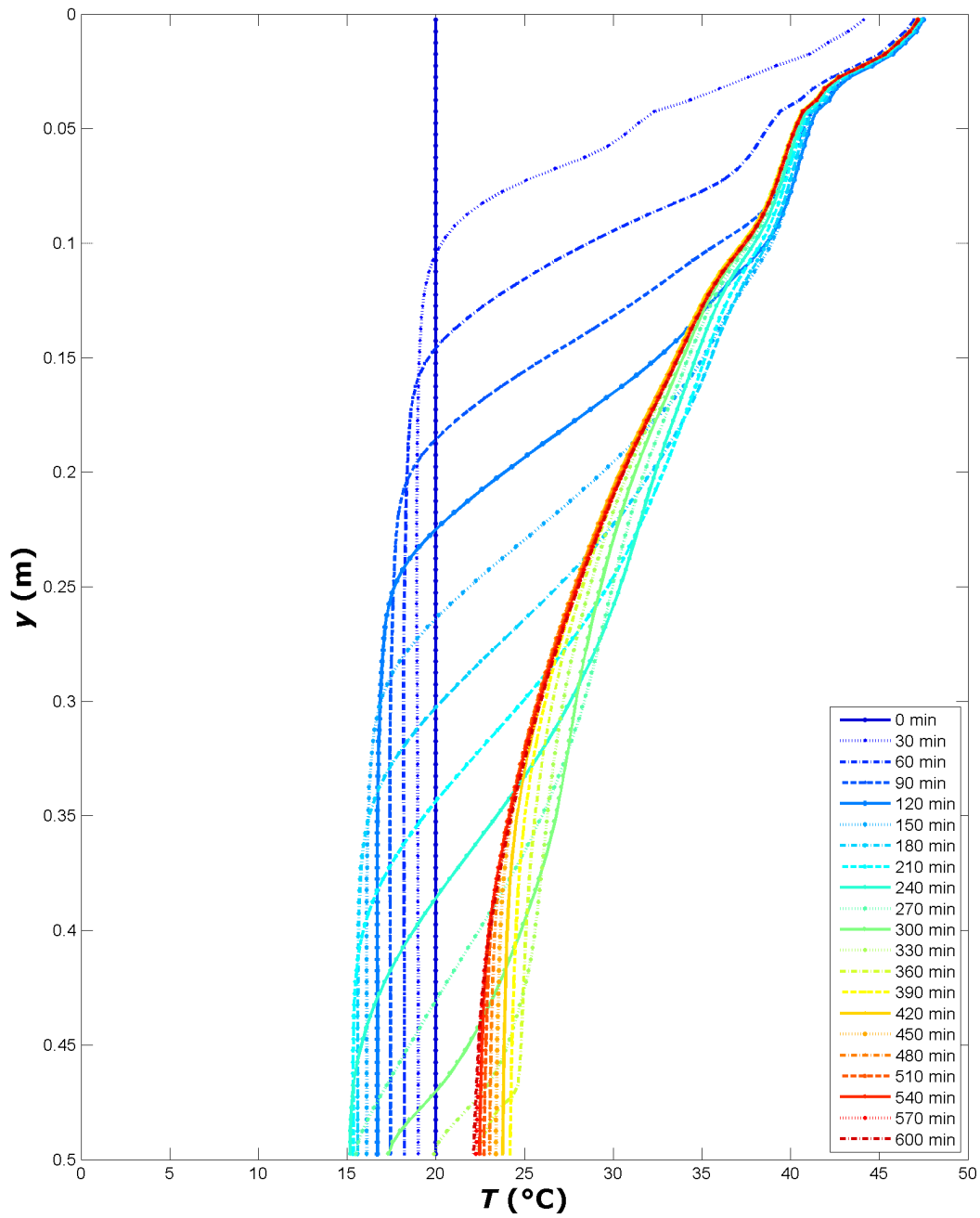


Fig. B.3 Development of Vertical Temperature Profile within Cavity at $x = 0\text{m}$ for Simulation 14

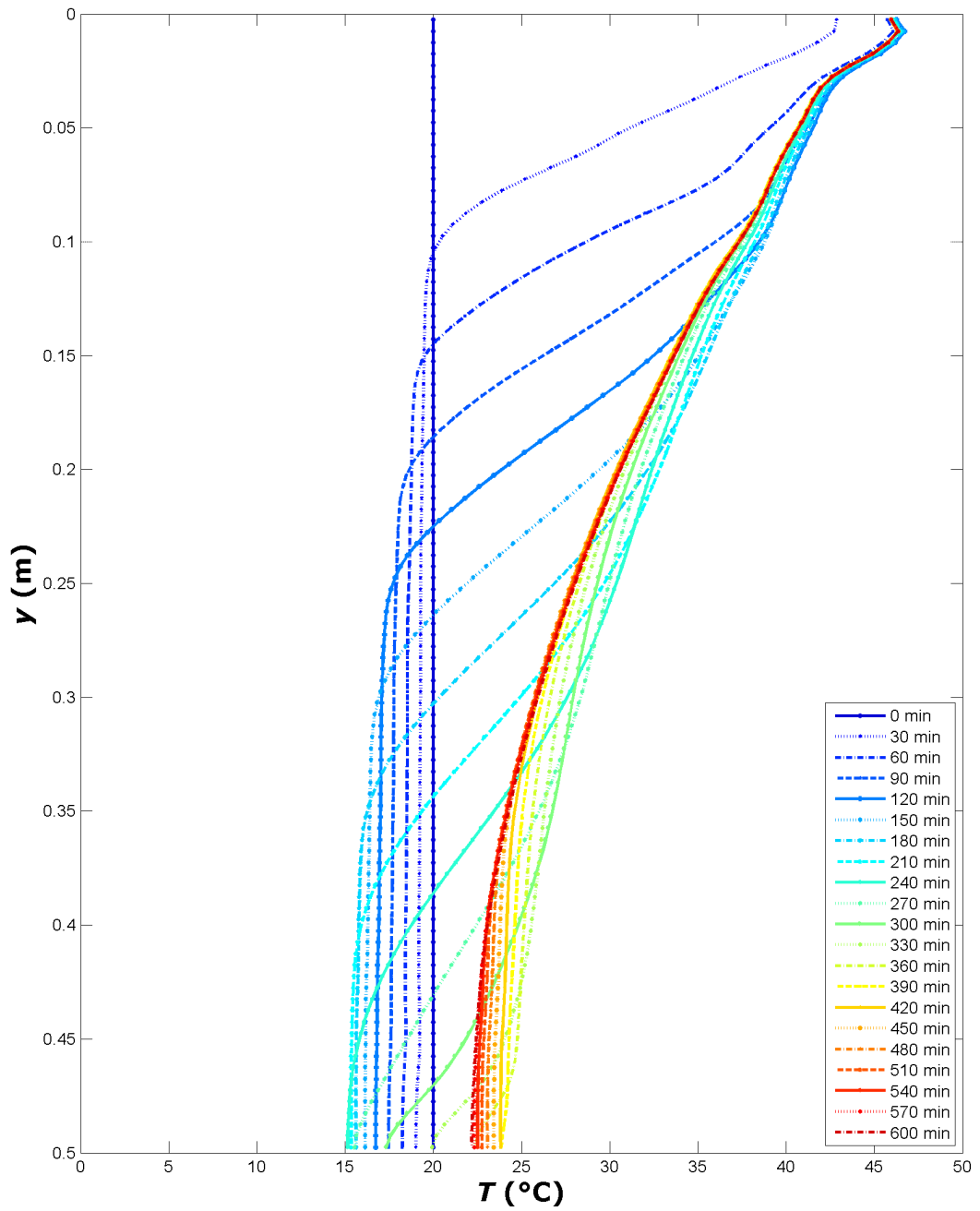


Fig. B.4 Development of Vertical Temperature Profile within Cavity at $x = 0.25$ m for Simulation 14

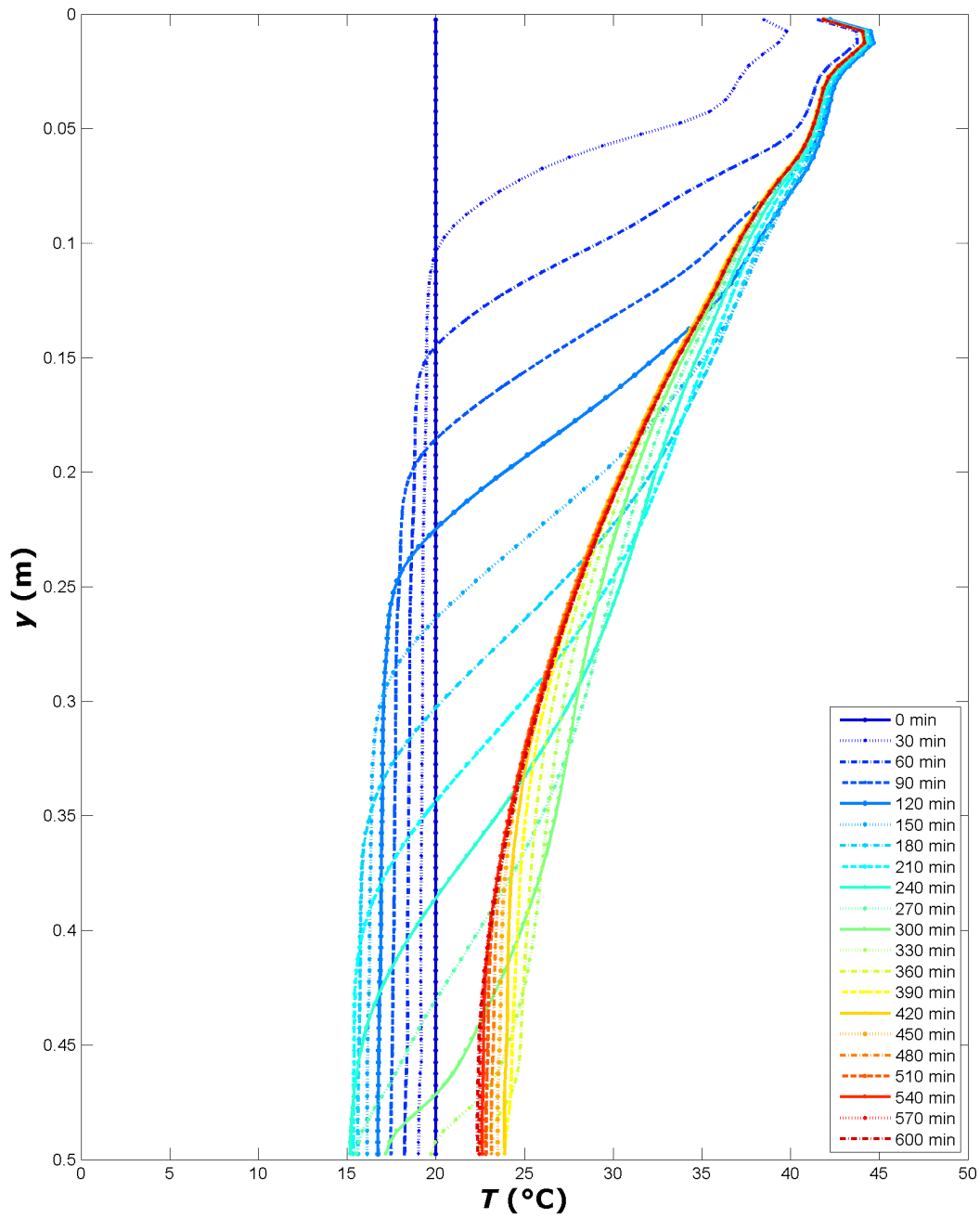


Fig. B.5 Development of Vertical Temperature Profile within Cavity at $x = 1.75\text{m}$ for Simulation 14

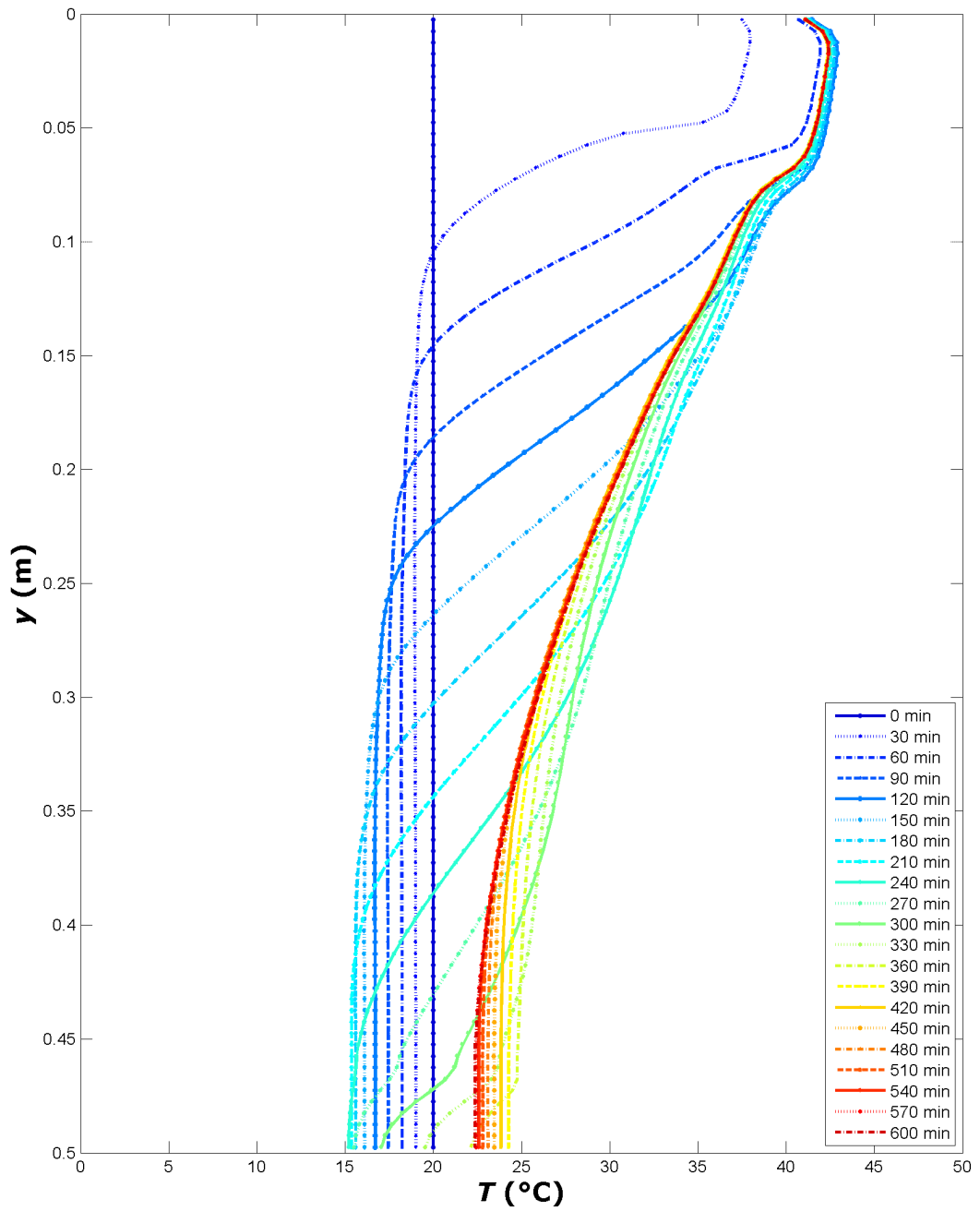


Fig. B.6 Development of Vertical Temperature Profile within Cavity at $x = 2$ m for Simulation 14

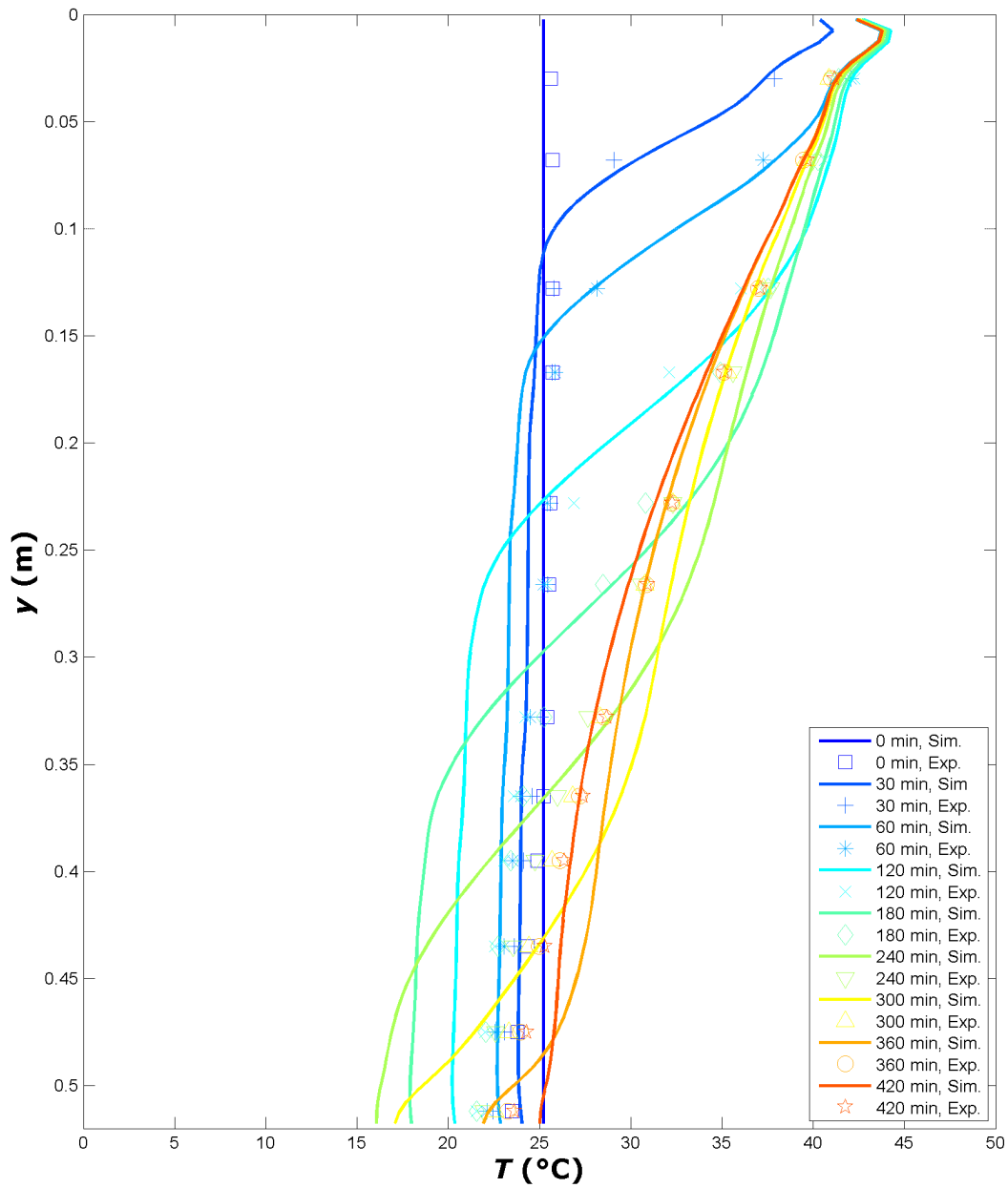


Fig. B.7 Comparison of Experimental Data (Experiment 1 from [17]) with Simulation Data, $A = H/L = 0.26$, $\dot{m}_{in} = 206 \text{ kg/hr}$, $T_{in} = 47.5^{\circ}\text{C}$, $T_{ic} = 25.2^{\circ}\text{C}$, $T_{amb} = 24^{\circ}\text{C}$, $q''_{wl} = 5000 \text{ W/m}^2$ as of Fig. 7.9.b

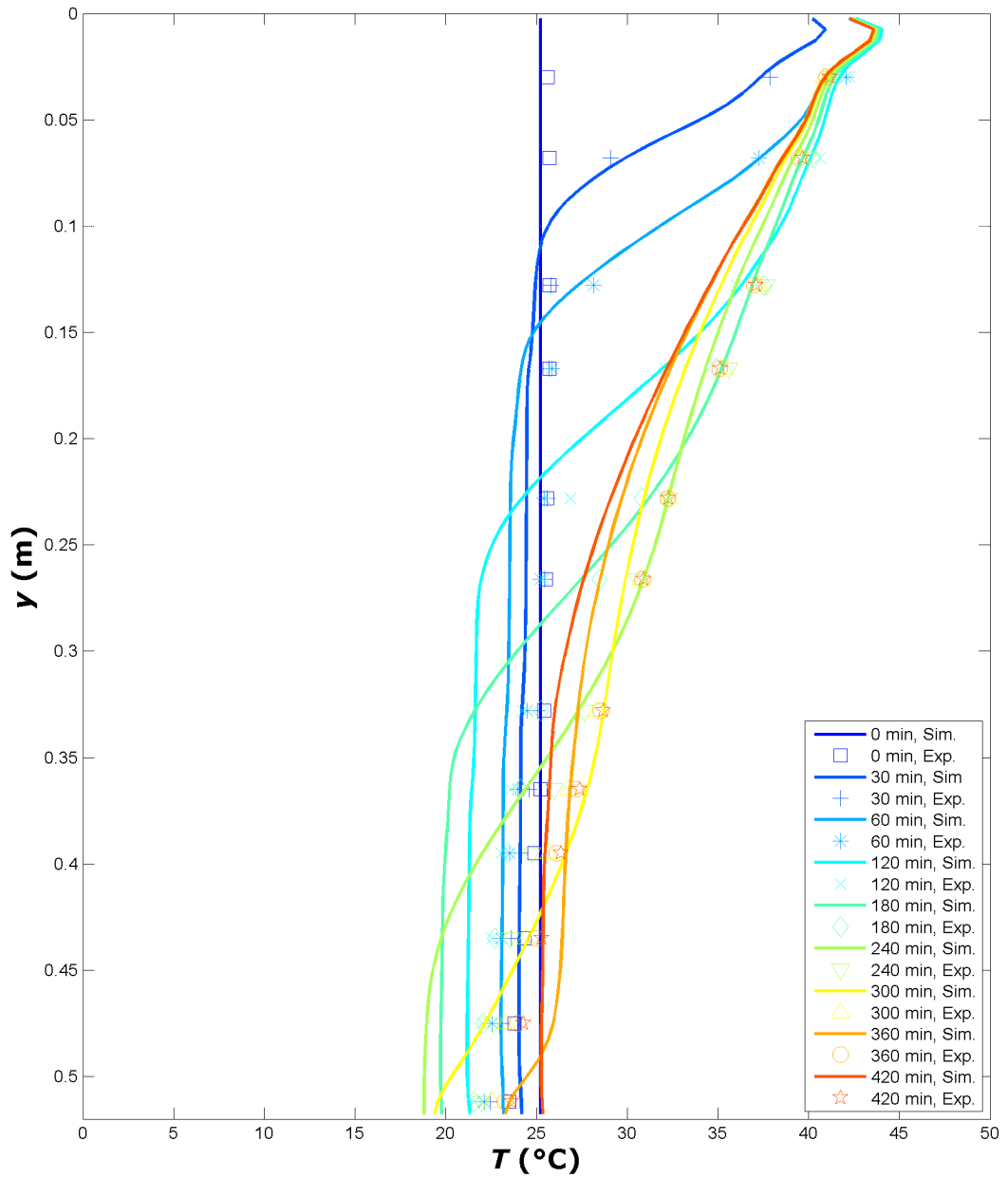


Fig. B.8 Comparison of Experimental Data (Experiment 1 from [17]) with Simulation Data, $A = H/L = 0.26$, $\dot{m}_{in} = 206 \text{ kg/hr}$, $T_{in} = 47.5^\circ\text{C}$, $T_{ic} = 25.2^\circ\text{C}$, $T_{amb} = 24^\circ\text{C}$, $q''_{wl} = 5000 \text{ W/m}^2$ as of Fig. 7.9.c

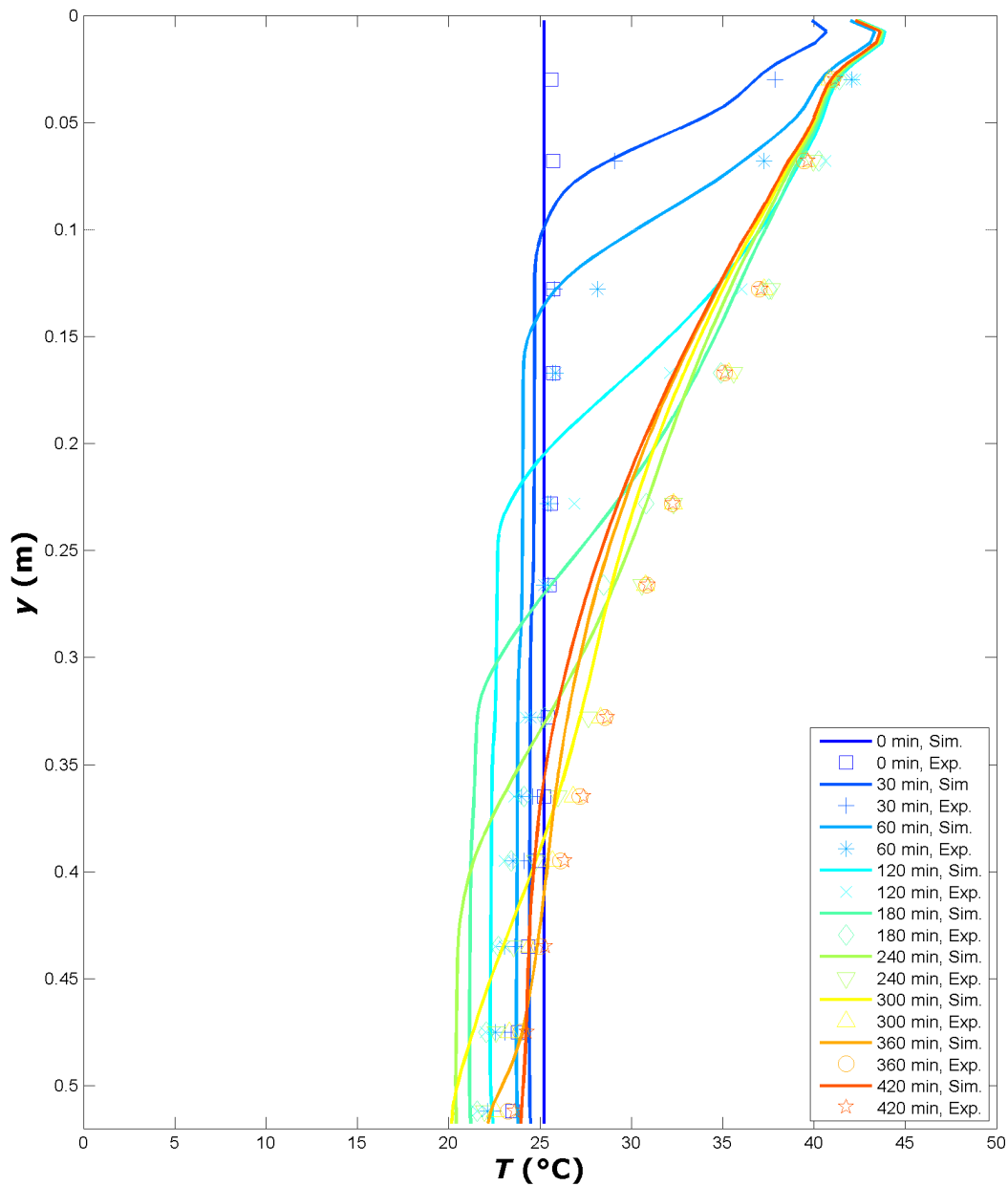


Fig. B.9 Comparison of Experimental Data (Experiment 1 from [17]) with Simulation Data, $A = H/L = 0.26$, $\dot{m}_{in} = 206 \text{ kg/hr}$, $T_{in} = 47.5^{\circ}\text{C}$, $T_{ic} = 25.2^{\circ}\text{C}$, $T_{amb} = 24^{\circ}\text{C}$, $q''_{wl} = 5000 \text{ W/m}^2$ as of Fig. 7.9.d

Table B.1 Geometry and Flow Parameters of the Simulations

Sim. #	H (m)	L (m)	$A = \frac{H}{L}$	T_{in} ($^{\circ}\text{C}$)	u_{in} (m/s)	T_{ic} ($^{\circ}\text{C}$)	T_{amb} ($^{\circ}\text{C}$)	q''_{solar} (W/m^2)	Wall B.C.
1	0.5	2.0	0.25	50	0.0015	20	20	0	$T_{wl} = 10^{\circ}\text{C}$
2	0.5	2.0	0.25	50	0.0015	20	20	0	$T_{wl} = 0^{\circ}\text{C}$
3	0.5	2.0	0.25	50	0.0015	20	20	0	$T_{wl} = 10 - 0^{\circ}\text{C}$
4	0.5	2.0	0.25	50	0.0015	20	20	0	$q_{wl} = 4000 \text{ W}/\text{m}^2$
5	0.5	2.0	0.25	50	0.0015	20	20	0	$q_{wl} = 7000 \text{ W}/\text{m}^2$
6	0.5	2.0	0.25	50	0.0015	20	20	0	$q_{wl} = 6000 \text{ W}/\text{m}^2$
7	0.5	2.0	0.25	50	0.0015	20	20	0	$q_{wl} = 5000 \text{ W}/\text{m}^2$
8	0.5	2.0	0.25	50	0.0015	20	20	0	$q_{wl} = 4000 \text{ W}/\text{m}^2$ *
9	0.5	2.0	0.25	50	0.0015	20	20	0	$q_{wl} = 7000 \text{ W}/\text{m}^2$ *
10	0.5	2.0	0.25	50	0.0015	20	20	0	$q_{wl} = 6000 \text{ W}/\text{m}^2$ *
11	0.5	2.0	0.25	50	0.0015	20	20	0	$q_{wl} = 5000 \text{ W}/\text{m}^2$ *
12	0.5	2.0	0.25	50	0.0015	20	20	0	$q_{wl} = 6000 \text{ W}/\text{m}^2$ **
13	0.5	2.0	0.25	50	0.0015	20	20	0	$q_{wl} = 6000 \text{ W}/\text{m}^2$ ***
14	0.5	2.0	0.25	50	0.0015	20	20	0	$q_{wl} = 6000 \text{ W}/\text{m}^2$ ****
15	0.5	2.0	0.25	50	0.0015	16	16	0	$q_{wl} = 6000 \text{ W}/\text{m}^2$ ****
16	0.5	2.0	0.25	50	0.0015	20	16	0	$q_{wl} = 6000 \text{ W}/\text{m}^2$ ****
17	0.5	2.0	0.25	50	0.0015	24	16	0	$q_{wl} = 6000 \text{ W}/\text{m}^2$ ****
18	0.5	2.0	0.25	50	0.0015	24	24	0	$q_{wl} = 6000 \text{ W}/\text{m}^2$ ****
19	0.5	2.0	0.25	50	0.0015	20	10	0	$q_{wl} = 6000 \text{ W}/\text{m}^2$ ****
20	0.5	2.0	0.25	40	0.0015	20	20	0	$q_{wl} = 6000 \text{ W}/\text{m}^2$ ****
21	0.5	2.0	0.25	50	0.0015	20	20	200	$q_{wl} = 6000 \text{ W}/\text{m}^2$ ****
22	0.5	2.0	0.25	50	0.0015	20	20	400	$q_{wl} = 6000 \text{ W}/\text{m}^2$ ****
23	0.3	2.0	0.15	50	0.0015	18	18	0	$q_{wl} = 5500 \text{ W}/\text{m}^2$ ****
24	0.3	2.0	0.15	50	0.0015	18	18	0	$q_{wl} = 5000 \text{ W}/\text{m}^2$ ****
25	0.3	2.0	0.15	50	0.0015	18	18	0	$q_{wl} = 4500 \text{ W}/\text{m}^2$ ****
26	0.3	2.0	0.15	50	0.0015	18	18	0	$q_{wl} = 4000 \text{ W}/\text{m}^2$ ****
27	0.3	2.0	0.15	50	0.0015	18	18	0	$q_{wl} = 3000 \text{ W}/\text{m}^2$ ****
28	0.3	2.0	0.15	50	0.0015	24	24	0	$q_{wl} = 5500 \text{ W}/\text{m}^2$ ****
29	0.3	2.0	0.15	50	0.0015	24	24	0	$q_{wl} = 5000 \text{ W}/\text{m}^2$ ****
30	0.3	2.0	0.15	50	0.0015	24	24	0	$q_{wl} = 4500 \text{ W}/\text{m}^2$ ****
31	0.3	2.0	0.15	50	0.0015	24	24	0	$q_{wl} = 4000 \text{ W}/\text{m}^2$ ****
32	0.3	2.0	0.15	50	0.0015	24	24	0	$q_{wl} = 3000 \text{ W}/\text{m}^2$ ****
33	0.3	2.0	0.15	50	0.0015	20	20	0	$q_{wl} = 5500 \text{ W}/\text{m}^2$ ****

* As in Fig. 7.9.a

** As in Fig. 7.9.b

*** As in Fig. 7.9.c

**** As in Fig. 7.9.d

Table B.2 Wall Heat Flux Variation with Time in a Typical Experiment

$q_{wl}(t)$ (W/m ²)	Time Interval
2000	$0 \leq t \leq 15$ min
2100	$15 \leq t \leq 30$ min
2300	$30 \leq t \leq 45$ min
2650	$45 \leq t \leq 60$ min
2850	$60 \leq t \leq 75$ min
2950	$75 \leq t \leq 90$ min
3100	$90 \leq t \leq 105$ min
3200	$105 \leq t \leq 120$ min
3250	$120 \leq t \leq 135$ min
3350	$135 \leq t \leq 150$ min
3450	$150 \leq t \leq 165$ min
3500	$165 \leq t \leq 180$ min
3500	$180 \leq t \leq 195$ min
3550	$195 \leq t \leq 210$ min
3650	$210 \leq t \leq 225$ min
3700	$225 \leq t \leq 240$ min
3700	$240 \leq t \leq 255$ min
3750	$255 \leq t \leq 270$ min
3800	$270 \leq t \leq 285$ min
3850	$285 \leq t \leq 300$ min
3900	$t \geq 300$ min

CURRICULUM VITAE

PERSONAL INFORMATION

Surname, Name : Kayseriliöđlu, Yavuz Selim
Date & Place of Birth : 6th of January, 1979 in Ankara/Turkey
Nationality : Turkish
Phone : 0090 312 592 34 84 / 0090 312 468 49 87
E-mail Address : ykayserili@aselsan.com.tr
yavuz.kayserilioglu@gmail.com
Work Address : ASELSAN A.Ş. Mehmet Akif Ersoy Mahallesi
296. Cadde No: 16, 06370 Yenimahalle / Ankara,
Turkey
Permanent Address : Güvenlik Cad. 103/11 Aşađıayrancı / Ankara,
Turkey

EDUCATION

Degree	Institution	Graduation Year
M.S.	METU Mech. Eng. Dept.	2004
B.S.	METU Mech. Eng. Dept.	2001
High School	Ankara Atatürk Anatolian High School	1997

WORK EXPERIENCE

Year	Organization	Enrollment
2005 - Present	ASELSAN A.Ş.	Mechanical Design Engineer
2001 - 2004	METU Mech. Eng. Dept	Teaching Assistant
August of 2000	ASELSAN A.Ş.	Intern Engineering Student
August of 1999	Türk Traktör Fabrikaları A.Ş.	Intern Engineering Student

FOREIGN LANGUAGES

English (Advanced), Italian (Intermediate)